Exploration of the Cosmic Dawn with High-Redshift Quasars

Masafusa Onoue

Doctor of Philosophy

Department of Astronomical Science

School of Physical Sciences

SOKENDAI (Graduate University for Advanced Study),

National Astronomical Observatory of Japan

January 10, 2018

Ph.D. Thesis Committee (alphabet order):

Dr. Mareki Honma (SOKENDAI, National Astronomical Observatory of Japan)

Dr. Ikuru Iwata (SOKENDAI, National Astronomical Observatory of Japan)

Dr. Kazuhiro Shimasaku (University of Tokyo)

Dr. Tadafumi Takata (SOKENDAI, National Astronomical Observatory of Japan)

Dr. Keiichi Wada (Kagoshima University)

Thesis Advisors:

Dr. Nobunari Kashikawa (SOKENDAI, National Astronomical Observatory of Japan)

Dr. Satoshi Miyazaki (SOKENDAI, National Astronomical Observatory of Japan)

Dr. Masayuki Tanaka (SOKENDAI, National Astronomical Observatory of Japan)

Acknowledgment

I would like to thank the following persons for their great help during my five years as a PhD student in SOKENDAI and National Astronomical Observatory of Japan. First of all, I would like to express my gratitude to my thesis advisor, Associate Prof. Nobunari Kashikawa. He assigned the high-redshift quasar search project with the HSC-SSP to me when I entered SOKENDAI. During my school and undergraduate years, I used to see articles on the newspapers about the discoveries of the highest-redshift galaxies at that time with the Subaru telescope, which made me want to learn the observational astronomy and explore the highest-redshift universe. Therefore, I could spent these five years in doing what I have long dreamed of. He guided me with great care throughout my PhD years. I could learn a lot from him: the basics of the observational astronomy, the way to plan observations, the way to tackle the mysteries of the universe, and the way to lead big projects. He always reviewed my papers and observation proposals whenever I needed, which greatly improved the clarity and logics. Other than those, one of the best things I learn may be the importance of enjoying the science. I thank Prof. Satoshi Miyazaki, who is one of the supervisors and the leader of the HSC-SSP survey. It was my pleasure that I could spent my PhD years with the ground breaking survey project. I was lucky that I could have an opportunity once to measure the transmission of the HSC-i filter. I am indebted to Prof. Masayuki Tanaka for for his invaluable support. He kindly took his time to teach me the basics of observation and data reduction. He also helped me a lot in developing a photometric redshift selection for $z > 6$ quasars

Other than the supervisors, I was supported by a lot of astronomers. My thanks go to Yoshiki Matsuoka, who has been leading the $z > 6$ quasar search with the HSC-SSP. My thanks go to Tohru Nagao. Without him as a chair of the HSC-AGN group, the HSC-AGN working group could not have been active. I am deeply grateful to the entire HSC collaboration for realizing the unprecedented wide-field survey with a 8m telescope and for giving me feedbacks on my papers and observation proposals. I would like to thank Dr. Bram Venemans, Prof. Fabian Walter and their research group at MPIA in Heidelberg, Germany. I was fortune that I could go to MPIA as an internship program of the SOKENDAI for three months from November 2015 to January 2016. The study of quasar pair environments with the HSC-SSP could not have been realized without their supports at the initiation. I am especially indebted to Bram Venemans, who kindly accepted to host me in MPIA when I met him in a conference in Groningen, Netherland. The experience in one of the world's top institute was one of the most exciting experience in my PhD years. My thanks go to the high-redshift quasar group members in MPIA especially Chiara Mazzucchelli and Dr. Emanuele Farina, who were always kind to me.

I would like to thank the group members in NAOJ, Jun Toshikawa, Shogo Ishikawa, Hisakazu Uchiyama, Kei Ito, Shigeru Namiki, and Youngming Liang, for their kind suggestions and discussions on each other's work in the group meeting. My thanks go to other staffs and students in the Subaru building of NAOJ, who spent time together in these five years. I am grateful to the same-year students in the Mitaka Campus, especially Tsuguru Ryu, Haruka Baba, Koki Okutomi, Kotomi Taniguchi, Yuta Kato, Yutaka Hirai, Akio Taniguchi, Kazuma Mitsuda, who spent good and hard times together during our PhD years. The D3 workshop we held in the Nobeyama Observatory in 2017 summer was a great workshop.

Last but not least, I would like to thank my family, Yoshifusa Onoue and Seiko Onoue, who taught me how beautiful the night sky is. I deeply appreciate their steady and warm support.

This work is based on data collected at the Subaru Telescope and retrieved from the HSC data archive system, which is operated by Subaru Telescope and Astronomy Data Center at National Astronomical Observatory of Japan. The Hyper Suprime-Cam (HSC) collaboration includes the astronomical communities of Japan and Taiwan, and Princeton University. The HSC instru-

mentation and software were developed by the National Astronomical Observatory of Japan (NAOJ), the Kavli Institute for the Physics and Mathematics of the Universe (Kavli IPMU), the University of Tokyo, the High Energy Accelerator Research Organization (KEK), the Academia Sinica Institute for Astronomy and Astrophysics in Taiwan (ASIAA), and Princeton University. Funding was contributed by the FIRST program from Japanese Cabinet Office, the Ministry of Education, Culture, Sports, Science and Technology (MEXT), the Japan Society for the Promotion of Science (JSPS), Japan Science and Technology Agency (JST), the Toray Science Foundation, NAOJ, Kavli IPMU, KEK, ASIAA, and Princeton University. This paper makes use of software developed for the Large Synoptic Survey Telescope. We thank the LSST Project for making their code available as free software at `http://dm.lsst.org`. The Pan-STARRS1 Surveys (PS1) have been made possible through contributions of the Institute for Astronomy, the University of Hawaii, the Pan-STARRS Project Office, the Max-Planck Society and its participating institutes, the Max Planck Institute for Astronomy, Heidelberg and the Max Planck Institute for Extraterrestrial Physics, Garching, The Johns Hopkins University, Durham University, the University of Edinburgh, Queen's University Belfast, the Harvard-Smithsonian Center for Astrophysics, the Las Cumbres Observatory Global Telescope Network Incorporated, the National Central University of Taiwan, the Space Telescope Science Institute, the National Aeronautics and Space Administration under Grant No. NNX08AR22G issued through the Planetary Science Division of the NASA Science Mission Directorate, the National Science Foundation under Grant No. AST-1238877, the University of Maryland, and Eotvos Lorand University (ELTE) and the Los Alamos National Laboratory. A part of this work is financially supported by the overseas internship fund of Department of Astronomical Science, SOKENDAI and JSPS KAKENHI Grant Number 15J02115.

January 10, 2018
M.O.

Abstract

Quasars are one of the unique probes of the early universe. We can learn from the observations of high-redshift quasars, for example, the reionization history, the early growth of the super massive black holes (SMBHs), and the build-up of the SMBH co-evolutionary growth with host galaxies. However, the observations of quasars in the reionization epoch have been difficult due to their small number density compared to galaxies at the same redshift. Moreover, the number of $z > 6$ quasars has been increased to more than 200 thanks to recent tremendous observational efforts with wide-field surveys, but most of them are the extremely luminous quasars limited by the survey depths, which may bias the understanding of the SMBH growth history. This thesis explores the relatively unexplored, low-luminosity quasars at $z > 6$ to investigate the roles of high-redshift quasars from unique points of views exploiting wide and deep optical surveys of the 8.2m Subaru telescope, especially the Hyper Suprime-Cam Subaru Strategic Program covering 1400 deg^2.

First, we address the quasar contribution to cosmic reionization with our deep imaging survey of $z \sim 6$ low-luminosity quasars with Subaru/Suprime-Cam down to $z_R = 24.15$ mag in the UKIDSS-DXS fields covering 6.5 deg^2. From our photometric color selection, we select 17 candidates and identify two quasars from our follow-up spectroscopy and additional deeper photometry with the HSC-SSP, while one of the two could be a galaxy due to its narrow Lyα emission line as a type-I quasar. Thanks to the deep imaging, we put a unique constraint on the faint-end ($M_{1450} \sim -23$) of the $z = 6$ quasar luminosity function (QLF), which has been poorly constrained due to the survey depths of most of the previous quasar surveys. From the QLF, the quasar photon budget of ionizing photons is found to be only $1-12\%$ required for reionization at $z \sim 6$ with 2σ confidence. Even taking into account several systematic uncertainties such as the clumping factor of intergalactic medium and the minimum magnitude of the QLF, we for the first time derive the firm evidence that quasars are only the minor contributors of reionization, based on the complete identification of faint quasar candidates.

Next, the search for $z > 6$ low-luminosity quasars is extended with the much wider HSC-SSP. From the first-year data of the HSC-SSP, we have identified more than 70 quasars at $z \sim 6-7$ in > 400 deg^2, which has already exceeded the number of the SDSS $z \sim 6$ quasars. Since those samples are ~ 2 magnitude fainter than most of the other quasars discovered through shallow surveys such as the SDSS, we have succeeded in probing down the tip of the iceberg. In this thesis work, we took deep near-infrared spectroscopy for five new low-luminosity quasars from the HSC-SSP in Gemini/GNIRS and VLT/X-SHOOTER. From the obtained spectra, we detected broad emission lines of MgII and CIV with underlying continuum. We serendipitously found a highest-redshift red quasar at $z = 6.71$ characterized by its unusually red broad-band color of $y_{\rm HSC} - W2 \sim 3$, which is in the transitional phase from starburst to type-I quasar.

We measure their black hole mass with the so-called single-epoch method utilizing the emission line widths and the continuum luminosity obtained from the spectra. The estimated virial black hole mass is in the range of $2 \times 10^7 M_\odot \leq M_{\rm BH} \leq 9 \times 10^9 M_\odot$ with the Eddington ratio of $0.2 \leq L_{\rm bol}/L_{\rm Edd} \leq 3.6$. Such a variation in the Eddington ratio was not seen in the most luminous $z > 6$ quasars. The black hole masses of those with sub-Eddington accretion rates cannot be explained from seed BH models with the current growth rates due to the short timescale from their birth. We suggest that those two are already in the post-active phase of their initial mass growth even at such high redshift; they would be in the build-up phase of the galaxy-BH co-evolutionary growth known in the local universe, while it would not be the case for the exceptionally luminous quasars. The one red quasar has a super-Eddington ratio, which is consistent with the picture that SMBHs experience intense mass growth in the red quasar phase. Moreover, 37 quasars at $z > 6$ are compiled from the literatures and this study to obtain the Eddington ratio distribution of $z > 6$ quasars. Dividing into two luminosity bins at $L_{\rm bol} = 10^{47}$ erg s^{-1}, we find

that the average Eddington ratio is $< \log L_{\rm bol}/L_{\rm Edd} >= -0.10 \pm 0.20$ in the luminous bin, while quasars in the less luminous bin have $< \log L_{\rm bol}/L_{\rm Edd} >= -0.14 \pm 0.41$. While the high Eddington ratio is characteristic in $z > 6$ quasars, the large scatter in the less luminous bin shows that the low-luminosity range of $z > 6$ quasars are the mixture of the most active black holes and the quenched black holes. The absence of $M_{\rm BH} \sim 10^{10} M_{\odot}$ black holes with the sub-Eddington ratio implies a cut off in the black hole mass function at $z > 6$ perhaps limited by the timescale and accretion disk physics.

This work paves the way for various future studies. We will address the $z \sim 6-7$ QLF with the HSC-SSP, which enables us to further examine the redshift evolution of the QLF faint-end with its large samples size. The detailed study on the classification of the ambiguous populations found in the optical follow-up observation with narrow Lyα is crucial in the QLF estimate and has a possibility to identify new populations at $z > 6$ such as type-II quasars and galaxies with young stellar populations. The complete BH mass estimate for flux-limited HSC quasar samples yields to the understanding of the entire SMBH growth history up to $z \sim 7$, with the determination of several key statistical quantities such as black hole mass function and Eddington ratio distribution function at low-mass and low-accretion rate end.

Contents

Chapter 1

High-Redshift Quasars as a Probe of the Reionization Epoch

In this Chapter, a short introduction of this thesis is presented. Each section is meant to give an overview of the topic related to quasars in the cosmic dawn ($z > 3$). More focused introduction is given in the beginning of each chapter.

1.1 The First Billion Years of the Universe

Through the history of the universe, it is known that there has been several transitions of the baryonic medium. At the earliest stage ($z > 1100$), the universe is filled with hot and opaque plasma consisting of atomic nuclei and electrons. As the universe expands and cools down to thousands degrees, ionized medium recombines, which makes the universe transparent to lights ($t_{\rm universe} \sim 3.8 \times 10^5$ years). The photons interacting with the fluid of protons and electrons are now observable as the Cosmic Microwave Background. The period after the recombination is called as the dark ages, which is characterized by the lack of high energetic sources, dominated by the cooled neutral hydrogen gas. This neutral phase continues to $t_{\rm universe} \sim 0.5$ billion years at $z \sim 10-30$, and ends with the birth of first stars and galaxies with the ultraviolet (UV) radiation destroying the surrounding neutral hydrogen. This global transition of the universe is called as cosmic reionization, which leads to the universe full of galaxies as it is today.

1.2 Topics Related to High-Redshift Quasars

A quasar (quasi-stellar object, or QSO in short) is one of the most energetic extragalactic objects in the universe, which is powered by the mass accretion onto the central super massive black hole of a massive galaxy. 3C 273 is the first quasar discovered in Schmidt (1963). As described in Schmidt (2015) with his life history, this quasar is first identified as a compact radio source, which was found to be an extragalactic source at $z = 1.16$ based on the Balmer line detections. Thanks to the intrinsic brightness, quasars are one of the best probes of the distant universe, especially the reionization epoch. Moreover, we can learn on the formation and evolution of the super massive black holes, which are tightly connected to the growth of host galaxies (Kormendy & Ho, 2013). In the following sections, we describe how quasars can be used to probe the high-redshift universe.

1.2.1 Formation Sites of Quasars

The major triggering mechanism of quasars has been thought to be the major merger of gas-rich galaxies as proposed in, for example, Hopkins et al. (2008) and Alexander & Hickox (2012). Such heavy interaction of two galaxies would cause a large cold-gas inflow into the central parts of the merging galaxies due to the loss of angular momentum by shocks, which eventually induce dusty starbursts. This phase corresponds to the (Ultra) Luminous InfraRed Galaxies or ULIRGs in the local universe. The interacting galaxies are also observed in the rest-frame far-infrared as the sub-millimeter galaxies and dust obscured galaxies (Toba et al., 2015). The quasar phase comes after the starburst phase in which the strong quasar radiation destroys the surrounding dust. The galaxy star formation and black hole growth are quenched to be the dead elliptical galaxies after the cold gas is drained.

In this widely accepted scenario, it is expected that the formation sites of quasars should be massive haloes in which galaxy mergers occur frequently. Therefore, a number of studies uses quasars and radio-loud active galactic nuclei as probes of the massive environments (e.g., Steidel & Hamilton, 1992; Venemans et al., 2007). These studies suggest that radio galaxies are good probes of proto-clusters (Venemans et al., 2007; Hatch et al., 2014). However, it has been also shown that luminous quasars are not necessarily associated with massive haloes, which

has been recently revealed by the quasar environment studies of $z \sim 4-7$ quasars (Mazzucchelli et al., 2017; Kikuta et al., 2017, and references therein). Having said that, it should be noticed that these studies utilize deep imaging observations in the high-redshift quasar fields to select surrounding galaxies based on continuum or Lyα emission, depending on the literature. The observation field-of-views and depths are also totally different between these studies, which may introduce some selection bias. In addition, the sample size in each study is usually small (less than five in most cases). Therefore, the recent studies possibly challenge the standard scenario for triggering luminous quasars and imply that there are other triggering mechanisms at high redshift, while more unified analysis of large quasar fields is highly required.

1.2.2 Cosmic Reionization

As the transition phase from the Dark Age to the current universe full of galaxies, cosmic reionization has been discussed especially in the context of formation of first stars and galaxies. Since the first stars are born and accumulate into the first galaxies at $z \sim 10-30$, the UV radiation from these first-generation objects has ionized the surrounding neutral hydrogen in the intergalactic medium (IGM), expanding the ionizing bubbles gradually overlapping with each other, and finally the cosmic reionization has completed at $z \sim 6$, as illustrated in Figure 1.1.

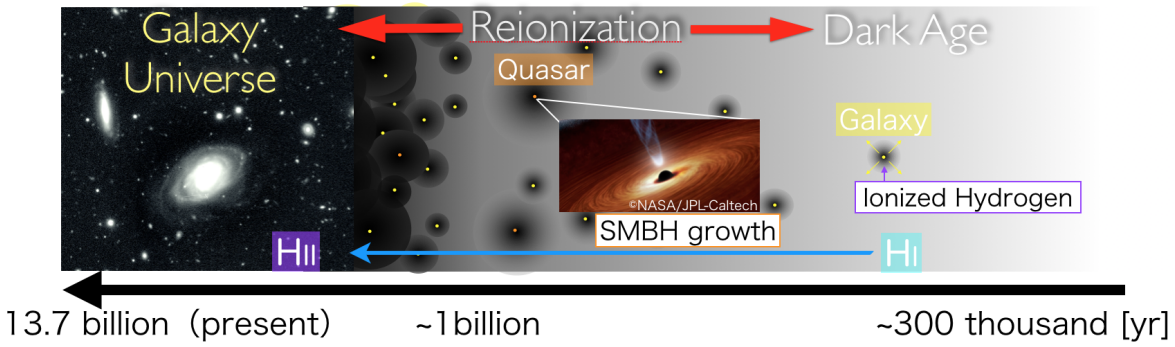

Figure 1.1: Illustration of the cosmic reionization

To observationally constrain the timescale of the reionization process, it is essential to investigate the evolution of the IGM neutral fraction ($x_{\rm HI} \equiv \frac{n_{\rm HI}}{n_{\rm H}}$) in the early universe. In this respect, it has been widely recognized that the continuous Lyman α absorption in the high-redshift quasar spectrum is a good probe of the neutral hydrogen just in front of the quasar along the line of

sight (Gunn & Peterson, 1965). The quasar radiation blueward of Lyman α ($\lambda_{\rm rest} \leq 1215$ Å) is absorbed by the neutral hydrogen gas. While the absorption systems at $z < 5$ can be identified by the individual sharp absorptions at the wavelength corresponding to their redshifts (Lyα forest), the whole transmitted flux in the Lyman α forest reaches to almost zero beyond the reionization epoch due to higher optical depth. This complete absorption feature seen in $z > 6$ quasar spectra (the so-called *Gunn-Peterson trough*) is thought to be the sign that the reionization is in the final stage at this redshift. Fan et al. (2006b) argue that the IGM optical depth increases from $\tau \propto (1+z)^{4.3}$ to $\tau \propto (1+z)^{11}$ at $z > 5.5$. Becker et al. (2015) find that the scatter of the Lyα opacity gets larger at $z \gtrsim 6$. Moreover, it is remarkable that they discover a strong IGM absorption at $z \sim 5.6-5.8$ in one line-of-sight of a $z = 5.98$ quasar, ULAS J0148+0600. This suggests that the reionization process is caused by spatially patchy UV radiation with Lyα opacity fluctuating from field to field even at $z \sim 5.5$. This picture is consistent with the scenario that reionization is induced by the first-generation objects whose special distribution is inhomogeneous.

One issue vigorously discussed is the sources of reionization, namely what kinds of objects the most dominant sources of the ionizing photons are. Low-mass galaxies have been thought to be the major contributors of reionization. The observational studies of $z > 6$ Lyman break galaxies suggest that the slope of the UV luminosity function of galaxies is steep enough to provide sufficient ionizing photons to fully ionize the neutral hydrogen during reionization (e.g., Finkelstein et al., 2015; Bouwens et al., 2017; Ishigaki et al., 2017). However, the problem is that even though the number density of galaxies is well constrained, the actual amount of UV photons escaping from the interstellar medium is unclear. Another possible contributor is quasars because they are the most energetic extragalactic sources, while the number density is much smaller than that of galaxies at the same redshift. Its contribution has been highly uncertain due to the lack of constraints on the faint-end of the quasar luminosity function at high redshift (Willott et al., 2010b; Kashikawa et al., 2015). This is because quasars are rare especially at high redshift and it is difficult to find quasars with ultra-deep but small-area surveys commonly used for the high-redshift galaxy surveys. Also, the previous surveys of $z > 6$ quasars are limited to the most luminous populations. In this sense, it has been highly required to increase the number of low-luminosity quasars at $z > 6$ based on wide and deep surveys.

1.2.3 Early Growth of Super Massive Black Holes

Another important topic probed by high-redshift quasars is the formation and evolution of the super massive black holes (SMBHs). Mortlock et al. (2011) and De Rosa et al. (2014) estimate the black hole mass of ULAS J1120+0641 at $z = 7.085$, the highest-redshift quasar at that time. They show that this quasar has a black hole of $M_{\rm BH} = 2 \times 10^9 M_\odot$, which is in the most massive class of SMBHs throughout the cosmic history. De Rosa et al. (2014) find that three luminous quasars at $z = 6.6 - 6.9$ discovered in Venemans et al. (2013) have the comparable black hole masses. Another extreme example is SDSS J010013+280225, a $z = 6.3$ quasar found in Wu et al. (2015). This quasar is the most luminous quasar at $z > 6$ known with its absolute magnitude of $M_{1450} = -29.26$. They show that, as expected from the brightness, the power source is a SMBH with $M_{\rm BH} \sim 1.2 \times 10^{10} M_\odot$. The existence of such gigantic black holes within the first billion years of the universe puts a severe restrict on the SMBH formation scenario. Based on the so-called Salpeter time (Salpeter, 1964), the growth time of a SMBH from a seed is denoted as

$$t_{\rm grow} = \tau_{\rm salp} \ln\left(\frac{M_{\rm BH}}{M_{\rm seed}}\right) \text{ yr} \tag{1.1}$$

$$= 0.46 \left(\frac{\eta}{1-\eta}\right)\left(\frac{L_{\rm bol}}{L_{\rm Edd}}\right)^{-1} \ln\left(\frac{M_{\rm BH}}{M_{\rm seed}}\right) \text{ Gyr} \tag{1.2}$$

, where η is the radiation efficiency ($L_{\rm bol} = \eta \dot{M} c^2$) and $L_{\rm bol}/L_{\rm Edd}$ is the Eddington ratio. If one assumes that a SMBH with $M_{\rm BH} = 10^9 M_\odot$ at $z = 7$ continuously grows at the Eddington limit (i.e., $L_{\rm bol}/L_{\rm Edd} = 1$) from z_0 ($= 10, 20$) with radiation efficiency of $\eta = 0.1$, the obtained seed black hole mass from equation (1.2) is $M_{\rm seed} = 5 \times 10^6 M_\odot$ ($z_0 = 10$), and $1 \times 10^4 M_\odot$ ($z_0 = 20$), respectively.

There are several scenarios for the seed black hole formation (e.g., Volonteri , 2010; Latif et al., 2016): one is the remnants of Pop-III stars which leave $M_{\rm seed} \sim 10^{2-3} M_\odot$ black holes. The first-generation stars contain no metals, which makes it possible to have such a high mass due to weak mass-loss rates. Another is the “direst-collapse" scenario, which leaves as massive as $M_{\rm seed} \sim 10^5 M_\odot$ seed black holes as a result of the formation of super massive stars with comparable mass. The super massive stars are formed if pristine massive gas clouds are irradiated by far-UV radiation from nearby star-forming galaxies, which destroy molecular hydrogen and suppress Pop-III star formation in the clouds by keeping the virial temperature at $T \gtrsim 10^4 K$ (e.g.,

Omukai, 2001). In addition, Hirano et al. (2017) recently propose that cosmological supersonic gas streams can induce super massive star formation in small dark matter halos, which eventually leaves $\sim 10^5 M_\odot$ black holes at $z \sim 30$. Those scenarios of massive seed black holes could be the formation pathway for the gigantic blackholes observed at high redshift such as the ones found in Mortlock et al. (2011), Wu et al. (2015), and Bañados et al. (2017).

1.3 $z > 6$ Quasar Survey

A number of studies have been trying to discover quasars in the reionization epoch since 2000s, most of which were found by large survey programs. At the time of writing this thesis, the total number of $z > 5.8$ (published) quasars is more than 200. Section 3.2.1 describes the current status of the $z > 6$ quasar survey with Subaru/Hyper Suprime-Cam, in which > 70 are identified including unpublished ones. Here, to express my respects for their tremendous efforts, a brief description of representative quasar surveys and their achievements is given in this section.

The first $z \sim 6$ quasar found is SDSS J1044-0125 at $z = 5.8$ with the absolute 1450Å magnitude of $M_{1450} = -27.2$ (Fan et al., 2000). Starting with this, the Sloan Digital Sky Survey (SDSS) revolutionized the field of high-redshift quasars by constructing 52 quasar samples over $> 10,000$ deg^2 of the northern sky (Fan et al., 2001c, 2003, 2004, 2006a; Jiang, 2008, 2009, 2015; Wu et al., 2015; Jiang et al., 2016; Wang et al., 2017). Jiang et al. (2016) compile the large samples to constrain the quasar luminosity function at the bright end ($-29 \lesssim M_{1450} \lesssim -24$). It is noted that those studies are based on various survey components: (i) SDSS Main, which covers $\sim 15,000$ deg^2, (ii) the SDSS Stripe 82, a ~ 300 deg^2 of the deeper imaging area, and (iii) the SDSS overlap regions, which are parts of the main survey regions (approximately one-fourth of the SDSS main) but were visited multiple times. The overlap regions enable one to select quasar candidates ~ 0.5 magnitude fainter than the those in the non-overlapped regions because multiple visits are helpful to significantly reduce the number of fake sources such as transient objects. Overall, their strategy of quasar selection is to utilize the five optical broad-bands of the SDSS (u, g, r, i, z) to capture the sharp Lyman break in the $z > 6$ quasar spectra. They use $i - z$ color to select $z > 5.7$ quasar candidates, also requiring non-detection in bluer bands. However, since only one color information causes a large number of contaminants such as Galactic M, L, or T

type stars whose surface density is much higher than that of $z \sim 6$ quasars, they also took near-infrared photometry (J, K) to further distinguish quasars from stars.

While the SDSS-Main quasars are limited to the extremely luminous (and thus rare) quasars with $M_{1450} \lesssim -26$, a complemental search of less luminous quasars is the Canada-France High-redshift Quasar Survey (CFHQS, Willott et al. 2007, 2009, 2010b). Over ~ 200 deg^2, 20 $z \sim 6$ quasars $\gtrsim 1$ mag fainter than the SDSS quasars, including an accidentally found ultra-faint quasar, CFHQS J0216-0455 at $z = 6.01$ ($M_{1450} = -22.21$).

The two surveys above are limited up to $z \sim 6.4$ due to their optical color selection. The UKIRT Infrared Deep Sky Survey (UKIDSS) enabled us to select quasars up to $z \sim 7$ (Venemans et al., 2007; Mortlock et al., 2009, 2011; Bañados et al., 2017). Some remarkable discoveries in the 2010s were made from this survey: Mortlock et al. (2011) found the first $z > 7.0$ quasar, ULAS J1120+0641 at $z = 7.1$ and, more than a half decade later, Bañados et al. (2017) broke the highest-redshift record with their discovery of a $z = 7.5$ quasar, ULAS J1342+0928. Vigorous discussions have been made on those discoveries, because it is hard to explain their extremely massive black holes of $M_{\rm BH} \sim 10^9 M_\odot$ with seed black holes of $M_{\rm seed} \sim 10^{2-3} M_\odot$, as already discussed in the previous section.

The followings are the currently ongoing projects. Recently, the Panoramic Survey Telescope & Rapid Response System 1 (Pan-STARRS1) 3π survey has been ongoing to cover the similar parameter space to that of the SDSS in terms of the depth and coverage (Morganson et al., 2012; Bañados et al., 2014; Venemans et al., 2015; Bañados et al., 2016). Bañados et al. (2016) discuss that, from their 77 PS1 quasars, there is a variety in the observed SED, especially on the emission line strength. They discuss that the Lyα equivalent width of $z \sim 6$ quasars are systematically smaller than lower-redshift quasars with a large dispersion with log <EW(Lyα + Nv)>= 1.542 ± 0.391 at $z \sim 6$, while log <EW(Lyα + Nv)>= 1.803 ± 0.205 at $3 < z < 5$ (Diamond-Stanic et al., 2009). Moreover, one notable difference between SDSS and PS1 is that PS1 has a y-band filter, which extends their color selection to $z \sim 7$ with optical observations. Venemans et al. (2015) and Mazzucchelli et al. (2017b) exploit the unique filter set to discover three and six quasars at $6.4 \leq z \leq 6.7$, respectively.

The VISTA Kilo-Degree Infrared Galaxy (VIKING) survey is a recently completed near-infrared survey with the 5σ-depth of $J_{\rm lim} \sim 22$ covering ~ 1500 deg^2 in total, which is composed of north-

ern and southern stripes. The VISTA infrared camera has five broad-band filters (Z,Y, J, H, and Ks) and is consisted of 4×4 detectors, which covers 1.5 deg^2 after continuous mosaicing (or "tiling" in their terminology). Utilizing the relatively deep near-infrared photometry, Venemans et al. (2013) discover three $6.6 \leq z \leq 6.9$ quasars, which are ~ 1 magnitude fainter than ULAS J1120+0641. Their black hole mass is $M_{\rm BH} \sim 10^9 M_\odot$ with high Eddington ratio of $L_{\rm bol}/L_{\rm Edd} = 0.2 - 0.7$ (De Rosa et al., 2014).

The Dark Energy Survey (DES) is an ongoing optical wide-field survey aiming at covering 5000 deg^2. The Dark Energy Camera (DECam) is mounted on the Victor M. Blanco 4-meter Telescope and has a field-of-view of 3 deg^2. Reed et al. (2015) and Reed et al. (2017) utilize this survey for $z > 6$ quasar selection with the g,r,i,z, and y filters, with the 10σ depth of $z \sim 22.3$, to find nine $z \sim 6$ quasars in total at $-27 \lesssim M_{1450} \lesssim -25$ as for now. Note that their candidate selection is unique in the sense that they efficiently separate quasars from Galactic stars in the multi-color space by combining the optical DES photometry with infrared data and selecting candidates based on a template SED-fitting method.

The DECam Legacy Survey (DECaLS) also uses the DECam to cover 9000 deg^2 with g, r, and z bands with the approximate 5σ-depth of $g_{\rm lim} \sim 24.7$, $r_{\rm lim} \sim 23.9$, and $z_{\rm lim} \sim 23.0$. This survey is meant to provide spectroscopic targets $\gtrsim 1$ mag fainter than the SDSS for the Dark Energy Spectroscopic Instrument (DESI) survey. Wang et al. (2017) combine the DECaLS and the near-infrared UKIRT Hemishere Survey (UHS) photometry to (5σ depth: $J_{\rm lim} \sim 19.6$ Vega mag) find two $z \sim 6$ quasars and one at $z = 6.63$ with their absolute magnitudes of $M_{1450} \sim -26$.

There are other smaller projects such as the Infrared Medium-deep Survey (IMS) (Kim et al., 2015), Very Large Telescope Survey Telescope (VST) ATLAS survey (Carnall et al., 2015), and Subaru (Kashikawa et al., 2015; Onoue et al., 2017, see Chapter 2).

1.4 The HSC-SSP survey

The Hyper Suprime-Cam (HSC, Miyazaki et al. (2012)) is a new optical camera installed at the prime focus of the Subaru telescope. With the 8.2m mirror of the Subaru, ten minutes imaging goes as deep as $r_{\rm lim,5\sigma} \sim 26$, which is three magnitudes deeper than the Sloan Digital Sky Survey (SDSS, York et al. (2000)). The most characteristic feature of the HSC is its gigantic field-of-view

of 1.5 degree diameter. Taking advantage of the survey efficiency of the camera, the HSC Subaru Strategic Program (HSC-SSP) covers 1400 deg^2 with its five broad-band filters in the Wide layer[1]. This survey is a five-year survey, which began in March 2014. Its first ~ 100 deg^2 data of the Wide, Deep and UltraDeep layers has been open to public since February 2017 (Aihara et al., 2017a). As of January 9, 2018, the total area covered by the five optical bands in the Wide layer is 340 deg^2 [2]. The sky coverage of the HSC-SSP is shown in Figure 1.2. Thanks to the 8m prime mirror of the Subaru and its unique capability of wide-field imaging with the HSC, the HSC-SSP survey is currently one of the most competitive optical surveys in the world.

1.5 Objectives

The main objectives of this thesis are to tackle the mysteries of the cosmic dawn and quasars raised in the previous sections. Specifically, there are two main topics that this thesis approaches:

1. **How much ionizing photons do quasars provide in the reionization epoch?** (Chaper 2)
2. **How are the general super massive black holes in the reionization epoch massive and active?** (Chaper 3)

Throughout the thesis, the keyword is the wide-field surveys. Regarding the quasar luminosity function, the low-luminosity quasars are hard to find due to survey depths and their small number density compared to galaxies at the same redshift. Furthermore, $z > 6$ quasars discovered in the previous surveys are highly biased toward the most massive and active super massive black holes, which has prevented one from addressing the characteristics of general black hole growth at high redshift. Given such a situation, we make use of the unique photometric data of the Subaru telescope, a 8.2m-telescope at the summit of Mauna Kea, Hawaii. The strength of the telescope compared with other ground-based 8-10m-class telescopes is that Subaru has a capability of prime-focus instruments, which enable us to image the sky with a wide field-of-view. Utilizing the advantage of Subaru, we shed a light on the understandings of the high redshift universe from various points of view with the combination of deep and wide fields-of-view.

[1] For more information of the HSC-SSP survey, we encourage readers to refer to the public data release paper (Aihara et al., 2017a) and the survey design paper (Aihara et al., 2017b). The filter information is given in Kawanomoto et al. (2017)

[2] From an internal website of the HSC-SSP collaboration

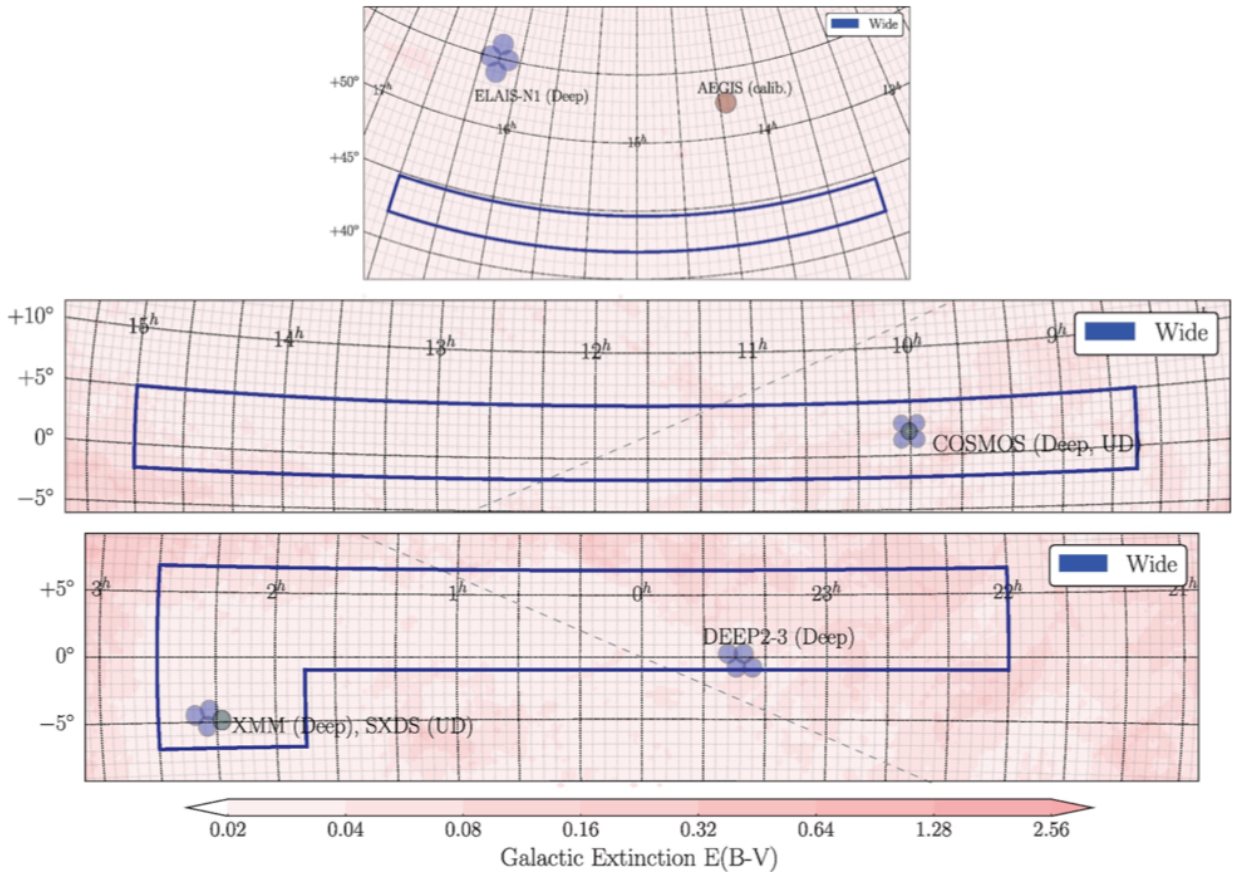

Figure 1.2: The HSC-SSP coverage in which HSC-Wide area is shown in blue rectangles. Background color indicates the Galactic extinction $E(B-V)$. This figure is from the survey design paper of the HSC-SSP (Aihara et al., 2017b).

1.6 Structure of the Thesis

This doctoral thesis is organized as follows. Chapter 1 introduces the general background of the topics discussed in this thesis. We discuss the contribution of quasars to reionization in Chapter 2, based on our deep imaging survey of $z \sim 6$ quasars with Subaru/Suprime-Cam. We extend the high redshift quasar survey with the HSC-SSP, which is described in Chapter 3. Thanks to the unprecedented coverage with deep imaging with the Subaru/HSC, we have succeeded in identifying a large number of low-luminosity quasars at $z = 6-7$ as described in the first part of this chapter. Then, we show the black hole mass measurements of five quasars with our deep near-infrared spectroscopy with Gemini/GNIRS and VLT/XSHOOTER. Finally, we give a summary in Chapter 4 and describe our future prospects on these studies.

In Appendix, Chapter A shows a related work to the main body of the thesis, in which we investigate the quasar environments at $z = 3-4$ and $z \sim 1$ with the HSC-SSP, especially focusing on the extreme cases in which more than one luminous quasars are in pair.

Throughout the thesis, we adopt a standard ΛCDM cosmology with $H_0 = 70$ km s^{-1} Mpc^{-1}, $\Omega_m = 0.3$, $\Omega_\Lambda = 0.7$, and $\Omega_b h^2 = 0.022$. Magnitudes are given in the AB system unless otherwise stated.

Chapter 2

Minor Contribution of Quasars to Ionizing Photon Budget at $z \sim 6$: Update on Quasar Luminosity Function at the Faint-end with Subaru/Suprime-Cam

We constrain the quasar contribution to cosmic reionization based on our deep optical survey of $z \sim 6$ quasars down to $z_R = 24.15$ using Subaru/Suprime-Cam in three UKIDSS-DXS fields covering 6.5 deg^2. In Kashikawa et al. (2015), we select 17 quasar candidates and report our initial discovery of two low-luminosity quasars ($M_{1450} \sim -23$) from seven targets, one of which might be a Lyα emitting galaxy. From an additional optical spectroscopy, none of the four candidates out of the remaining ten turn out to be genuine quasars. Moreover, the deeper optical photometry provided by the Hyper Suprime-Cam Subaru Strategic Program (HSC-SSP) shows that, unlike the two already-known quasars, the $i-z$ and $z-y$ colors of the last six candidates are consistent with M- or L-type brown dwarfs. Therefore, the quasar luminosity function (QLF) in the previous paper is confirmed. Compiling QLF measurements from the literature over a wide magnitude range, including an extremely faint AGN candidate from Parsa et al. (2017), to fit them with a double power-law, we find that the best-fit faint-end slope is $\alpha = -2.04^{+0.33}_{-0.18}$ ($-1.98^{+0.48}_{-0.21}$) and characteristic magnitude is $M^*_{1450} = -25.8^{+1.1}_{-1.9}$ ($-25.7^{+1.0}_{-1.8}$) in the case of two (one) quasar detection. Our result suggests that, if the QLF is integrated down to $M_{1450} = -18$, quasars produce $\sim 1-12\%$ of the ionizing photons required to ionize the whole universe at $z \sim 6$ with 2σ confidence level, assuming that the escape fraction is $f_{\rm esc} = 1$ and the IGM clumpy factor is $C = 3$. Even when the systematic uncertainties are taken into account, our result supports the scenario that quasars are the minor contributors of reionization.

2.1 Introduction

High-redshift ($z \gtrsim 6$) quasars are unique probes of the early universe in a way complementary to other populations such as galaxies and gamma-ray bursts. In particular, they can be used to estimate the hydrogen neutral fraction of the intergalactic medium (IGM), which directly probes the

cosmic reionization history (Fan et al., 2006c). Furthermore, the existence of the most massive ($M_{\rm BH} > 10^9 M_\odot$) supermassive black holes at this epoch poses a challenge to the seed black hole formation and early growth scenario (e.g., Mortlock et al., 2011; Wu et al., 2015). Submillimeter studies (Venemans et al., 2016; Wang et al., 2016) have derived an implication that such gigantic black holes evolve faster than their host galaxies when compared to the local $M_{\rm BH} - M_{\rm bulge}$ relation (Magorrian et al., 1998; Kormendy & Ho, 2013). A flat metallicity evolution of the quasar hosts has been suggested up to $z \sim 7$ (Jiang et al., 2007; De Rosa et al., 2014).

Searches of $z > 5.7$ quasars have been performed in large optical and near-infrared surveys, namely SDSS (Fan et al., 2006c; Jiang et al., 2016), CFHQS (Willott et al., 2010b), UKIDSS (Mortlock et al., 2011), VIKING (Venemans et al., 2013), DECaLS (Wang et al., 2017), DES (Reed et al., 2017), PS1 (Bañados et al., 2016), and HSC (Matsuoka et al., 2016, 2018), which have identified more than two hundred quasars to date. Thanks to the large sample size, the bright end of the quasar luminosity function (QLF) is well constrained (e.g., Jiang et al., 2016). However, the photon budget of quasars, i.e., how much ionizing photons quasars emit to reionize the universe is still an outstanding issue as the QLF faint-end, which is crucial in the photon budget estimate, is poorly constrained. It has been based on three (or two) quasars at the faintest range ($M_{1450} \sim -22$) which are spectroscopically identified in Willott et al. (2010b) and Kashikawa et al. (2015, hereafter K15). Whereas these optical studies suggest insufficient contribution of quasars, Giallongo et al. (2015) propose a scenario that faint AGN are the major contributors in the ionizing background radiation at $4 < z < 6$, based on their 22 extremely faint ($M_{1450} \sim -20$) AGN candidates in the GOODS-South field, five of which are at $z \sim 5.75$. Their X-ray fluxes are detected in deep X-ray 4Ms *Chandra* images. Following this paper and the discovery of a long and dark Lyman alpha trough in a $z \simeq 6$ quasar spectrum (Becker et al., 2015; Chardin et al., 2017), such AGN-driven reionization scenario has recently been vigorously discussed in, for example, Madau & Haardt (2015). However, Parsa et al. (2017) show that, through their individual examination of the X-ray images and photometric redshift considering a wide range of dust reddening in their galaxy and AGN template SEDs, only seven of the $z > 4$ AGN candidates are robust, among which one is at $z > 5$. Several other deep X-ray studies also report discrepancy with the Giallongo et al. (2015) results (Vito et al., 2016; Ricci et al., 2017). The photon budget issue has also been discussed with the UV luminosity function of Lyman break galaxies (e.g., Finkelstein et

al., 2015; Bouwens et al., 2017), which is well constrained down to $M_{\rm UV} \sim -13$. However, unclear understanding of the escape fraction of UV photons and the magnification uncertainties in the gravitational lensing prevent one from making a convincing conclusion on which population, galaxies or AGN is the dominant contributor of the reionization. This argument is particularly essential for estimating the typical size of the ionizing bubble, which essentially depends on the ionizing sources.

In this *Chapter*, we update our deep survey of $z \sim 6$ quasars with Subaru/Suprime-Cam (Miyazaki et al., 2002), the initial results of which are reported in K15.

2.2 Subaru/Suprime-Cam Observation and Previous Results

We observed 6.5 deg^2 in total consisting of three UKIDSS-DXS fields (Lockman Hole, ELAIS-N1, VIMOS 4) on June 22–24, 2009 (UT) exploiting two broad bands of the Suprime-Cam: z_B ($\lambda_{\rm eff}$ = 8842Å) and z_R ($\lambda_{\rm eff}$ = 9841Å) with 3σ depth[1] of 25.55 and 24.15, respectively. CFHTLS i'-band ($\lambda_{\rm eff}$ = 7571Å) images are provided in VIMOS 4 field with $i'_{{\rm lim},3\sigma} \sim 25.7$[2]. Suprime-Cam i'-band ($\lambda_{\rm eff}$ = 7641Å) images are available in Lockman/ELAIS fields with $i'_{{\rm lim},3\sigma} \sim 26.42$. UKIDSS J- and K-band images are also available over the three fields with $J_{{\rm lim},3\sigma} = 23.84$ and $K_{{\rm lim},3\sigma} = 23.17$. In K15, we select 17 candidates at $23.65 \leq z_R \leq 24.11$ from stellar objects applying following color selection: i) $i'-z_B > 1.7$, ii) $z_B-z_R < 1.0$, iii) $i'-z_B > 2(z_B-z_R)+0.9$, which can effectively distinguish quasars from contaminants such as Galactic brown dwarfs. We ignore the difference of the two i'-band filters causing $\Delta i' < 0.01$ mag difference for a $z \sim 6$ quasar. The observed magnitudes and coordinates of the candidates are listed in Table 3 of K15 and Table 2.1 of this paper with new photometry. From our initial follow-up spectroscopy with Subaru/FOCAS (Kashikawa et al., 2002), we discovered two $z \sim 6$ quasars out of seven targets, giving an initial constraint on the QLF faint-end. Figure 2.1 show their optical spectra from Kashikawa et al. (2015) taken by Subaru/FOCAS. That paper suggests that quasars are responsible for $5-15\%$ of the ionizing photons at $z \sim 6$, but we could only give a lower-limit due to the remaining ten candidates yet to be identified. Note that ELAIS1091000446 (z_R = 24.2) at z = 6.04, one of the discovered quasars has an unusual Lyα profile with its half-line width of 427 km s^{-1}, which falls

[1] 2"ϕ-aperture limiting magnitude
[2] See Section 2.4.2.

between those of typical quasars (> 1000 km s^{-1}) and Lyman break galaxies (~ 100 km s^{-1}), while the other one, VIMOS2911001793 ($z_R = 23.7$) at $z = 6.16$ is a typical $z \sim 6$ quasar with a broad Lyα (1732 km s^{-1}).

2.3 Follow-up Spectroscopy

We performed optical spectroscopy for four of the remaining candidates (VIMOS2873003200, ELAIS891006630, ELAIS914002066 and ELAIS914003931) with Subaru/FOCAS (S15B-204S & S16A-200S, PI: M.Onoue). We selected the targets with relatively red $i' - z_B$ colors among the ten. Our program was executed on September 8, 2015 for the first two targets and May 14, 2016 (UT) for the last two. We used 300R grism with an order-cut filter O58 to cover $5800-10450$ Å with a spectral resolution of $R \sim 500$ (0".8-slit width). Each target was observed for about two hours, divided into six 1020 sec (September run) and 1077 sec (May run) exposures. Within the six exposures, three-point dithering (-1".0, 0".0, $+1$".0) was applied for good background subtraction. Two-pixel CCD on-chip binning in the spatial direction (0".104 per pix) was applied. Nearby reference stars were used to securely put the faint targets on the slit. Standard star (BD+33d2642) spectra were also taken for absolute flux calibration. The sky conditions were clear with $0".4 - 0".7$ seeing size. The data was reduced with a standard procedure using an IRAF-based FOCAS pipeline. The individual 2D spectra were median stacked and reduced to final 1D spectra.

As a result, we find that none of the four targets are quasars. The continuum flux of VIMOS2873003200 ($z_R = 23.78$) is detected all over the spectral coverage with a doublet emission line at $\lambda_{\rm obs} \sim 8770$ Å, which is likely a [OII] doublet $\lambda\lambda 3726$ 3729 at $z = 1.354$. Note that another [OII] emitter (Lockman14004800) was found in K15. The other three ELAIS targets are not detected. As we describe in Section 2.4.2, these are also undetected in deeper photometric observation with Subaru/HSC.

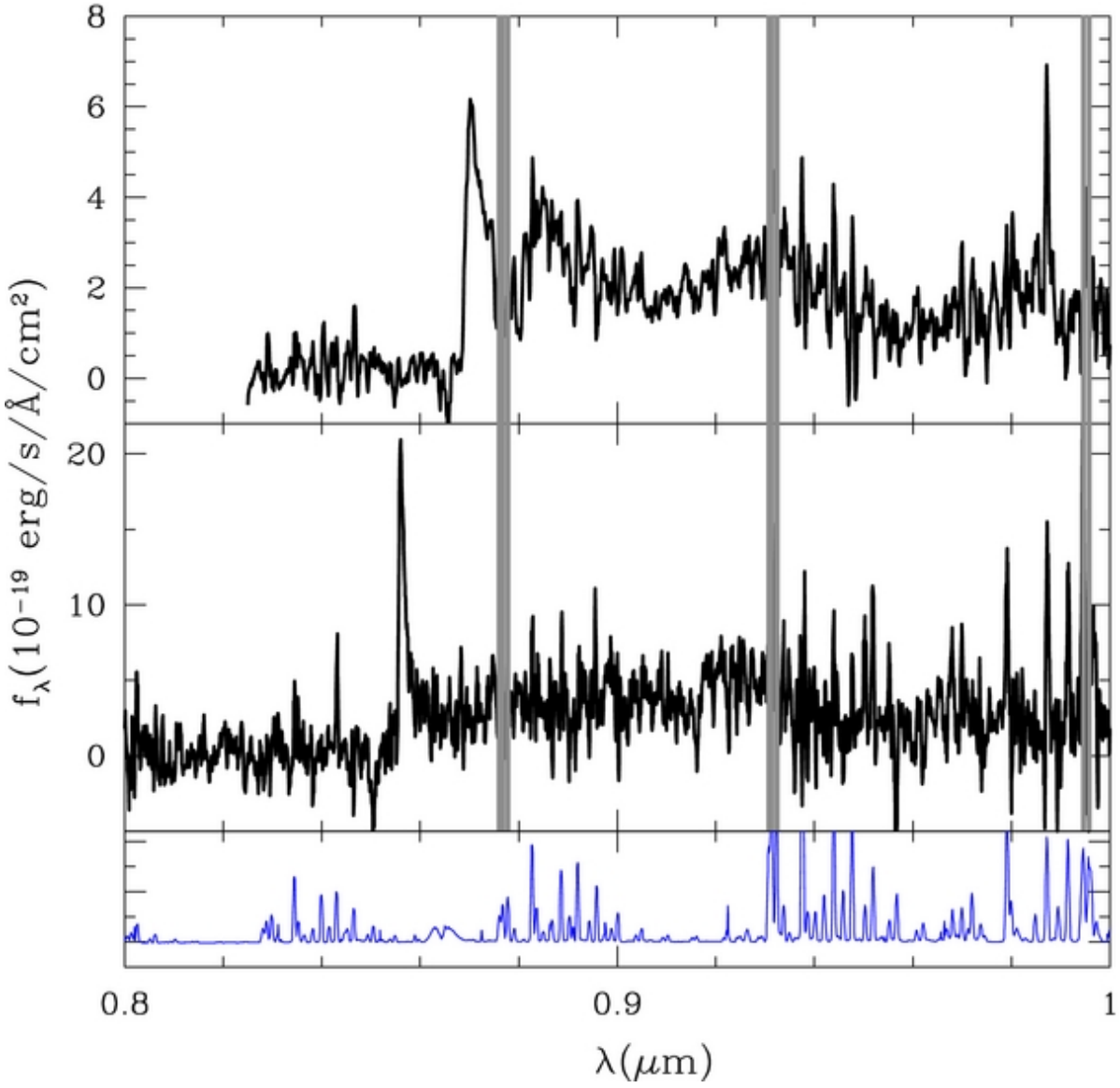

Figure 2.1: Optical spectra of the two quasars discovered with our Subaru/Suprime-Cam survey at $z \sim 6$. The upper panel shows VIMOS2911001793 ($z = 6.156$) and the middle panel shows ELAIS1091000446 ($z = 6.041$). The wavelength ranges affected by strong sky emission lines are shaded. The bottom panel is the sky spectrum.

2.4 The HSC Colors

2.4.1 Last Six Candidates

This Suprime-Cam survey of $z \sim 6$ quasars was originally positioned as a pre-study for a much larger survey, the Hyper Suprime-Cam Subaru Strategic Program (HSC-SSP), of which the detailed design and the survey strategy are given in Aihara et al. (2017a,b). Fortunately, ELAIS-N1 and VIMOS 4 fields are covered in the HSC-Deep and Wide layers, respectively. We leverage the latest internal photometric catalog of the HSC-SSP (DR S16A) to inspect the last six candidates. The average 5σ depths of the PSF magnitude in Wide (Deep) are $g \sim 26.8$ (~ 26.8), $r \sim 26.4$ (~ 26.6), $i \sim 26.4$ (~ 26.5), $z \sim 25.5$ (~ 25.6), and $y \sim 24.7$ (~ 24.8). The filter information of the HSC is described in Kawanomoto et al. (in prep.).

Figure 2.2 shows the $i-z$ and $z-y$ color diagram of 13 candidates detected in the HSC-SSP. The solid line shows the quasar color track at $5 < z < 7$ and the grey symbols show the colors of brown dwarfs, which are derived from the SED templates of the BTsettl model (Allard et al., 2013)[3]. As a result, we find that, using the same color selection used in K15, only the two already-identified quasars have strong color excess in $i-z$. One of the six unclassified candidates, VIMOS2773005145 shows moderately-red colors in $i-z$ and $z-y$, which are indicative of a L-type brown dwarf. The $i-z$ colors of the other five are not as red as expected for $z \sim 6$ quasars ($0.4 \leq i-z \leq 1.3$) and rather consistent with M-type brown dwarfs, which is also the case for other non-quasars spectroscopically followed-up in K15[4]. Conclusively, the deeper HSC photometry shows that there are no additional quasars in our remaining candidates. The HSC photometry is summarized in Table 2.1.

2.4.2 The Difference of S-Cam & HSC Colors

We suspect that the different colors of the candidates between the S-Cam+CFHT and HSC filter sets are caused by different imaging depths. The HSC-Wide is deeper by 0.5 and 1.3 mag in i (S-Cam and CFHT i', respectively), 0.5 mag in z (z_B) and 1.1 mag in y (z_R). While the candidates are detected in z_B and z_R with more than 7σ significance, they are faint in i' with $\lesssim 1\sigma$ detections.

[3] Solar metallicity models are used.
[4] VIMOS2871007103 is likely a low-z interloper as it is detected in g and r. See Table 2.1.

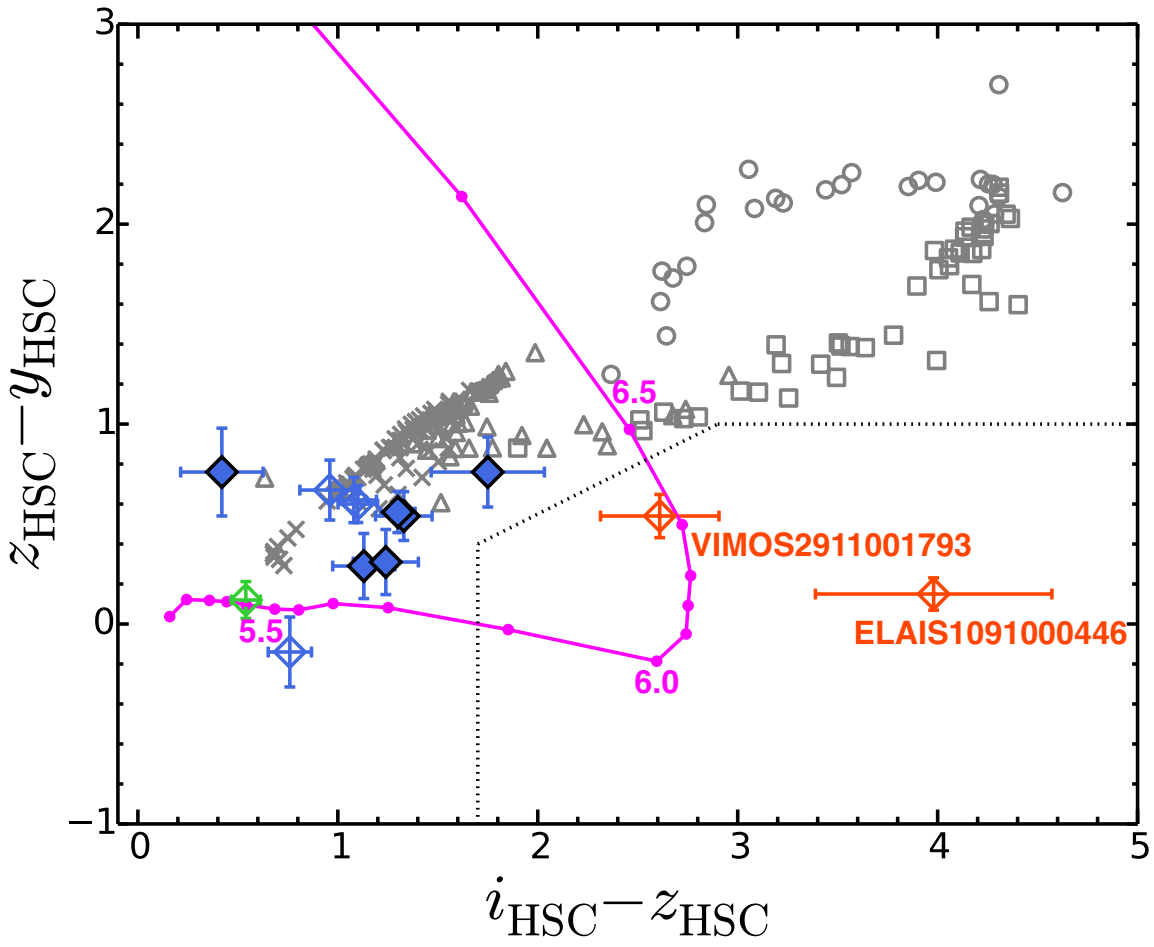

Figure 2.2: HSC $i-z$ and $z-y$ color diagram of the 13 quasar candidates detected in the HSC-SSP. The red, green, and blue diamonds show the quasars (VIMOS2911001793, ELAIS1091000446), [OII] emitter, and other sources, respectively. Spectroscopically-identified candidates are shown in open symbols and the other six are shown in filled symbols. The model color track of $5 < z < 7$ quasars are shown in a solid line with steps of $\Delta z = 0.1$. Note that strong IGM absorption at Lyα makes the observed $i-z$ color red. The model colors of M (cross), L (triangle), T (square), and Y-type (circle) brown dwarfs from the BTsettl model (Allard et al., 2013) are shown in grey. The color selection window applied in K15 is shown in a dotted line.

Therefore, it can be said that the deeper imaging of the HSC helps derive robust optical colors of the candidates. Moreover, we find that our previous estimate of the limiting magnitude of i'-band was slightly optimistic in the VIMOS field. We re-evaluated the i'-band depth based on the distribution of background levels within 2"ϕ-apertures at randomly selected positions on the images. The depth was found to be systematically shallower by ~ 1 mag than the one in K15, with a large field-to-field variation of 0.6 mag partly due to heavy galactic cirrus ($A_V \sim 0.16$ mag, Schlafly & Finkbeiner, 2011). The total effective volume is evaluated to be at most $\sim 25\%$ smaller than in K15, given their selection completeness.

The three ELAIS candidates undetected in the FOCAS spectroscopy (Secion 2.3) are also undetected in the HSC-SSP images: $\gtrsim 3$ mag fainter than in z_B and z_R. Considering the rest-frame UV variability of quasars ($\lesssim 1$ mag, Welsh et al., 2011), they are likely to be either moving or transient objects in the Suprime-Cam images taken on continuous days, rather than variable quasars. The [OII] emitter found in this paper, VIMOS2873003200 is also detected in bluer g- and r-bands with $> 10\sigma$ significance. Note that there are other quasar candidates in ELAIS and VIMOS at the similar magnitude range of the K15 candidates, if we only use the deeper HSC colors. However, it is a natural consequence considering the low completeness in our Supreme-Cam selection ($\lesssim 50\%$). We will discuss them in the series of the HSC quasar papers (Matsuoka et al., 2016, 2018; Akiyama et al., 2017).

2.5 Discussion

2.5.1 $z \sim 6$ QLF

As we find no additional quasars from the remaining candidates, our previous constraint on the binned QLF in K15 is confirmed. In Figure 2.3, the binned QLF from our Suprime-Cam survey (K15 and this study) is shown in brown (two quasars) and red (one quasar) open circles with Poisson error bars. We do not correct for the effect of the shallow imaging in the VIMOS field, because we find that it only increases the ionizing photon emissivity of quasars by $\lesssim 6\%$, which is negligible within our QLF constraints. We also show the binned QLF of the CFHQS (Willott et al., 2010b, magenta) and those of the SDSS (Jiang et al., 2016, green) in squares (SDSS-Main),

Table 2.1: HSC photometry of 17 candidates

Object	g	r	i	z	y	Notes
Candidates followed-up in Kashikawa+15						
VIMOS2911001793	>28.5	>28.1	27.49±0.59	23.51±0.04	23.36±0.07	$z = 6.156$ QSO
ELAIS1091000446	28.56±0.67	27.41±0.54	27.03±0.29	24.42±0.06	23.88±0.09	$z = 6.041$ QSO
Lockman14004800	···	···	···	···	···	[OII] emitter
VIMOS2832005555	>28.5	27.96±1.08	25.09±0.07	23.99±0.07	23.39±0.06	ND
VIMOS2871008551	>28.5	>28.1	25.63±0.09	24.67±0.12	24.00±0.09	ND
VIMOS2871007103	25.92±0.07	25.64±0.11	25.09±0.06	24.33±0.09	24.47±0.15	ND
VIMOS3031005637	>28.5	26.53±0.28	25.40±0.08	24.32±0.08	23.70±0.08	ND
Remaining candidates						
VIMOS2873003200	24.74±0.03	24.56±0.04	24.40±0.04	23.86±0.06	23.74±0.07	[OII] emitter
ELAIS891006630	>28.5	>28.3	>28.2	>27.3	>26.5	ND
ELAIS914002066	>28.5	>28.3	>28.2	>27.3	>26.5	ND
ELAIS914003931	>28.5	>28.3	>28.2	>27.3	>26.5	ND
VIMOS2752003989	>28.5	27.79±0.79	25.54±0.10	24.21±0.10	23.67±0.07	likely BD
VIMOS2773005145	>28.5	>28.1	26.35±0.24	24.60±0.15	23.84± 0.09	likely BD
VIMOS2833009245	>28.5	>28.1	25.64±0.11	24.51±0.11	24.22±0.12	likely BD
VIMOS2853001577	>28.5	>28.1	25.26±0.08	24.84±0.19	24.08±0.11	likely BD
VIMOS2733006446	>28.5	>28.1	25.76±0.11	24.52±0.12	24.21±0.11	likely BD
VIMOS2993006408	>28.5	>28.1	25.52±0.07	24.22±0.05	23.66±0.09	likely BD

Notes: 1σ limiting magnitude is shown for undetected bands. Lockman field is not covered in the HSC-SSP. In the last column, candidates undetected in the spectroscopic follow-up are shown as “ND", while candidates not targeted in the spectroscopy and showing stellar-like HSC colors are shown as “likely BD". The S-Cam photometry can be found in K15.

triangles (Overlap region), and diamonds (Stripe 82). The AGN luminosity functions derived in Giallongo et al. (2015, blue) and Parsa et al. (2017, cyan) are also shown at $-21 \leq M_{1450} \leq -19$, while it should be noted that their luminosity functions are based on AGN "candidates" with large uncertainties on the photometric redshift (see Parsa paper for detailed discussions) and host galaxy contribution may not be negligible in the rest-frame UV luminosity for such ultra-faint sources (Ricci et al., 2017). To calculate the shape of the $z \sim 6$ QLF, $\Phi(M_{1450}, z)$, we fit the binned QLF with a double power-law:

$$\Phi(M_{1450}, z) = \frac{10^{k(z-6)}\Phi^*(z)}{10^{0.4(\alpha+1)(M_{1450}-M^*_{1450})} + 10^{0.4(\beta+1)(M_{1450}-M^*_{1450})}}, \tag{2.1}$$

where α and β are the faint- and bright-end slopes, respectively, M^*_{1450} is the characteristic magnitude, and k is the parameter showing the redshift evolution. The scale factor $\Phi^*(z)$ is a function of redshift. We fix the bright-end slope as $\beta = -2.8$ following the SDSS result (Jiang et al., 2016) since our data point is at the faint side. The LFs of Giallongo et al. (2015) and Parsa et al. (2017) at $z = 5.75$ are scaled to $z = 6.0$ using $k = -0.47$, which is derived in Fan et al. (2001c). Since the faintest bins of Willott et al. (2010b) and ours are based on discovery of only one ($M_{1450} = -22.21$) and two quasars ($M_{1450} = -23.10, -22.58$), we combine the two individually determined bins into one as also applied in K15. These re-binned QLFs are shown in filled circles in Figure 2.3 and used in the following analysis. We assume two cases in which two quasars are detected (case 1), and one quasar is detected (case 2) in our survey due to the unclear classification of ELAIS1091000446. In order to estimate the best-fit combination of (α, M^*_{1450}), we fit the double power-law using χ^2 minimization to the binned QLFs shown in filled symbols in Figure 2.3, namely the SDSS, CFHQS, our study (re-binned with CFHQS), and the X-ray selected AGN candidate from Parsa et al. (2017). Note that the scale-factor, $\Phi^*(z = 6)$ is determined so that the minimum χ^2 is achieved at each (α, M^*_{1450}).

As a result, we derive (α, M^*_{1450}) = ($-2.04^{+0.33}_{-0.18}$, $-25.8^{+1.1}_{-1.9}$) with the scale factor $\Phi^*(z = 6) = 4.06 \times 10^{-9}$ Mpc^{-3} mag^{-1} for the case 1 and (α, M^*_{1450}) = ($-1.98^{+0.48}_{-0.21}$, $-25.7^{+1.0}_{-1.8}$) with the scale factor $\Phi^*(z = 6) = 4.53 \times 10^{-9}$ Mpc^{-3} mag^{-1} for the case 2. These best-fit QLFs are shown in solid lines in Figure 2.3. In both cases, the best-fit parameters are consistent with the QLF in Jiang et al. (2016) within 1σ level, while they also use the K15 and Willott et al. (2010b) results (assuming

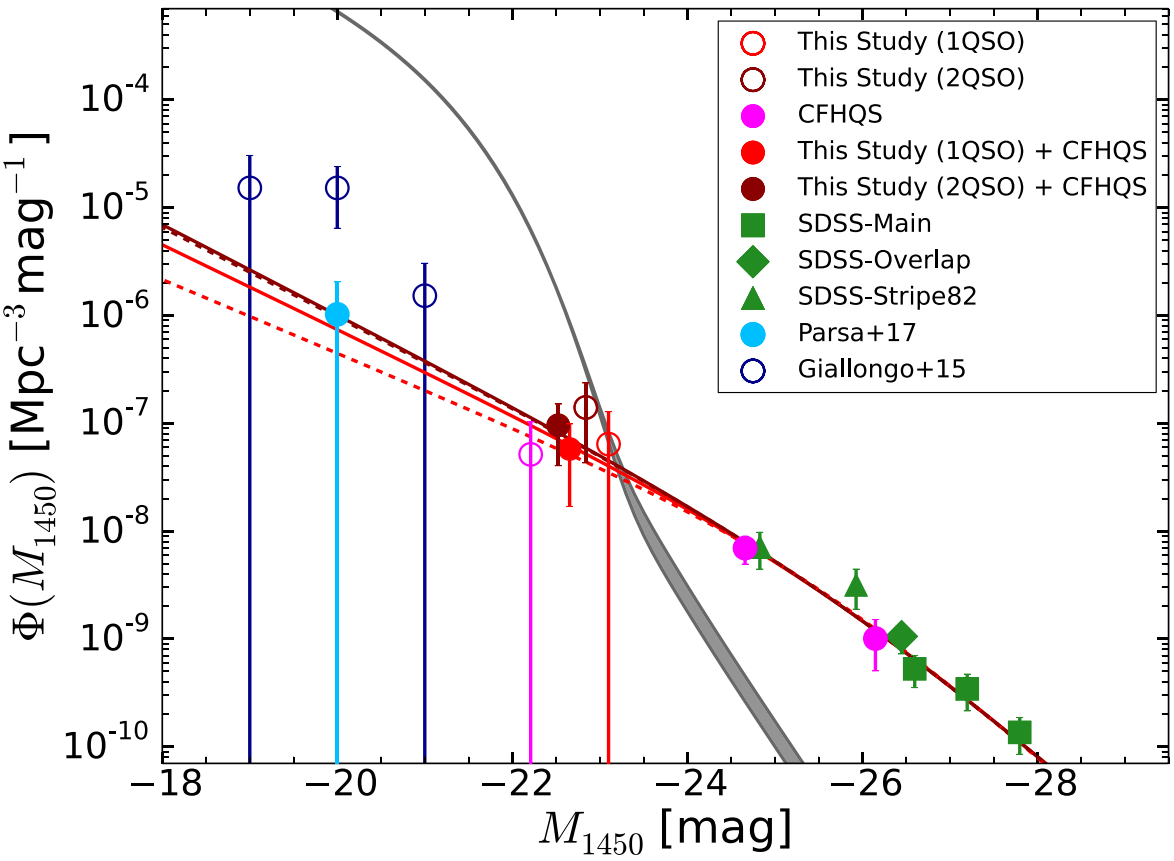

Figure 2.3: $z \sim 6$ QLF. The binned QLF from K15 and this study is shown in brown (case 1) and red (case 2) open symbols, respectively, with the re-binned QLFs with the faintest bin of the CFHQS (Willott et al., 2010b, magenta) shown in filled symbols. The SDSS data points (Main, Overlap, Stripe82) from Jiang et al. (2016) are shown in green (squares, diamonds, and triangles). AGN luminosity functions from Parsa et al. (2017, cyan) and Giallongo et al. (2015, blue) are scaled to $z = 6.0$ using $k = -0.47$. The best-fit double power-laws (using all the filled symbols) are shown in solid lines, while those fitted without the Parsa et al. (2017) bin are shown in dashed lines. The shaded grey line shows the UV luminosity function of i-dropout galaxies from Ono et al. (2017, lensed Schechter function), which intersects with the QLFs at $M_{1450} \simeq -23$.

one quasar in K15). To estimate the uncertainty of the faint-end slope and the characteristic magnitude, we fit the QLF with fixed (α, M^*_{1450}) over $-2.50 \leq \alpha \leq 0.00$ and $-31.0 \leq M^*_{1450} \leq -22.0$ with steps of $\Delta\alpha = 0.01$ and $\Delta M_{1450} = 0.1$. In Figure 2.4, the two-dimensional 1σ and 2σ confidential ranges are shown in red (case 1) and blue (case 2) contours with the best-fit values. We also fit the QLFs excluding the Parsa et al. (2017) bin, and find that the number densitiy at the faint-end slightly decreases, which are indicated in dashed lines in Figure 2.3. Table 2.2 summarizes our best-fit QLF parameters.

We repeat the QLF fitting by replacing the Parsa et al. (2017) bin with those of Giallongo et al. (2015), assuming two quasars from our survey. The derived QLF is not strongly different from the above results, and the faint-end slope is required to be much steeper ($\alpha = -2.15$) than their measurement ($\alpha = -1.66$). Note that the best-fit power-law falls at smaller densities than Giallongo et al. (2015) in all bins, while the goodness-of-fit is reasonable ($\chi^2_\nu = 0.9$) partly due to the large uncertainties in their constraints. In addition, the total number density of quasars when the QLF is integrated down to $M_{1450} = -18$ is only 25% of theirs.

When our best-fit QLFs are compared to lower redshifts, there is a trend that, albeit with a large uncertainty, the faint-end slope gets steeper from $z \sim 4$ ($\alpha = -1.30 \pm 0.05$, Akiyama et al., 2017), which is indicative of the supermassive black holes in their actively growing phase at $z > 6$.

2.5.2 Photon Budget of Quasars during Reionization

The ionizing photon emissivity of $z \sim 6$ quasars is calculated from the QLFs derived in the previous section, following the framework given in Bolton & Haehnelt (2007). In this paper, we assume a broken power-law for the rest-frame SED of a quasar: $f_\nu \propto \nu^{-0.6}$ ($\lambda \leq 912$Å) and $f_\nu \propto \nu^{-1.7}$ ($\lambda_{\rm rest} > 912$Å), which is given in Lusso et al. (2015). We integrate the QLF from $M_{1450} = -30$ to -18 mag using the best-fit double power-law at each frequency to derive the monochromatic emissivity. Then, it is converted to the hydrogen ionization rate assuming that all ionizing photons ($\lambda \leq 912$Å) emitted from quasars escape to the IGM, from which the ionizing photon emissivity per unit comoving volume, $\dot{N}_{\rm ion}$ is derived. Based on our best-fit QLFs, we find $\dot{N}_{\rm ion} = 1.63 \times 10^{49}$ s^{-1} Mpc^{-3} (case 1) and $\dot{N}_{\rm ion} = 1.34 \times 10^{49}$ s^{-1} Mpc^{-3} (case 2). The required emission rate to balance with the hydrogen recombination at $z = 6$ is $\dot{N}_{\rm ion} = 10^{50.48}$ $(3/C)$ s^{-1}

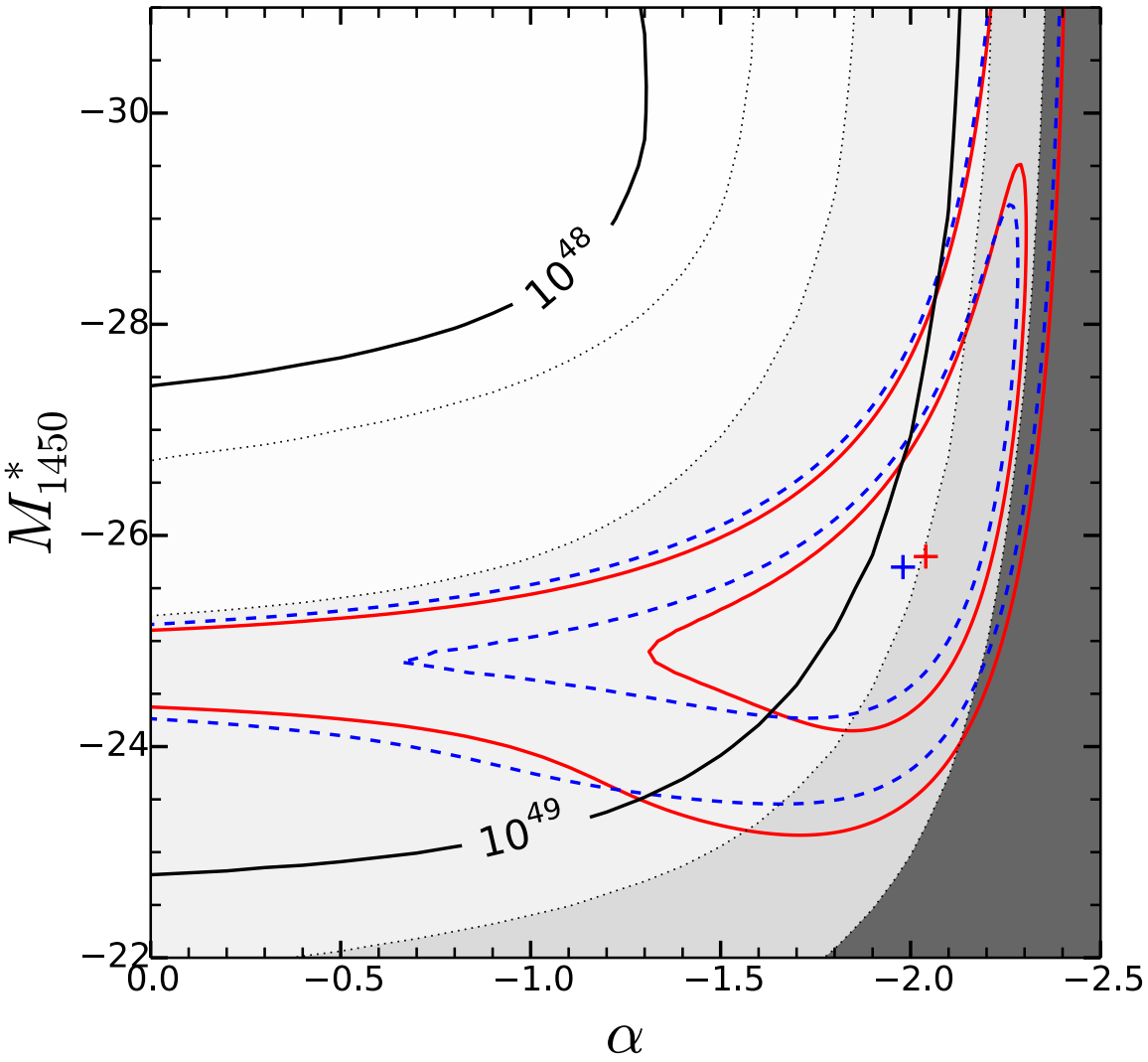

Figure 2.4: Constraints on the QLF faint-end slope α and characteristic absolute magnitude M^*_{1450}. The 1σ and 2σ confidence ranges are shown in red and blue contours, respectively, with the best-fit indicated in plus signs. The ionizing emissivity of quasars, $\dot{N}_{\rm ion}$ [s^{-1} Mpc^{-3}] for each (α, M^*_{1450}) is indicated in solid lines assuming case 1 and the corresponding photon budget is shown in shades (10, 5, 1, 0.5% from right to left).

Table 2.2: Best-fit QLF Parameters

Case	α	M^*_{1450} (mag)	$\Phi^*(z=6)$ ($\times 10^{-9}$ Mpc^{-3} mag^{-1})	$\dot{N}^a_{\rm ion}$ ($\times 10^{49}$ s^{-1} Mpc^{-3})	$\chi^{2,b}_\nu$
1	$-2.04^{+0.33}_{-0.18}$	$-25.8^{+1.1}_{-1.9}$	4.06	1.63	0.5
1'	$-2.03^{+0.54}_{-0.32}$	$-25.7^{+1.1}_{-3.6}$	4.25	1.48	0.6
2	$-1.98^{+0.48}_{-0.21}$	$-25.7^{+1.0}_{-1.8}$	4.53	1.34	0.5
2'	$-1.85^{+0.86}_{-0.40}$	$-25.4^{+0.9}_{-2.2}$	6.53	1.00	0.6

[a] Ionizing emissivity in which we assume that the escape fraction is $f_{\rm esc} = 1$ and the IGM clumping factor is $C = 3$. The cases where the X-ray based bin of Parsa et al. (2017) is excluded for case 1 and 2 are shown in case 1' and 2', respectively.
[b] Reduced chisquare of the QLF fitting.

Mpc^{-3} (Madau et al. , 1999), where C is the IGM clumping factor. Therefore, the contribution of $z \sim 6$ quasars to the ionizing photons is 5.4% in case 1 and 4.4% in case 2, if we assume the fiducial value of $C = 3$ (e.g., Shull et al., 2012). In Figure 2.4, the ionizing photon emissivity at each $\alpha - M^*_{1450}$ plane is indicated with solid lines assuming case 1. The shades show the corresponding photon budget, which indicates that the 2σ confidence range falls at $\sim 1-12$% contribution in either case. The error estimate is based on the two-dimensional confidence range of α and M^*_{1450} (Fig. 2.4). Meanwhile, if the QLF is integrated further down to $M_{1450} = -13$, where the recent studies of $z > 6$ UV luminosity function of galaxies exploiting gravitational lensing have reached (Livermore et al., 2017; Bouwens et al., 2017), the photon budget is still small (9.8% and 7.0% for case 1 and 2, respectively). Furthermore, while we include in the QLF fitting the faint AGN candidate (ID-28476 in Giallongo et al. (2015)) at $M_{1450} = -19.03$, the ionizing emissivity gets smaller if we remove it and estimate the QLF only with spectroscopically-identified quasars. Taking systematic uncertainties due to the choice of the clumping factor ($C \sim 2-5$, Jiang et al. 2016), the escape fraction, and the minimum magnitude of the QLF into account, we place a stringent upper limit of $\lesssim 20$%; thus, our result supports the scenario that quasars are likely the minor contributors of the ionizing background at $z \sim 6$.

As a final remark, more accurate measurements of the QLF faint-end and its redshift evolution can be addressed with the much wider low-luminosity quasar survey with the HSC-SSP.

Chapter 3

Near-Infrared Spectroscopy of Low-Luminosity Quasars at $z = 6 - 7$

Previous studies of the highest redshift quasars suggest that there exist gigantic super massive black holes (SMBHs) with $M_{\rm BH} > 10^9 M_\odot$ even at $z \sim 7$ accreting at the Eddington limit and the SMBHs grow faster than their host galaxies throughout their co-evolutionary growth history. In this chapter, we present the black hole mass measurements of five low-luminosity quasars at $z = 6.1 - 6.7$ identified in our quasar search project exploiting the HSC-SSP. This project has succeeded in discovering more than 60 quasars at $-24 \lesssim M_{1450} \lesssim -22$, which is ~ 2 mag fainter than most of the previous wide-field surveys.

From our deep near-infrared spectroscopy with Gemini/GNIRS and VLT/ X-SHOOTER covering optical to near-infrared range, we detect broad emission lines of MgII λ2798 and CIV λ1549, and the underlying continuum. The two X-SHOOTER targets show peculiar SEDs: one shows a strong and narrow emission lines with FWHM< 2000 km s^{-1} with very weak continuum of $M_{1450} = -23.09$, which reminds one of a type-II quasar-like profile except its blue continuum slope. Another one at $z_{\rm MgII} = 6.7071$ is found to be a red quasar in the transitional phase between starburst and type-I quasar, which is implied from its unusually flat continuum and red observed color of $y - W2 = 2.96$. Its strong double absorption at the blue side of CIV and NV may indicate the presence of episodic nuclear outflow.

Based on the so-called single-epoch method, the measured line profiles suggest a variety in their Eddington ratio of $L_{\rm bol}/L_{\rm Edd} = 0.2 - 8.6$ and the black hole masses with $M_{\rm BH} = 10^{7-9}$ $M_\odot$, while more luminous quasars at the same redshift range prefer the Eddington-limit accretion. The two $M_{\rm BH} \sim 10^9 M_\odot$ black holes with $L_{\rm bol}/L_{\rm Edd} \sim 0.1$ cannot be explained with their current accretion speeds, and are likely the first quasars whose growth is already in their post-active phase. This is in contrast to the most luminous quasars at $z > 6$, which likely experience their most active phase of mass growth from their birth. We compile $z > 6$ quasars whose black hole masses are available and divide them into two luminosity bins at $L_{\rm bol} = 10^{47}$ erg s^{-1}. The Eddington ratio distribution has a twice larger dispersion in the less luminous bin than the luminous bin with $< \log L_{\rm bol}/L_{\rm Edd} >= -0.14 \pm 0.41$. Combined with our recent ALMA observations for two targets aiming at the host galaxy properties, we may witness the build up of the local galaxy-SMBH co-evolution at high redshift.

3.1 Introduction

High-redshift quasars are one of the most important probes of the universe at the reionization epoch. Observational studies of quasars help us to understand formation and early growth history of the super massive black holes (SMBHs), their host galaxies, and the reionization process. The last two decades have seen a great progress in the search for $z \sim 6-7$ quasars, the number of which has reached to more than 200 thanks to large optical and NIR surveys such as SDSS (e.g., Fan et al. 2006c; Jiang et al. 2016), UKIDSS (e.g., Mortlock et al. 2011; Bañados et al. 2017), and Pan-STARRS1 (e.g., Bañados et al. 2016). Mortlock et al. (2011) discovered a gigantic SMBH with $M_{\rm BH} = 2 \times 10^9\ M_\odot$ at $z = 7.085$, which have put strong constraints on its accretion history and its seed mass at birth. Since the quasar luminosity is the product of black hole mass and accretion rate, dedicated mass measurements are needed to disentangle the two quantities. There is a clear trend seen in the current mass measurements for $z > 6$ SMBHs. The observed Eddington ratios peak at $L_{\rm bol}/L_{\rm Edd} \sim 0.1$ at $z < 4$ (Shen et al., 2008; Schulze et al., 2015), Figure 3.1 shows the observed distribution of SDSS DR5 quasars (Schenider et al., 2007) at $z \lesssim 4$. However, most SMBHs at $z > 6$ with $M_{\rm BH} \sim 10^{9-10} M_\odot$ accrete at the rate around the Eddington limit, which indicates that such a fast growth is common at the highest redshift. In the context of the SMBH co-evolution with host galaxies, Venemans et al. (2016) show that extremely luminous $z \sim 7$ quasars are powered by SMBHs growing faster than their host galaxies in comparison with the bulge-to-BH mass ratio in the local universe (the so-called $M_{\rm BH} - \sigma$ relation; Kormendy & Ho 2013). Nevertheless, their star-formation rates are quite high with roughly $> 100\ M_\odot\ {\rm yr}^{-1}$. In addition, it has been suggested that the quasar host galaxies are already metal-rich at $z > 6$ and there is no signifiant metallicity evolution down to the reionization epoch (e.g., Nagao et al., 2006; De Rosa et al., 2014).

However, these current knowledge of the SMBH evolution is likely biased because those arguments are based on the most luminous, namely the most massive and active SMBH populations at this epoch. This is due to the depth limits of the past quasar surveys. Therefore, more general views on the SMBH growth and the co-evolutionary relationship with host galaxies are still unclear. It follows that low-luminosity quasars at $z > 6$ are the keys because they are powered by more typical, less massive or less active SMBHs in the reionization epoch.

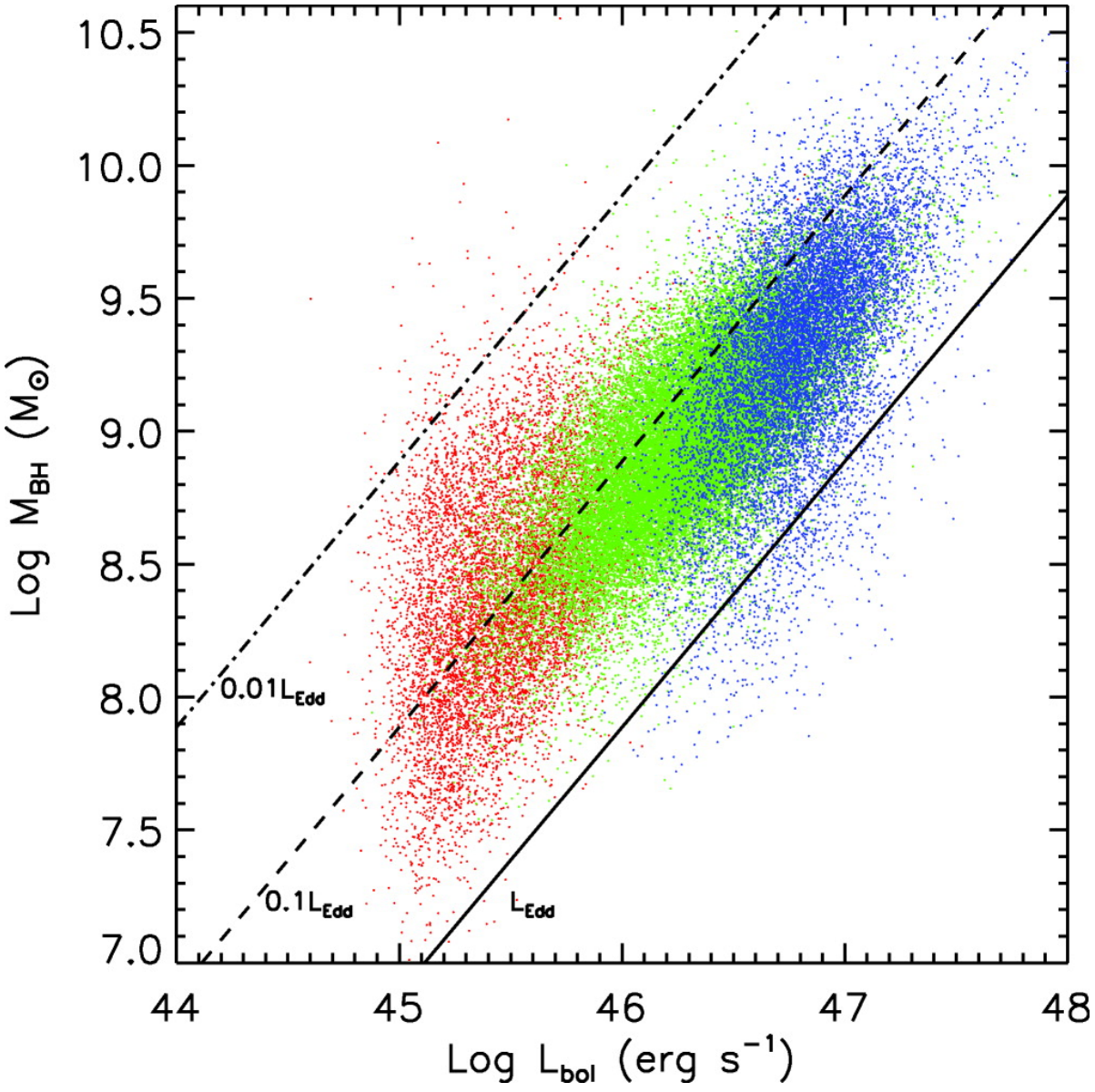

Figure 3.1: The distribution of SDSS DR5 quasars at $z \lesssim 4$ from Shen et al. (2008, Figure 11). Different colors show different mass estimator and therefore different redshift range (red: $z \lesssim 1$, green:$1 \lesssim z \lesssim 2$, blue: $2 \lesssim z \lesssim 4$). The virial mass is estimated based on Hβ, CIV, and MgII emission lines, respectively. The diagonal lines indicate the corresponding Eddington ratio from $L_{\rm bol} = 0.01$ to 1.

3.2 The Subaru High-z Exploration of Low-Luminosity Quasars (SHELLQs)

3.2.1 Our Project

Exploiting the unique optical imaging dataset provided by the HSC-SSP (Section 1.4), we have conducted a ground-breaking survey for $z \sim 6-7$ quasars to construct an unprecedentedly massive sample of low-luminosity quasars. This is an advanced project from the previous Suprime-Cam survey (Chapter 2) and is made possible thanks to the deep imaging of the 8m telescope with the HSC field-of-view approximately seven times wider than that of the previous Suprime-Cam. We name this project as *the Subaru High-z Exploration of Low-Luminosity Quasars*, or *SHELLQs* in short. From the first-year data of the HSC-SSP covering effectively 430 deg^2, this project has succeeded in discovering more than 60 quasars at $5.8 \leq z \leq 6.9$ among which 33 have been published (Matsuoka et al., 2016, 2018). This number accounts for $\sim 20\%$ of the all $z > 6$ quasars currently known. The discovery spectra of the new quasars taken by Subaru/FOCAS and GTC/OSIRIS are shown in Figure 3.2, Figure 3.3, Figure 3.4, and Figure 3.5.

To briefly mention the candidate selection, we utilize the *grizy* broad-band photometry of the HSC-Wide survey. As described in Section 1.3 and Section 2.2, the optical colors of $z \sim 6$ and $z \sim 7$ quasars are characterized by red $i-z$ and $z-y$ colors, respectively. We also use those color cuts in the initial candidate selection: $i-z > 1.5$ and $z-y > 0.8$ at each redshift range as well as various photometry flags and point source selection. What is unique is that an Bayesian-based probabilistic approach is applied for the initially extracted candidates. In its framework, good quasar candidates are those who attain high quasar probabilities; in other words, those who are more close to typical quasars in multi-color space. This method is first proposed in Mortlock et al. (2012) in which the surface densities of quasars and brown dwarfs are implemented as weight factors, or prior. This method is quite helpful in reducing the number of candidates because surface densities of contaminants (i.e. brown dwarfs) are much higher than those of $z > 6$ quasars. Note that similar approaches have recently been proposed in, for example, Reed et al. (2017) and Yang et al. (2017).

Figure 3.6 clearly shows the uniqueness of our SHELLQs samples by the distribution of red-

shift and absolute magnitude of the SHELLQs quasars. It is evident in the figure that the quasars identified with our surveys, including the Suprime-Cam quasars described in Chapter 2, are much fainter than most of the others by ~ 2 mag.

3.2.2 Narrow Lyα quasars

Here, a notable population in the SHELLQs quasars is briefly described. Among the 33 SHELLQs quasars, there is a variety in their observed optical SEDs such as the sharpness of the strong absorption blueward of Lyα due to neutral IGM and strong and broad absorption at NV λ1240. The most peculiar population is the 12 quasars with narrow Lyα emission lines. Their characteristics can be summarized as follows: (i) they are point sources in the HSC imaging (FWHM$\sim$ 0".6), (ii) their continuum emission, albeit noisy, do not show clear interstellar absorption such as SiII λ1260, λ1304, and CII λ1335, which are visible in our SHELLQs galaxy spectra, (iii) they have narrow Lyα with $\mathrm{FWHM_{Ly\alpha}} \sim 300$ km s^{-1}, high Lyα luminosity with $L_{\mathrm{Ly\alpha}} \sim 10^{43-44}$ erg s^{-1} and high $\mathrm{EW_{rest}}$ up to 370Å(HSC J1423-0018, Figure 3.4), and finally, (iv) there is a small absorption blueward of NV λ1240 ($\mathrm{FWHM_{Nv,abs}} \gtrsim 1000$ km s^{-1}) in their composite spectrum (Figure 10 of Matsuoka et al. 2018), which is indicative of broad absorption line quasars (BALs). Note that the line widths are similar to those of bright Lyman α emitters (Shibuya et al., 2017), rather than typical type-I quasars ($\mathrm{FWHM_{Ly\alpha}} > 1000$ km s^{-1}). Remarkably, one of the two quasars found in our Suprime-Cam surveys, ELAIS1091000446 at $z = 6.041$ also shows the same spectral properties (Kashikawa et al. 2015 and Section 2.2). Since this population has been only found in low-luminosity quasar searches and no apparent counterparts have been identified at low redshifts, this population could be a new kind of high redshift objects common in the optically faint range where the number densities of quasars and Lyman break galaxies are comparable (Figure 2.3). The magnitude distribution of the SHELLQs sources and the composite spectrum of 12 narrow Lyα quasars are given in Figure 3.7. While we have planned their deep follow-up observations with Keck/MOSFIRE and VLT/X-SHOOTER to investigate their classification, we do not discuss their nature in details in this thesis. We speculate that they are either composites of type-I quasars and Lyα emitters, type-II quasars, or galaxies with very young stellar populations (i.e., Population II or III). Specifically, HSC J1423-0018 shows a very strong and narrow Lyα with $L_{\mathrm{Ly\alpha}} = 10^{44.3\pm0.01}$ erg s^{-1}, which is highest as a $z > 6$ LAE, and is about one order of excess

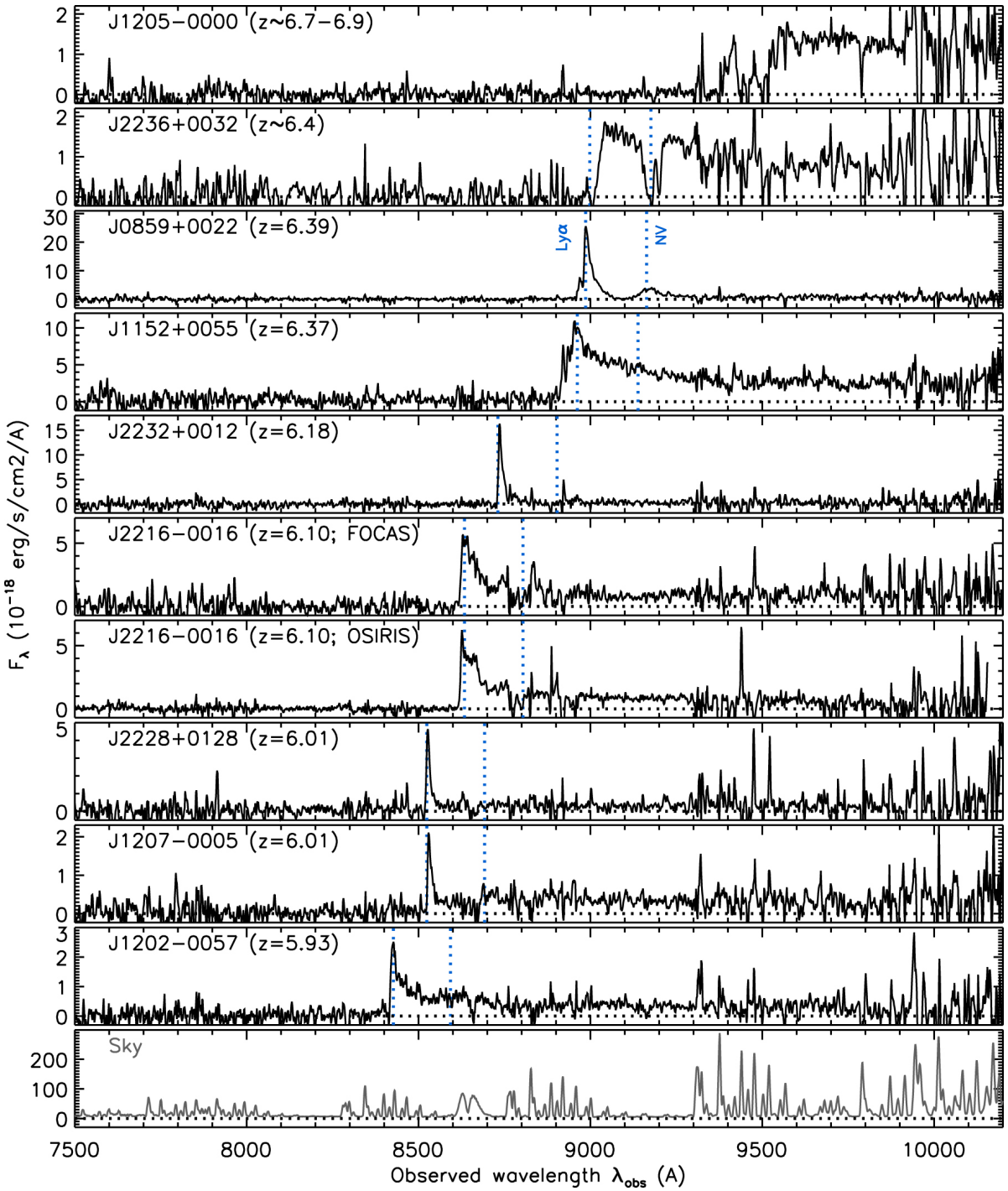

Figure 3.2: Discovery spectra of 9 SHELLQs quasars from our first paper, quoted from Matsuoka et al. (2016) with a permission of the authors. The position of Lyα and N V λ1240 are indicated as dotted lines. Note that HSC J2216-0016 was observed both in Subaru/FOCAS and GTC/OSIRIS.

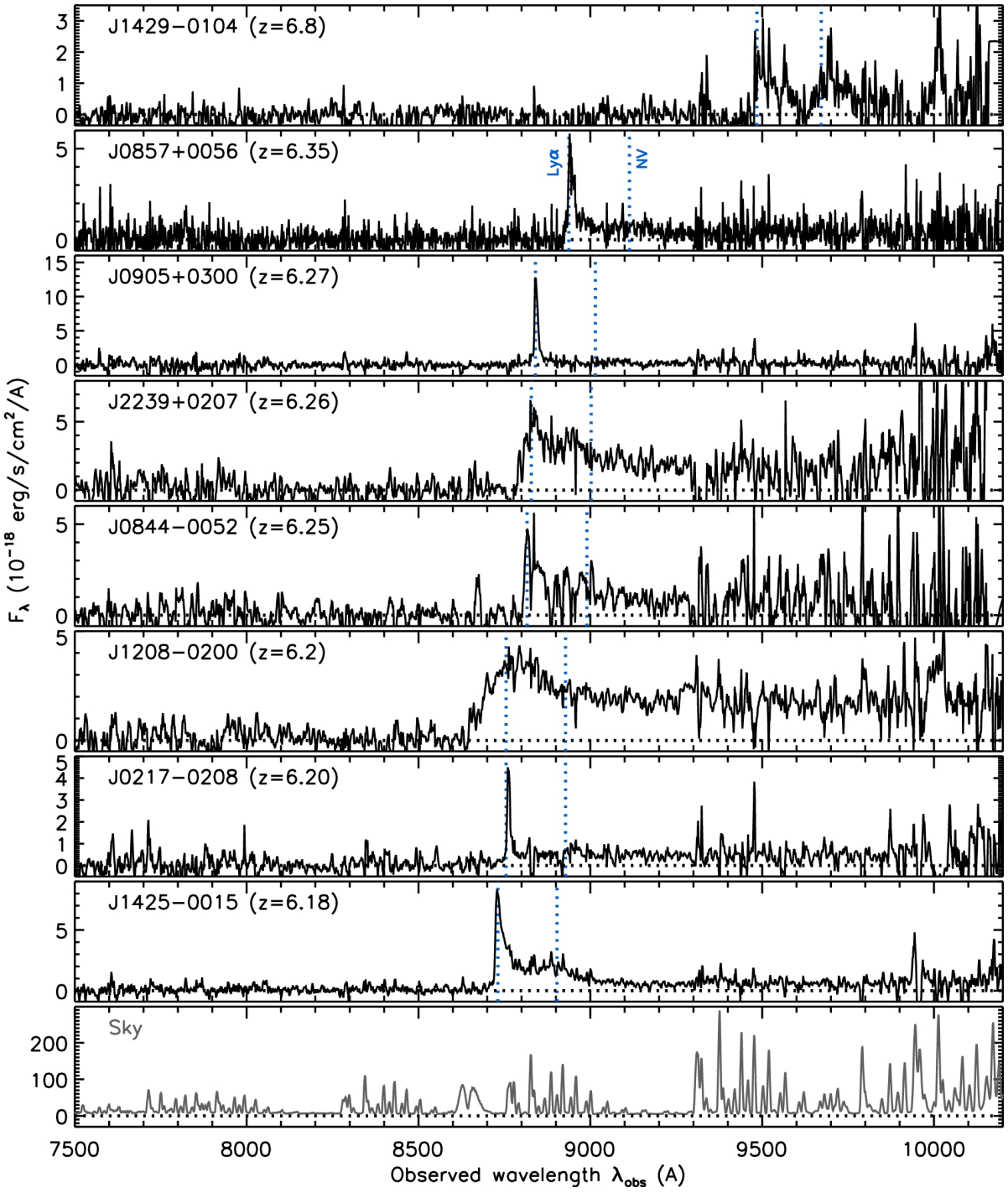

Figure 3.3: Discovery spectra of 24 SHELLQs quasars from our first paper, quoted from Matsuoka et al. (2018) with a permission from the authors.

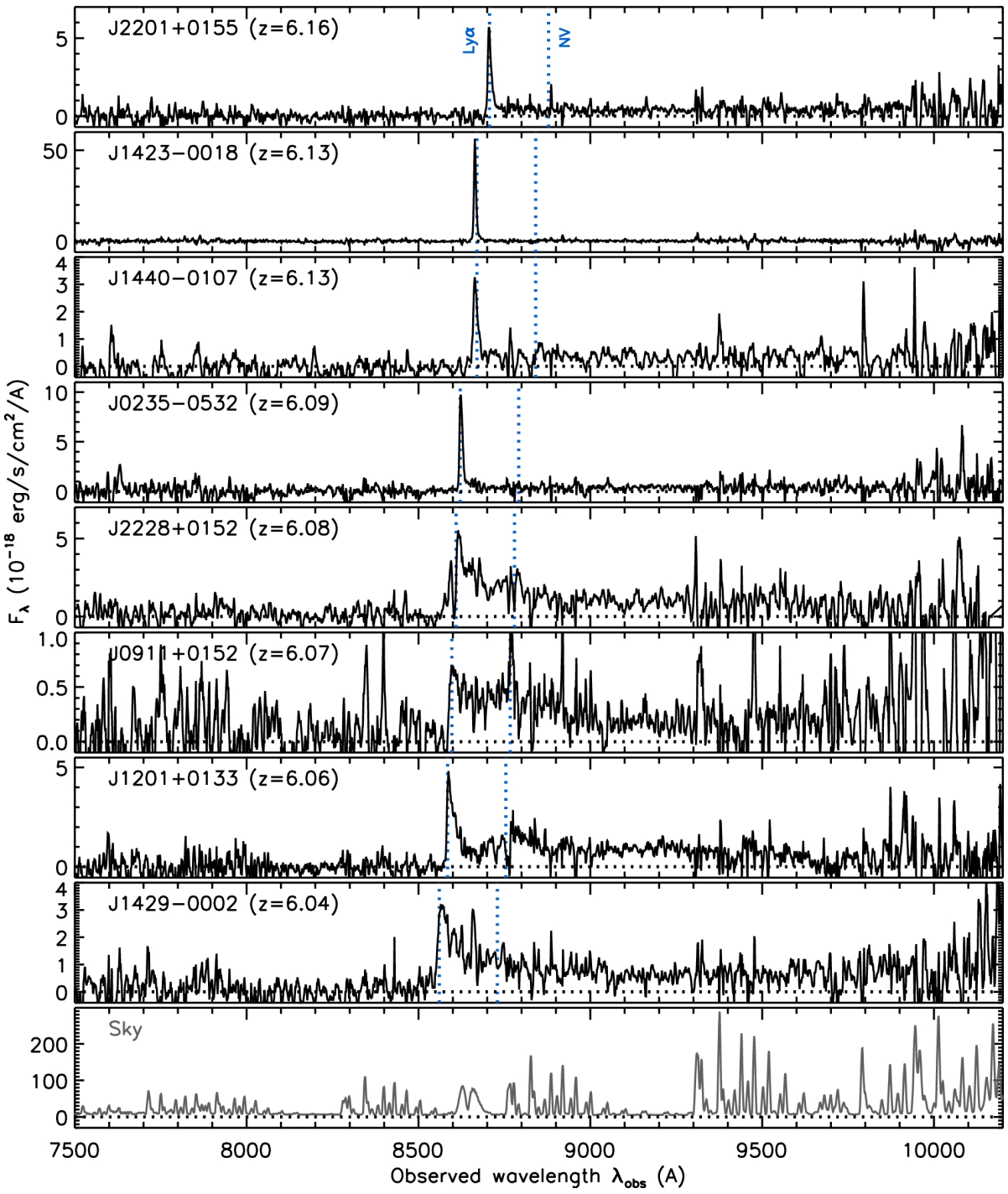

Figure 3.4: Contd.

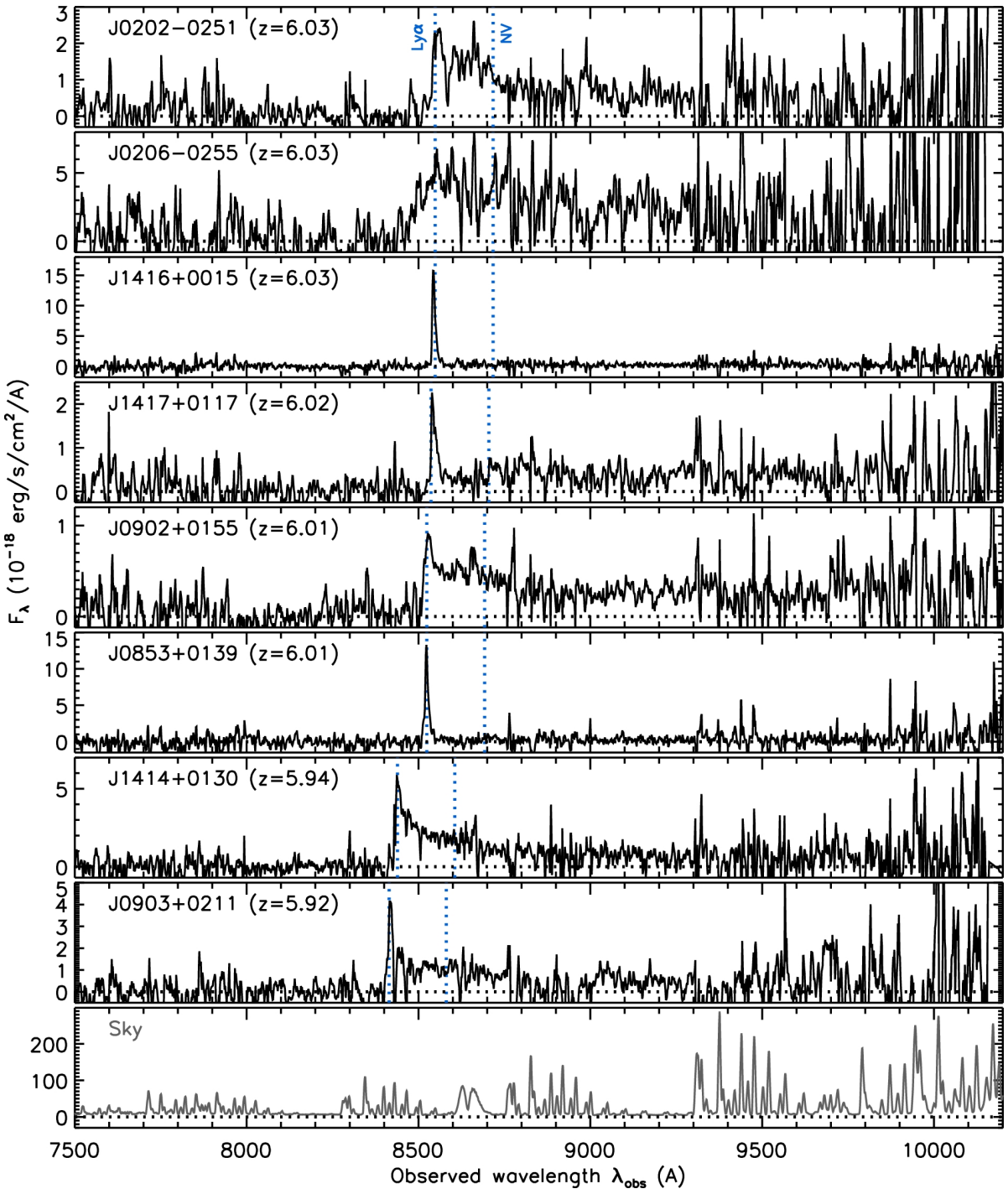

Figure 3.5: Contd.

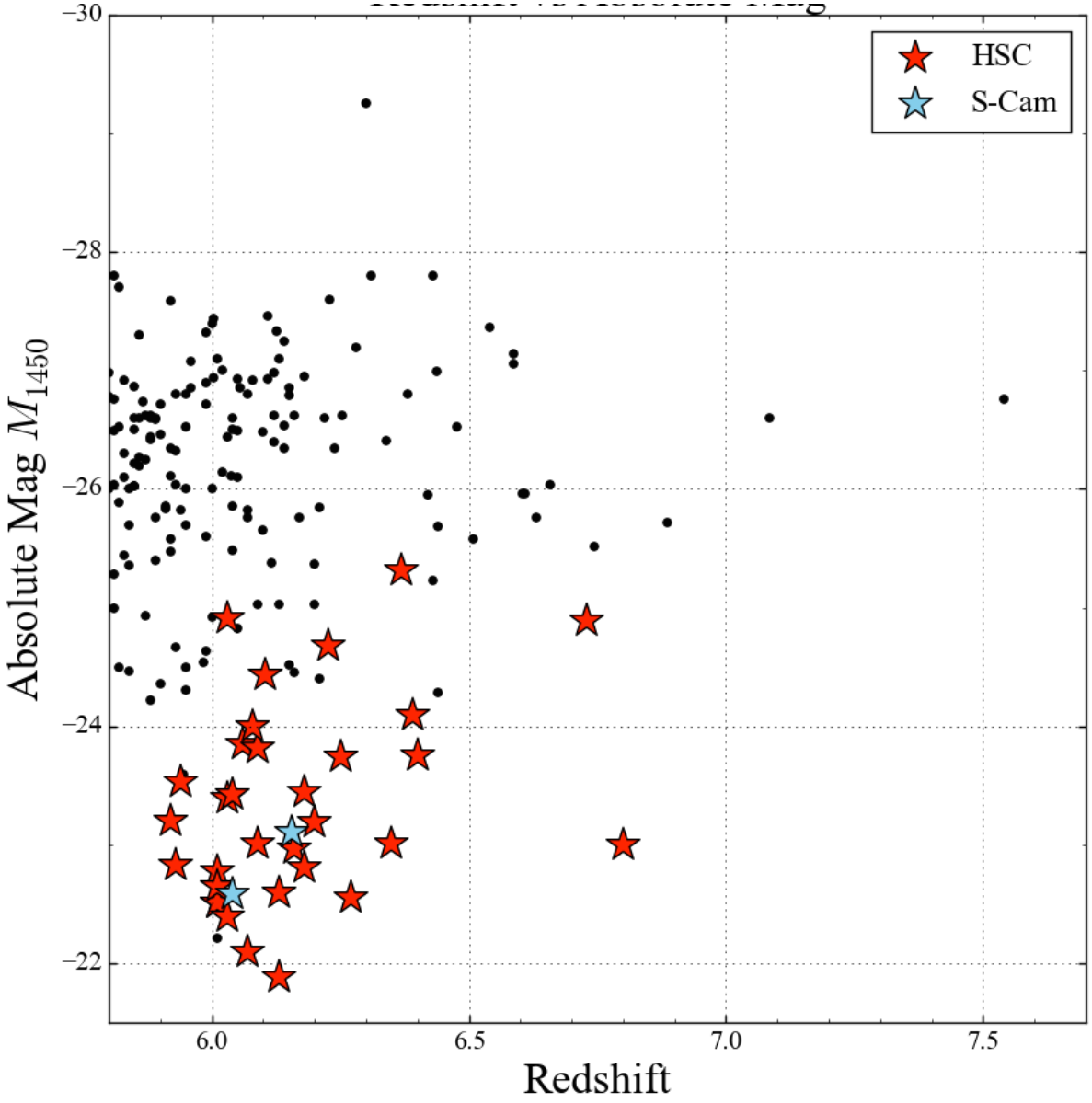

Figure 3.6: The distribution of redshift and absolute magnitude, M_{1450} [mag] of the published quasars at $z > 5.8$ as of January 2018. Red and blue stars show the quasars discovered in the HSC (Matsuoka et al., 2016, 2018) and S-Cam surveys (Kashikawa et al., 2015). The two quasars at $z > 7.0$ are from the UKIDSS survey (Mortlock et al., 2011; Bañados et al., 2017). For the five HSC quasars discussed in this chapter, the quantities are updated with the near-infrared measurements.

from the HSC LAEs (Shibuya et al., 2017).

3.3 Sample Selection

With the unique sample of $z > 6$ low-luminosity quasars, we conducted spectroscopic follow-up observations in NIR range to measure their black hole mass based on the single-epoch method (Section 3.7 for details). We selected our targets from the 33 SHELLQs quasars as follows. First, since we use the MgII λ2798 emission lines and the underlying continuum as the BH mass estimators (e.g., Vestergaard & Osmer , 2009), we limit the (optical) redshift range as $z_{\rm opt} > 6.04$ to avoid severe atmospheric absorption at the MgII line in K-band ($\lambda_{\rm obs} > 1.97$ μm). Another thing we should consider is that since our low-luminosity quasars are close to or beyond the depth limit of ground-based 8m-telescopes for NIR spectroscopy, we apply a magnitude cut of $M_{1450} < -23.8$ to observe within realistic integration times (< 10 hours).

As a result, seven quasars at $6.09 \leq z_{\rm opt} \leq 6.8$ are left. Their absolute 1450Å magnitudes are in the range of $-25.31 \leq M_{1450} \leq -23.82$. This is roughly an order of magnitude fainter than the SDSS quasars whose BH masses have been measured (Kurk et al., 2007; Jiang et al., 2007; De Rosa et al., 2011). Also, our samples are as faint as or fainter than those in the mass measurements of the CFHQS quasars (Willott et al., 2010a). The updated measurements of the absolute magnitudes are described in Section 3.5.4.

3.4 Observation and Data Reduction

We obtained NIR spectra of five targets extracted in the previous section. HSC J2239+0207 at $z_{\rm opt} = 6.26$ ($M_{1450} = -24.69$) was observed in Gemini Nourth GNIRS in the S16B fast turnaround program (ID: GN-2016B-FT-2, PI: M.Onoue). HSC J1208-0200 at $z_{\rm opt} = 6.2$ ($M_{1450} = -24.73$) and HSC J2216-0016 at $z_{\rm opt} = 6.09$ ($M_{1450} = -23.82$) were also observed in Gemini North GNIRS as a S17A Subaru-Gemini exchange program (ID: S17A0039N, PI: M.Onoue). There is another target in S17A, HSC J2228+0152 at $z_{\rm opt} = 6.09$ ($M_{1450} = -24.00$), but the observation was not executed in our queue mode observations, unfortunately. The other three, namely HSC J1205-0000 ($z_{\rm opt} = 6.8$, $M_{1450} = -24.56$), HSC J0859+0022 ($z_{\rm opt} = 6.39$, $M_{1450} = -24.09$), and HSC J1152+0055 ($z_{\rm opt} =$

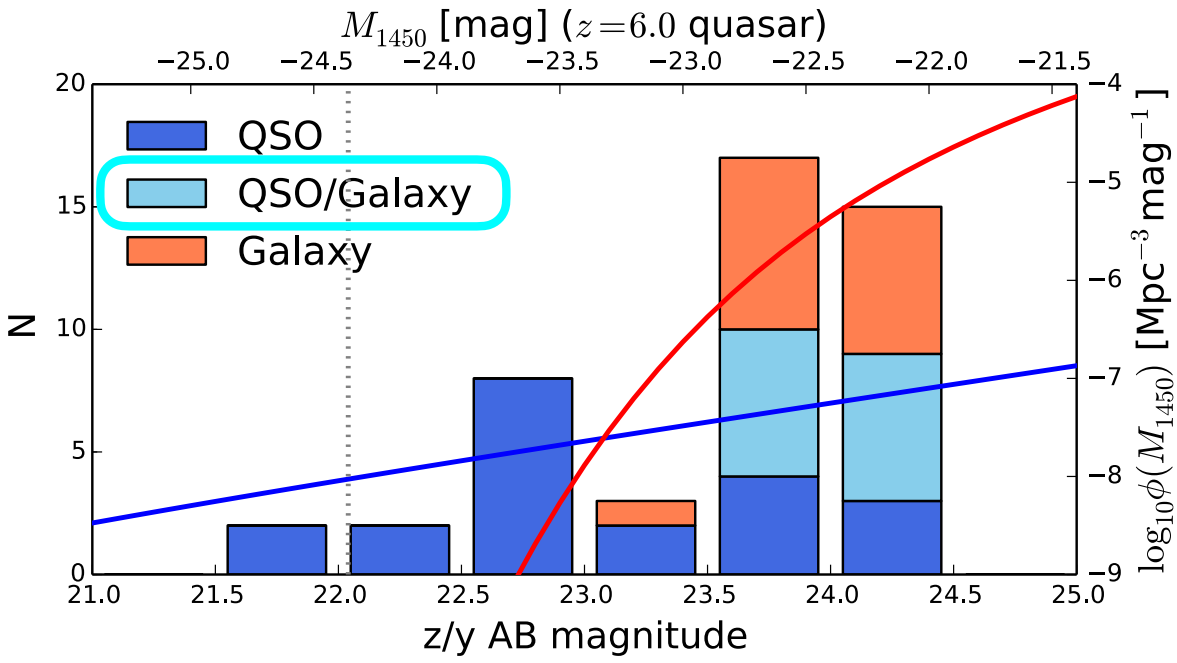

Figure 3.7: The histogram of the $z > 6$ objects currently identified through the SHELLQs project (z_{AB} for $z \sim 6$ and y_{AB} for $z \sim 7$). The target population in this proposal is shown as "QSO/Galaxy". The overlaid lines are the $z \sim 6$ QLF (blue) from Kashikawa et al. (2015) and the luminosity function of Lyman break galaxies (red) from Bouwens et al. (2015)

6.37, $M_{1450} = -25.31$) are for our Period 98 VLT/X-SHOOTER runs (ID: 098.A-0527, PI: M.Onoue), while J1152+0055 observation was not executed before this thesis and thus this quasar is not discussed. Therefore, the mass measurements for five targets; J2239+0207, J1208-0200, J2216-0016, J0859+0022 and J1205-0000 are presented in the following sections. Table 3.1 summarizes the targets and observations.

3.4.1 Gemini/GNIRS

The GNIRS observation were carried out in cross-dispersed echelle mode to cover the observed wavelength coverage of $\lambda_{\rm obs} \sim 0.9-2.5\mu$m, corresponding to the rest-frame wavelength coverage of $\lambda_{\rm obs} = 0.12-0.35$ μm. We used 31.7 l/mm grating and the short camera (0.15 arcsec per pixel). The slit width was chose to keep balance between spectral resolution and slit loss. More specifically, 0".675-slit was used for J1208-0200 and J2216-016, which results in the spectral resolution of $R \sim 760$. A slightly wider 1".0-slit was used for J2239+0207 because the reference star during the blind offset is relatively far (~ 40 arcsec) from the target and we needed to compromise on the acquisition accuracy. The spectral resolution in this case is $R \sim 510$, which is still sufficient to resolve the broad emission lines of MgII and CIV with FWHM> 1000 km s^{-1}. The single exposure time was set to 300 sec and the standard ABBA offset of 3 arcseconds in the spatial direction was applied for good subtraction of variable sky backgrounds. Spectra of nearby A-type stars are taken before and after the target observation at the similar altitudes, which are used for correcting telluric atmospheric absorption and calibrating relative sensitivity.

The GNIRS data were reduced with a dedicated Gemini IRAF pipeline Version 1.13. All the procedures are applied for dataset taken in each observation date, while in some cases, the data taken in one day needs to be separated due to offset of the target positions in the 2D spectra during the observation. Following a standard procedure, we first flat-field the 2D spectra and subtract sky background using each pair taken in the A and B node positions. After that, 2D spectra are stacked to maximize the signal-to-noise ratio. Distortion correction is done based on the GNIRS pinhole spectra taken in each day of the observations. After the 2D spectra of each order are straightened, the pixel-to-wavelength calibration is done with arc spectra. In the 1D spectrum extraction, the stacked 2D spectra are Gaussian weighted in the spatial direction. The shape of the Gaussian is determined by stacking the spectra into the spectral direction and

fitting the spatial profiles of the targets with Gaussian profiles. This procedure is applied because the continuum of our targets are faint and thus maximizing the spectral quality is needed. Standard A-type star spectra are used for relative flux calibration and correcting atmospheric absorption. SED templates of A-type stars taken from the 1993 Kurucz stellar atmosphere ATLAS[1] for this purpose. The absolute flux calibration is done by scaling the derived spectra to the observed broad-band photometry. The HSC-y magnitudes of the targets in the DR S16A are used for J2239+0207 and J1208-0200. Due to poor signal-to-noise ratio at $\lambda \sim 1.0\mu$m, J2216-0016 spectrum is scaled to the expected VIKING J-band magnitude measured by extrapolating the HSC-y magnitude assuming a power-law index obtained in the continuum fitting, which is described in Section 3.5.1.

The final 1D spectra are obtained by connecting each order. We do not consider the offset of the flux scale between each order due to poor S/N ratio. The order 8 (Z-band) is ignored because of low signal-to-noise ratio. Alternatively, the optical discovery spectra of each target taken in Subaru/FOCAS and GTC/OSIRIS are connected to the Gemini spectra. Finally, the spectra are smoothed with a Gaussian kernel with $\sigma = 2$ pixels (FWHM ~ 400 km s^{-1}), which does not affect our spectral analysis because the main interests are broad emission lines with FWHM > 1000 km s^{-1}.

3.4.2 VLT/X-SHOOTER

The VLT/X-SHOOTER is an Echelette spectrograph on the 8.2m VLT telescope (UT2), which consists of three independent detector arms covering different wavelength range: UVB ($\lambda_{\rm obs} = 3000-5600$Å), VIS ($\lambda_{\rm obs} = 5500-10200$Å), and NIR ($\lambda_{\rm obs} = 10200-24800$Å) arms. We use VIS and NIR arms data and ignore the UVB arm because $z > 6$ quasars have no signals due to heavy IGM absorption. We use $0".9 \times 11"$-slit in VIS and NIR arms with the pixel scales of $0.15-0.17"$ pix^{-1} and $0.18-0.21"$ pix^{-1} respectively, varying in the curved orders. High-gain 2×2-binning (spectral and special) slow-readout mode is applied in VIS arm. With this configuration, moderate spectral resolution is achieved: $R \sim 7410$ for VIS arm and $R \sim 5410$ for NIR arm. Blind offset is used for target acquisition with reference bright stars nearby. The integration is divided into pairs of ~ 200 seconds single exposures to subtract time-varying sky emission with the stan-

[1] http://www.stsci.edu/hst/observatory/crds/k93models.html

dard ABBA offset procedure. J0859+0022 was observed in 10 Observation Blocks (OBs)[2] divided into three runs, which corresponds to the total integration times of 6.5 hours in VIS arm and 7.2 hours in NIR arm. J1205-0000 has been also observed for 6.5 and 7.2 hours in each arm on [3]. As described in Section 3.6.5, this target is included because of its unexpectedly-bright near-infrared continuum. The two VLT targets were observed at the airmass of $\sim 1.1-1.3$ with the seeing size of $\sim 0".8$.

The obtained raw data are processed with the dedicated X-SHOOTER pipeline version 2.9.3 except 1D spectrum extraction, which is based on the same procedure applied in the Gemini/GNIRS spectra. Spectroscopic standard stars were observed for relative flux calibration in both arms. Absolute flux calibration is based on its HSC-z band magnitude for J0859 and VIKING-Ks magnitude for J1205-0000. Atmospheric absorption is corrected with a sky transmission model obtained from *SkyCalc* version 2.0.1, assuming the seasonal average at the observation dates and airmass. After stacking stacked 1D spectra of each observing date, the final spectra are obtained after smoothing with a gaussian kernel of $\sigma = 15$ pixels (FWHM ~ 300 km s^{-1} at Ks).

3.5 Optical-to-NIR Spectra

Figure 3.8 shows the final optical-to-NIR spectra of the three Gemini/GNIRS targets. Figure 3.9 shows the spectra of the two VLT/X-SHOOTER targets. Note that the Gemini spectra are connected with the optical spectra (Subaru/FOCAS: J1208, J2216; GTC/OSIRIS: J2239) at $\lambda_{\rm obs} \sim$ 9000Å, and the VIS and NIR arm spectra are combined at $\lambda_{\rm obs} \sim$ 10200Å for the X-SHOOTER spectra.

3.5.1 Spectral Model

The derived spectra are modeled by a combination of following components. The Balmer continuum is not considered due to the relatively low signal-to-noise ratio, which is used in model-

[2] OB is the unit of the VLT observation, consisting of ~ 1 hour observation including target acquisition, target observation, and all the other procedures necessary for the science observation

[3] only 1 out of 10 OBs was executed at the time of the thesis defense, but the spectrum and the analysis is updated in this final version because all the OBs were executed.

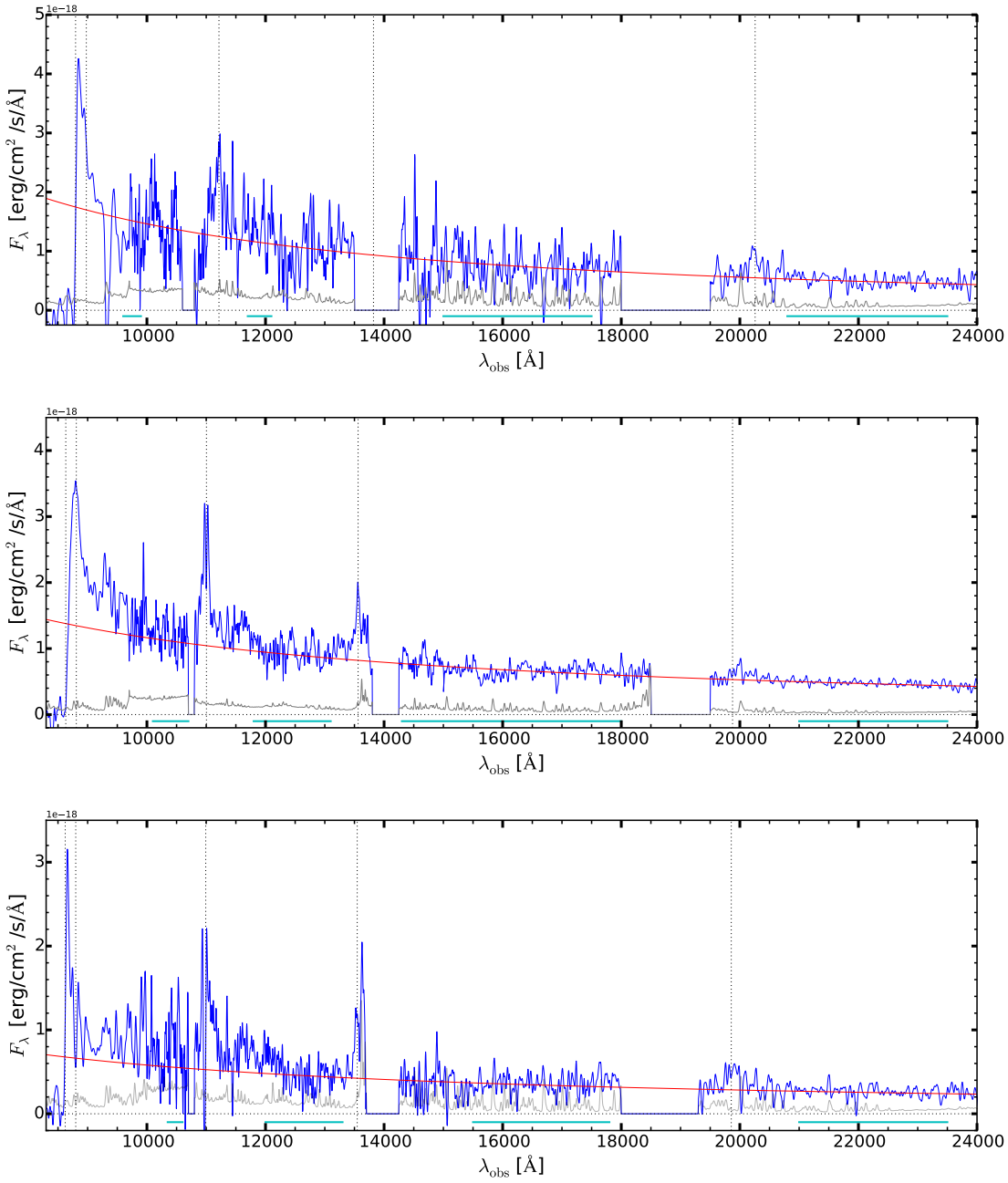

Figure 3.8: Optical-to-NIR spectra of the three Gemini/GNIRS targets (top: HSC J2239+0207, middle: HSC J1208-0200, bottom: HSC J2216-0016). The error spectra are shown as grey. Some regions affected by severe atmospheric absorption are masked. The GNIRS spectra are connected with optical discovery spectra taken by Subaru/FOCAS and GTC/OSIRIS at $\lambda \sim 0.9\mu$m. The best-fit power-laws are shown as red. The regions used for continuum fitting are indicated as cyan. The vertical dotted lines show the expected positions of strong emission line (Lyα, NV, CIV, CIII], and MgII from left to right) based on the updated redshifts (Table 3.3).

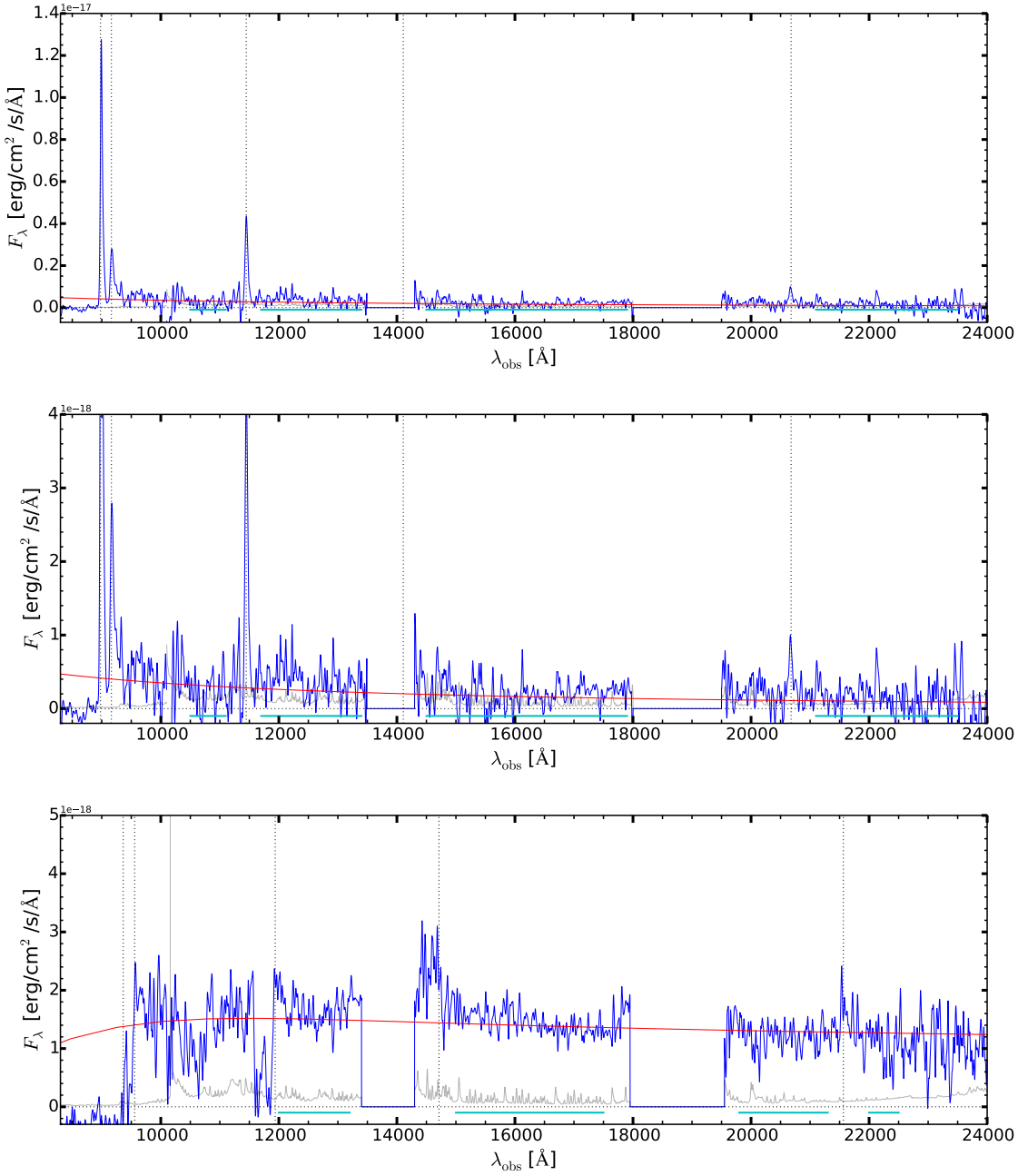

Figure 3.9: Optical-to-NIR spectra of the two VLT/X-SHOOTER targets (top and middle: HSC J0859+0022, bottom: HSC J1205-0000). The middle panel is for showing the weak continuum of J0859+0022. The VIS arm spectra are 7-pixel binned after smoothing for display purpose. The spectrum of J1205-0000, a red quasar, is fitted with a power-law model of $\alpha_\lambda = -1.5$ with the internal extinction of $E(B-V) = 0.27$ assuming the Calzetti law (Calzetti et al., 2000), while the FeII component is not considered.

ing high-quality quasar spectra (De Rosa et al., 2014).

Continuum

First, the primary component of the rest-frame UV continuum spectrum of a quasar is a power-law, which is the sum of black body radiation from the black hole accretion disk. Here, we model the observed continuum of the target quasars with a single power-law:

$$F_{\lambda,\mathrm{cont}} = F_0 \, \lambda^{\alpha_\lambda} \tag{3.1}$$

where F_0 is the scale factor and α_λ is the power-law index. The slope of the quasar continuum is known to have little redshift evolution with the most commonly used value of $\alpha_\lambda \sim -1.5$ at all redshift (Vanden Berk et al., 2001). To remove the contribution from strong emission lines and not to be strongly affected by atmospheric absorption, one usually needs to select several continuum fitting windows. As described in Section 3.5.2, the fitting is an iterative process to model the power-law and FeII forests simultaneously, which allows one to use wide fitting windows over the spectral coverage.

FeII Pseudo Continuum

The secondary component is the forests of FeII emission lines. Because iron has thousands of weak emission lines in the rest-frame UV range and they blend with each other, those lines are observed as pseudo-continuum, which complicates the measurements of true continuum levels. In this work, the empirical template of the FeII emission lines from Vestergaard & Wilkes (2001) is used. This template is derived from a high-resolution spectrum of I Zw I, a nearby Seyfert 1 galaxy at $z = 0.061$ with relatively narrow and strong iron emission lines. For the spectral modeling of the target quasars in this study, the narrow iron emission lines are smoothed with a Gaussian kernel in a logarithmic wavelength space with

$$\sigma_{\mathrm{conv}} = \sqrt{\mathrm{FWHM}^2_{\mathrm{QSO}} - \mathrm{FWHM}^2_{\mathrm{I\,Zw\,I}}} / 2\sqrt{2\ln 2} \tag{3.2}$$

where $\mathrm{FWHM_{I\ Zw\ I}} = 900$ km s^{-1} is the original line width of the I Zw I template. Since the line width of the quasars varies in the range of $1000-15000$ km s^{-1}, three models are generated with $\mathrm{FWHM_{QSO}} = 1000, 5000, 10000$ km s^{-1}. Vestergaard & Wilkes (2001) recommend to prepare a number of templates in steps of 250 km s^{-1}, however we only use the three considering the relatively low signal-to-noise ratio of the spectra and it is actually found that the template of $\mathrm{FWHM_{QSO}} = 5000$ km s^{-1} always gives the best-fit perhaps due to the large step and spectrum resolution. Therefore, the FeII models shown in the following sections are from this one template.

Emission Lines

Emission lines considered in this work are MgII λ2798, CIII] λ1909, and CIV λ1549. Those strong lines are fitted with a single or double Gaussian profile after subtracting the best-fit models of power-law continuum and FeII pseudo-continuum. Single Gaussian is mostly used, but in some cases double Gaussian is used if the observed lines have broad line skirts or asymmetric profiles which cannot be well fitted with a single Gaussian. In the case of double Gaussian fitting, the central wavelengths of the two components are fixed at the same positions except the case of the CIV emission line of J2216-0016 (Section 3.6.3).

3.5.2 Spectral Fitting

The spectral fitting, which is mostly the same as the one applied in the previous studies (Jiang et al., 2007; De Rosa et al., 2014), is done as follows [4]. It is difficult to fit the two continuum components simultaneously because the both components cover the similar wavelength range. An iterative fitting procedure helps to disentangle the two components. First, a power-law is fitted to selected regions in the spectra. We avoid the order gaps and regions where emission and absorption lines are visible in the spectra; thus the fitted regions vary from target to target. In the initial fitting, only the most clean range is selected. After subtracting the estimated power-law model, the iron templates are fitted to the residuals. The fitting region for the FeII includes the both sides of the MgII and some clean parts at shorter wavelength range. After determining the scale of the iron templates, the best-fit FeII models are subtracted from the original (not

[4] This method is fully described in Section 4.2 of Vestergaard & Wilkes (2001).

power-law subtracted) spectra, for which the power-law is fitted again with much larger fitting window. In this stage most of the continuum ranges are included. Then, the iron template fitting is tried again after subtracting the newly determined power-law models. This iterative fitting for quasar continuum is repeated until convergence of < 1% is achieved. The measured continuum slope index for each target is summarized in Table 3.2 with the range of $-1.60 \leq \alpha_\lambda \leq -1.04$ except J1205-0000 (Section 3.6.5). Since this range is mostly consistent with a luminous $z \sim 6$ quasar measurement in Fan et al. (2001c, $\alpha_\lambda = -1.21 \pm 0.34$), host galaxy contribution to the quasar continuum is negligible. The best-fit power-law and FeII models are shown in Figure 3.8 and Figure 3.9 for Gemini and VLT targets, respectively. It is noted that only the near-infrared spectra are used to determine the continuum models. However, as is evident in Figure 3.8 and 3.9, the best-fit power-law models well trace the optical parts, too.

3.5.3 Redshift

Accurate redshift determination is essential for characterizing various quantities such as absolute magnitude and velocity offset of emission lines. However, it is difficult to estimate the redshift because several emission lines are sometime affected by outflow motions of the accretion disks. The most reliable redshift estimator is the atomic or molecular emission lines such as CO and [CII] 158μm observed in the (sub-)mm range at $z \sim 6$. These lines are known as the useful probes of the star-formation activity of galaxies since they trace the cool interstellar medium from which stars are made. If these lines are not available, the secondary probes of the quasar redshift is the broad or narrow quasar emission lines. For high-redshift quasars, a low ionization line of MgII λ2798 is frequently used. Among several rest-frame UV emission lines detected in the target spectra, the systemic redshift is determined from the best-fit Gaussian models for MgII and CIII] lines. Moreover, [CII] redshift is used if available.

3.5.4 Absolute Magnitude at 1450Å

The absolute magnitude at 1450Å (M_{1450}) is usually used to characterize the intrinsic brightness of quasars (Fan et al., 2001a). Although M_{1450} was measured in the discovery papers (Matsuoka et al., 2016, 2018), we update the quantity because we cover much wider wavelength range, in-

Table 3.1: Gemini and VLT Observations

ID	Redshift[a]	y_{AB}^{b} (mag)	M_{1450} (mag)	Date (UT)	Instrument	$t_{\rm exp}^{c}$ (hour)
HSC J2239+0207	6.26	22.33	−24.69	Aug. 7, 8, 10, & Sep. 27, 2016	Gemini/GNIRS	2.7
HSC J1208-0200	6.2	22.05	−24.73	Feb. 17, 18, 19, 2017	Gemini/GNIRS	3.7
HSC J2216-0016	6.09	22.94	−23.82	Jun. 25, 26, 28, & Jul. 3, 5, 2017	Gemini/GNIRS	9.0
HSC J0859+0022	6.39	23.23	−24.09	Dec. 29, 2016, & Mar. 23,24,30,31 & Dec. 21, 2017	VLT/X-SHOOTER	7.2 (NIR) 6.5 (VIS)
HSC J1205-0000[d]	6.7 − 6.9	22.61	−24.6	Mar. 31, 2017 & Feb. 15,16,21, 2018	VLT/X-SHOOTER	7.2 (NIR) 6.5 (VIS)

[a] Redshift determined with the optical spectra quoted from Matsuoka et al. (2016, 2018).
[b] PSF magnitudes from the HSC-SSP S16A internal catalog.
[c] Total integration times. Those of NIR and VIS arms are separately given for the X-SHOOTER targets.

Table 3.2: Continuum Parameters

	J2239+0207	J1208-0200	J2216-0016	J0859+0022	J1205-0000
α_λ	-1.39 ± 0.03	-1.15 ± 0.01	-1.04 ± 0.04	-1.60 ± 0.04	-1.5
M_{1450}	-24.68 ± 0.33	-24.32 ± 0.14	-23.57 ± 0.37	-23.09 ± 0.43	-27.82 ± 0.04
$M_{1450,\rm M18}$	-24.69 ± 0.04	-24.73 ± 0.02	-23.82 ± 0.04	-24.09 ± 0.07	-24.56 ± 0.04

Notes: The power-law index and absolute magnitude at rest-frame 1450Å derived from the best-fit continuum models. For J1205-0000, the intrinsic continuum slope is fixed at $\alpha_\lambda = -1.5$ and the absolute magnitude is estimated by fitting the scale of its curved continuum with the power-law component including internal reddening of $E(B-V) = 0.27$, assuming the Calzetti law (Calzetti et al., 2000). The absolute magnitude determined in the optical spectra (Matsuoka et al., 2018) are also shown as $M_{1450,\rm M18}$ for reference.

cluding the rest-frame 1450Å, which aids for more reliable estimate of the continuum level. We use the best-fit power-law model of each target to estimate the continuum level at the rest-frame 1450Å and convert it to the absolute magnitude based on the derived redshift and the assumed cosmology. As shown in Table 3.2, we find that the new measurements are roughly consistent with the previous optical measurements assuming $\alpha_\lambda = -1.5$ except two cases (J0859+0022 and J1205-0000) whose continuum is unexpectedly faint or intrinsically bright. Section 3.6.4 and Section 3.6.5 discuss the observed near-infrared SEDs of the individual quasars.

3.6 Fitting Results

In this section, the results of the spectral measurements are described. In addition to the whole shapes of the spectra given in Figure 3.8 and Figure 3.9, Figure 3.11 shows the rest-frame spectra around MgII with the best-fit spectral models of continuum, FeII, and Gaussians. Figure 3.12 shows the rest-frame spectra around CIV and CIII]. The derived emission line properties are shown in Table 3.3.

3.6.1 J2239+0207

J2239+0207 is our first NIR follow-up target at $z_{\rm opt} = 6.26$ observed in Gemini/GNIRS for 2.7 hours. Its power-law continuum is detected over the all orders with several broad emission lines, especially the broad MgII emission line at $\lambda_{\rm obs} \sim 2.03\mu$m. The continuum slope of $\alpha_\lambda = -1.39 \pm 0.03$ is typical for a type-I quasar. Its absolute magnitude of $M_{1450} = -24.68 \pm 0.33$ is consistent with the value obtained from the optical measurements (Matsuoka et al., 2018). The single Gaussian fit results in $z_{\rm MgII} = 6.241 \pm 0.004$, which is slightly smaller than the optical redshift reported in Matsuoka et al. (2018). However, it should be noted that the optical measurements mostly depend on Lyα, for which the strong IGM absorption could affect its line profile at the red side, and therefore redshift measurements based on Lyα are quite uncertain and often give larger values than the systemic redshifts. The broad CIV emission line is detected with associated strong absorption $\sim$ 13000 km s^{-1} blueward of the CIV peak. This feature indicates that this quasar is a broad absorption line (BAL) quasar, while its negative peak comes at the order gap of the GNIRS. We may detect a weak SiIV λ1400 tentatively. CIII] is known as another strong

emission line, but it falls at the order gap at $\lambda_{\rm obs} \sim 1.4\mu$m.

3.6.2 J1208-0200

J1208-0200 is a $z_{\rm opt} = 6.09$ quasar with $M_{1450,\rm M18} = -24.73$, which is similarly faint as J2239+0207. This quasar was observed for 3.7 hours in Gemini/GNIRS. Its relatively smooth Lyman break at $z \sim 6$ and broad Lyα make it difficult to estimate its redshift from the optical FOCAS spectrum. In the GNIRS spectrum, the power-law continuum is clearly detected over the all orders with the broad CIII] and CIV emission lines at $\lambda_{\rm obs} \sim 1.36\mu$m and $\lambda_{\rm obs} \sim 1.10\mu$m, respectively. The power-law fit gives the slope index of $\alpha_\lambda = -1.15 \pm 0.01$, from which the absolute magnitude of $M_{1450} = -24.32 \pm 0.14$ is obtained. This is ~ 0.4 magnitude brighter than in Matsuoka et al. (2018). J1208-0200 does not show clear MgII, although week excess is seen at $\lambda_{\rm obs} \sim 2.0\mu$m, where MgII peak is expected from the CIII] redshift. Since the apparent peak falls at the position of a strong sky line, its profile is highly uncertain. Therefore, we do not measure the MgII line profile for J12080200 and alternatively, the CIII redshift ($z_{\rm CIII]} = 6.104 \pm 0.001$) is adopted as its source redshift. As is clearly seen in Figure 3.12, CIII] and CIV have both broad and narrow bases. Also, the CIV has a sharp absorption at the very peak of the emission line, which indicates internal or external absorption (i.e., weak outflow or companion absorber).

3.6.3 J2216-0016

J2216-0016 at $z_{\rm opt} = 6.09$ is the faintest among the Gemini/GNIRS targets, for which we spent $t_{\rm exp} = 9.0$ hours. We detect the power-law continuum over the all orders and the broad MgII and CIV at $\lambda_{\rm obs} \sim 1.99\mu$m and $\lambda_{\rm obs} \sim 1.10\mu$m, respectively. Like J2239+0207, CIII] λ1909 falls at the order gap. The power-law fit gives the slope index of $\alpha_\lambda = -1.04 \pm 0.04$. The derived absolute magnitude is $M_{1450} = -23.57 \pm 0.37$, which is consistent with Matsuoka et al. (2018). Although the continuum is faint, MgII and CIV are clearly detected thanks to the long integration times. The blued side of CIII] is detected but its red side is noisy due to low transmission. The MgII redshift is $z_{\rm MgII} = 6.111 \pm 0.004$. CIV has broad and narrow bases with an asymmetric profile. There is a strong absorption at the peak of the narrower component.

In our another project on the host galaxy properties of the SHELLQs quasars based on the

Atacama Large Millimeter/sub-millimeter Array (ALMA), [CII] 158 μm emission line and the rest-frame far-infrared dust continuum were detected in our Cycle-4 observation (Izumi et al. submitted). The [CII] redshift is commonly used to represent the systemic redshift of high-redshift galaxies and quasars because this emission is from the photo-dissociation regions of galaxies and not affected by the outflowing kinematics of the black hole accretion disks as it is the case for the emission lines from the broad-line region gas (e.g., Shen et al., 2016; Wang et al., 2016). The [CII] redshift of J2216-0016 is $z_{[\mathrm{CII}]} = 6.0962 \pm 0.0003$. It follows that the CIV blueshift is $\Delta v_{\mathrm{blueshift}} = 748$ km s^{-1}. Since it is a BAL quasar indicated by the NV absorption (Matsuoka et al., 2016) and also by spatially extended [CII] components (Izumi et al. in prep.), the CIV offset would also be related to the nuclear outflows.

3.6.4 J0859+0022

J0859+0022 at $z_{\mathrm{opt}} = 6.39$ is one of the targets in VLT/X-SHOOTER. Its observed y-band magnitude is the faintest among the five targets in this study. A deep spectroscopy was carried out for 7.2 hours in NIR arm and 6.5 hours in VIS arm, Its spectrum is characterized by extremely weak continuum and strong narrow emission lines. In Figure 3.9, the top panel covers the all emission lines, while the middle panel gives the enlarged view of the continuum regions. The continuum slope index is typical ($\alpha_\lambda = -1.60 \pm 0.04$). However, the absolute magnitude of $M_{1450} = -23.09 \pm 0.43$ is 1 magnitude fainter than the optical measurement. This is likely due to the low signal-to-noise ratio of the optical continuum in Matsuoka et al. (2018), which spent only 30 minutes. The obtained absolute brightness is approximately fainter by more than an order of magnitude than any other $z > 6$ quasars whose NIR spectra have been taken (e.g., Jiang et al., 2007; Willott et al., 2010a; De Rosa et al., 2014). As described in Section 3.7 in greater detail, the power source of J0859+0022 is a $M_{\mathrm{BH}} = 10^7 M_\odot$ black hole, which is the least massive at $z > 6$. Strong emission lines of MgII and CIV are detected in the NIR arm, while Lyα and NV are visible in the VIR arm. The MgII redshift is $z_{\mathrm{MgII}} = 6.3886 \pm 0.0003$.

In the VIS arm, Lyα and NVλ1240 are clearly detected, as is also reported in the discovery paper. Figure 3.14 show the optical spectrum with the extrapolated best-fit continuum model. The rest-frame equivalent width of Lyα+NV is measured with the method presented in Diamond-Stanic et al. (2009). Based on the best-fit continuum model, fluxes over the continuum at the

rest-frame $\lambda_{\rm rest} = 1160-1290$Å are integrated and normalized by the continuum level at $\lambda_{\rm rest} =$ 1215Å. As a result, the Lyα + NV of J0859+0022 is very strong with EW(Lyα + Nv)= 269.5 ± 0.3Å or log EW(Lyα + Nv) = 2.431. Bañados et al. (2016) compile the 117 PS1 quasars at $z \sim 6$ to show $<$ log EW(Lyα + Nv) $>= 1.542 \pm 0.391$. Therefore, J0859+0022 deviates from their mean value by 2.3σ and is higher than any PS1 quasars. Such a strong Lyα emission is also implied from the broad-band photometry. Figure 3.13 shows the HSC $i-z$ vs $z-y$ colors of the SHELLQs quasars except two $z > 6.5$ quasars (including J1205-0000). The four Gemini and VLT targets at $z \sim 6$ are shown as red. It is clear that J0859+0022 has an extremely red $i-z$ color and blue $z-y$ color, which is distinguishable from the others and the model color track assuming the typical quasar SED. Whether this quasar is a type-I or type-II quasar is discussed in Section 3.8.2. In the ALMA observation of J0859+0022, its [CII] redshift is $z_{\rm [CII]} = 6.3903 \pm 0.0005$.

3.6.5 J1205-0000

J1205-0000, the highest redshift quasar among the targets in this study at $z_{\rm opt} \sim 6.7-6.9$, is another VLT/X-SHOOTER target for which a 10 OB observation was executed. As discussed in Matsuoka et al. (2016), its optical spectrum is highly complicated without apparent Lyα emission, which makes the optical redshift measurement uncertain. From the deep X-SHOOOTER spectrum, we find that J1205-0000 has a remarkably flat continuum as shown in the bottom panel of Figure 3.9. What is also notable is that, despite its faintness in the optical range, this quasar is detected in the VIKING survey ($J = 21.95 \pm 0.21$, $H = 21.49 \pm 0.34$, $Ks = 20.73 \pm 0.18$)[5], whose depth is much shallower than the HSC-SSP ($J_{\rm lim,5\sigma} \sim 22$), and also in the WISE $W1$ and $W2$ ($W1 = 19.98 \pm 0.15$, $W2 = 19.65 \pm 0.23$)[6]. Figure 3.15 shows the broad-band SED of J1205-0000 based on the optical HSC-SSP and near-infrared VIKING and WISE ($W1$,$W2$). Considering that the wavelength flux density falls from y to $W2$ by almost an order of magnitude in the case of a typical type-I quasar at $z \sim 7$ (assuming $\alpha_\lambda = -1.5$), the flat broad-band SED shape and the red color of $y - W2 = 2.96$ is quite unusual. Therefore, this quasar should be classified as a "red quasar", which is at the intermediate phase of dusty starburst and type-I quasar. Moreover, it is intriguing that there are double broad absorption lines (BALs) blueward of the CIV and NV line

[5]The VIKING magnitudes are from the data release 4.
[6]The WISE magnitudes are from the ALLWISE data release November 13, 2013

positions, both of which are visible in Figure 3.2 and Figure 3.9. Figure 3.10 shows the optical part (VIS arm) of the X-SHOOTER spectrum. This extreme and double BAL feature of J1205-0000 suggests the presence of episodic nuclear outflow during the intense star formation and BH growth phase. Indeed, a study of red quasars also reports a extreme BAL quasar at $z = 4.36$ (Ross et al., 2014)[7].

The dust-obscured population is the key to understand the quasar evolution in the sense that they would be in the transitional phase from dusty starburst to unobscured type-I quasars. This corresponds to the "Blowout" phase in the schema of the quasar growth in Hopkins et al. (2008) and is in the similar phase to the dust obscured galaxies (e.g., Dey et al., 2008; Toba et al., 2015). Since red quasars are easily missed in the ordinary optical color selection for unobscured quasars, dedicated searches have been carried out by mostly combining optical wide-field surveys with radio and near-infrared data (e.g., Glikman et al., 2007). J1205-0000 is the first red quasar found in the reionization epoch thanks to the deep imaging of the HSC-SSP. This quasar would provide crucial information on how the gigantic black holes can grow within the short timescale of the early universe.

To model J1205-0000's continuum, intrinsic power-law and internal extinction are taken into account. Since it is too complicated if both components are fitted simultaneously with the current spectral quality and coverage, the continuum slope is fixed at $\alpha_\lambda = -1.5$ and the color excess $E(B-V)$ due to internal dust extinction is measured assuming the Calzetti extinction law (Calzetti et al., 2000). The Calzetti law is commonly used to take into account the dust reddening of starburst galaxies. The color excess $E(B-V)$ of J1205-0000 is first determined by fitting the intrinsic power-law continuum of $\alpha_\lambda = -1.5$ to the broad-band SED taking advantage of the wide wavelength coverage. Only VIKING and WISE photometry is used because HSC-i, z are highly affected by the IGM absorption and HSC-y is affected by the Lyman break and Lyα emission. The color excess derived in this method is $E(B-V) = 0.27 \pm 0.03$. We scale the power-law + extinction model to match with the X-SHOOTER spectrum at the continuum regions for fine tuning. In the obtained spectrum, MgII is detected at $\lambda_{\rm obs} = 2.16 \mu m$ ($z_{\rm MgII} = 6.7071 \pm 0.0009$) over the red continuum. The MgII flux of the observed spectrum is $F_{\rm MgII} = 14.7 \pm 0.8 \times 10^{-17}$ erg cm^{-2} s^{-1} and the extinction-corrected flux assuming the best-fit color excess is $F_{\rm MgII} = 9.0 \pm 0.5 \times 10^{-16}$

[7] J101439.51+413830.6 (Figure 9 of this paper)

erg cm^{-2} s^{-1}. On the other hand, CIV is not clearly seen in the current spectrum, while several absorption lines are at the blue side of the expected CIV position from the MgII redshift.

3.7 Black Hole Mass

Broad emission lines of quasars originated from the Doppler motions of broad-line region gas can be used to estimate the black hole mass, with the assumption that the gas is gravitationally bounded to the central SMBHs. The mass of a super massive black hole can be denoted as:

$$M_{\rm BH} = f G^{-1} R_{\rm BLR} v_{\rm BLR}^2 \tag{3.3}$$

where G is the gravitational constant, $R_{\rm BLR}$ is the distance from the black hole to the broad-line regions, and $v_{\rm BLR}$ is the velocity of the orbiting broad-line region gas around the central black hole. The the scaling factor f takes into account the geometry. For the MgII-based BH mass estimate of the quasars with MgII detections, we follow the mass-scaling relation given in Vestergaard & Osmer (2009), which utilizes the widths of broad emission lines and the continuum luminosity (the so-called "single-epoch" method):

$$M_{\rm BH}({\rm MgII}) = 10^{6.86} \left(\frac{{\rm FWHM(MgII)}}{10^3 \ {\rm km \ s^{-1}}} \right)^2 \left(\frac{\lambda L_\lambda \ (3000{\rm \AA})}{10^{44} \ {\rm erg \ s^{-1}}} \right)^{0.5} M_\odot \tag{3.4}$$

where FWHM is the MgII line FWHM and λL_λ (3000Å) is the monochromatic luminosity at rest-frame 3000Å. This method is commonly used for black hole mass measurements at high-redshift where direct measurements of the distance of broad-line region with the reverberation mapping is difficult. The single-epoch method is made possible due to the tight correlation between the continuum luminosity and the broad-line region distance (e.g., Kaspi et al., 2005). For the CIV-based mass estimate, the empirical relationship obtained in Vestergaard & Peterson (2006) is used:

$$M_{\rm BH}({\rm CIV}) = 10^{6.66} \left(\frac{{\rm FWHM(CIV)}}{10^3 \ {\rm km \ s^{-1}}} \right)^2 \left(\frac{\lambda L_\lambda \ (1350{\rm \AA})}{10^{44} \ {\rm erg \ s^{-1}}} \right)^{0.53} M_\odot . \tag{3.5}$$

Note that the two relationships are calibrated with the reverberation mapping result of Peterson et al. (2004). It is not a obvious assumption that the broad line region is virialized at $z > 6$ and the

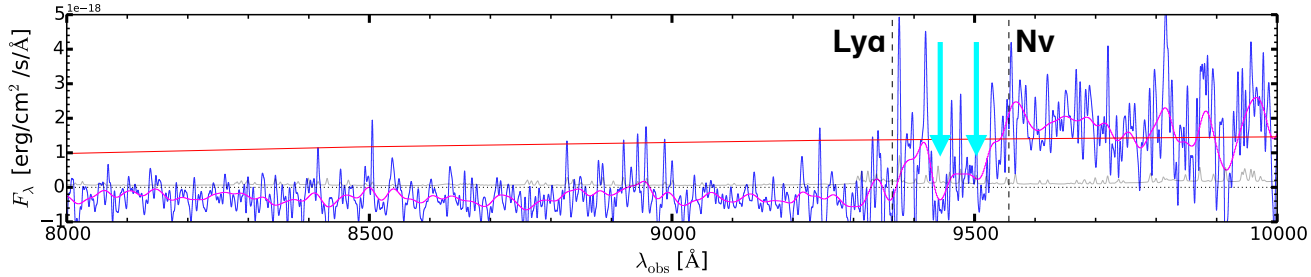

Figure 3.10: The VIS arm spectrum of J1205-0000 (blue). The same spectrum with additional 7-pixel binning before smoothing is shown in magenta. The vertical lines show the expected positions of Lyα and NV based on the MgII redshift. The best-fit power-law (plus host galaxy extinction) is shown in red.

Table 3.3: Emission Line Measurements

	J2239+0207	J1208-0200	J2216-0016	J0859+0022	J1205-0000
λL_{3000} (10^{45} erg s^{-1})	4.7 ± 1.4	4.3 ± 0.6	2.3 ± 0.8	1.0 ± 0.4	84 ± 16^c
FWHM$_{\rm MgII}$ (km s^{-1})	4030 ± 360	⋯	4160 ± 430	857 ± 60	1360 ± 78
$F_{\rm MgII}$(10^{-17} erg cm^{-2} s^{-1})	12 ± 1	⋯	7.0 ± 0.8	12 ± 1	36 ± 3^c
FWHM$_{\rm CIII]}$ (km s^{-1})	⋯	1721 ± 128	⋯	⋯	⋯
$F_{\rm CIII]}$ (10^{-17} erg cm^{-2} s^{-1})	⋯	16.1 ± 0.1	⋯	⋯	⋯
FWHM$_{\rm CIV}$ (km s^{-1})	5510 ± 590^a	2660 ± 120^b	2290 ± 170^b	1371 ± 16	⋯
$F_{\rm CIV}$ (10^{-17} erg cm^{-2} s^{-1})	24 ± 3^a	46.6 ± 0.2^b	38.1 ± 0.3^b	22.1 ± 0.4	⋯
$z_{\rm opt}$	6.26	6.2	6.09	6.39	$6.7-6.9$
$z_{\rm MgII}$	$6.241 \pm 0.004^*$	⋯	6.111 ± 0.004	6.3877 ± 0.0003	$6.7071 \pm 0.0009^*$
$z_{\rm CIII]}$	⋯	$6.104 \pm 0.001^*$	⋯	⋯	⋯
$z_{\rm CIV}$	6.242 ± 0.005^a	6.100 ± 0.001^b	6.081 ± 0.001^b	6.3931 ± 0.0002	⋯
$z_{\rm [CII]}$	⋯	⋯	$6.0962 \pm 0.0003^*$	$6.3903 \pm 0.0005^*$	⋯

The systemic redshift of each source is marked with asterisk. [CII] redshift determined in Izumi et al. (submitted) is used if available, while MgII and CIII] redshift is used, if not.

[a] The emission line profile is affected by a broad absorption at blue side.

[b] The emission line has an broad absorption at the line peak.

[c] The luminosity and MgII of J1205-0000 are corrected for the internal extinction with $E(B-V) = 0.27$.

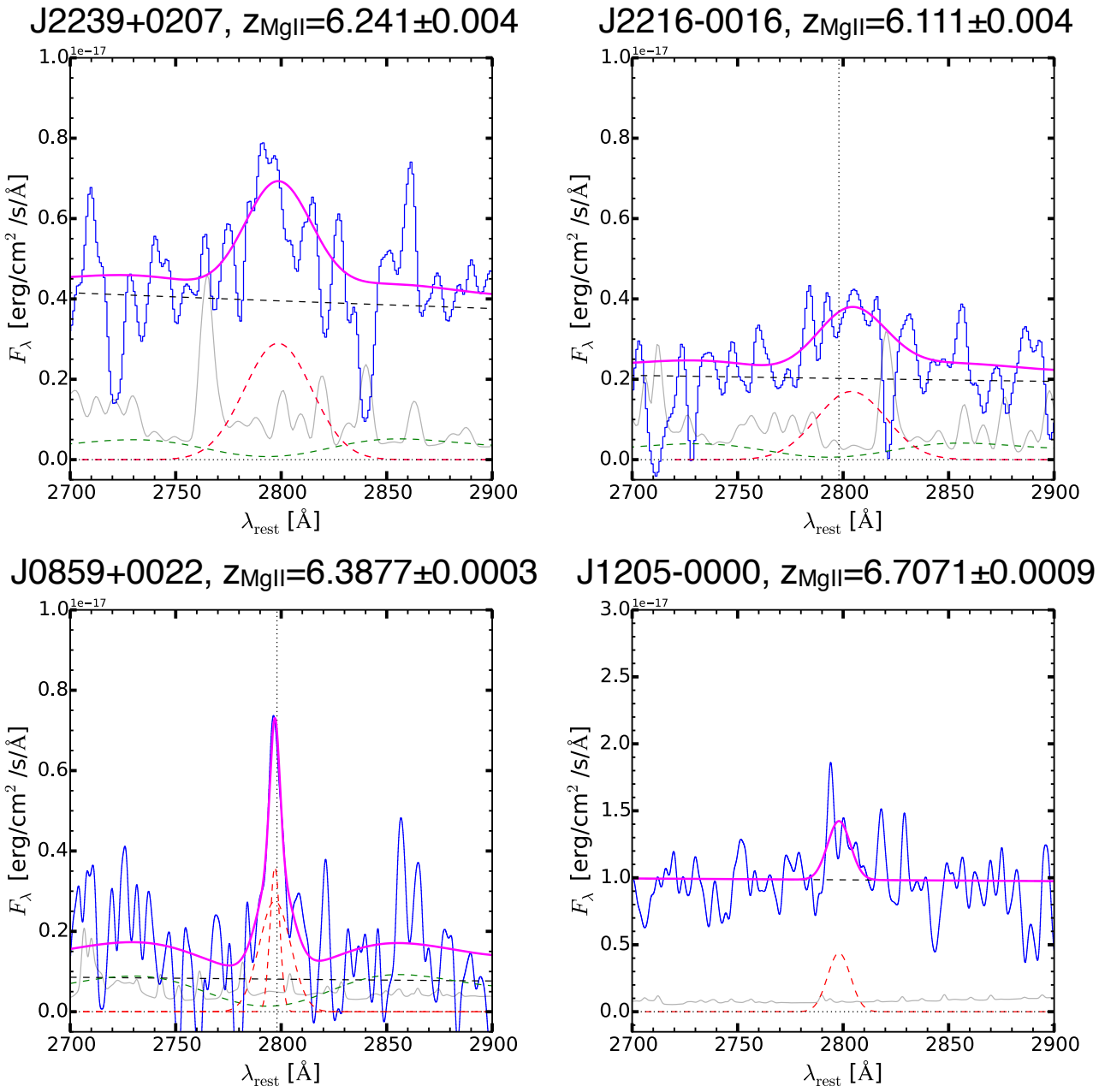

Figure 3.11: Rest-frame spectra of four SHELLQs quasars around MgII λ2798 emission lines. Nominal redshift of each source is used to correct the redshifted spectra (MgII redshift for J2239+0207 and J1205-0000, and [CII] redshift for J2216-0016 and J0859+0022). For the latter two, the expected peak positions from [CII] redshift are indicated with vertical dotted lines. For each source, the best-fit spectral model is shown as magenta, while individual component is also shown (power-law: black, FeII pseudo-continuum: green, Gaussian fit for MgII emission: red). The expected peak positions from [CII] redshift (Table 3.3) are indicated for J2216-0016 and J0859+0022 with vertical dotted lines.

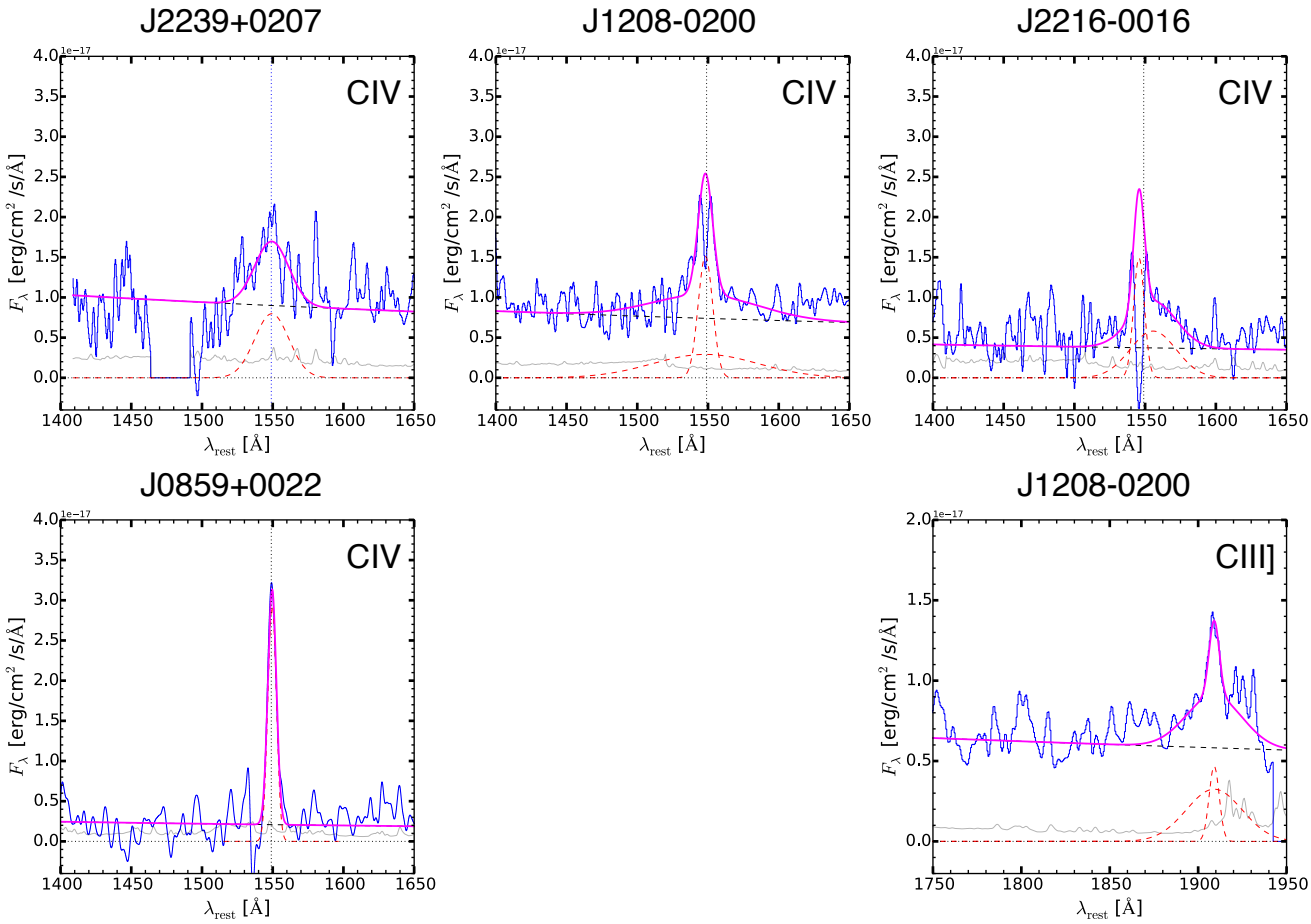

Figure 3.12: Rest-frame spectra of four SHELLQs quasars around CIV λ1549 emission lines and CIII] for one source (J1208-0200). The absorption regions at the peak of CIV of J1208-0200 and J2216-0016 are masked in the line fitting. The expected peak positions from the systemic redshift (Table 3.3) are indicated with vertical dotted lines.

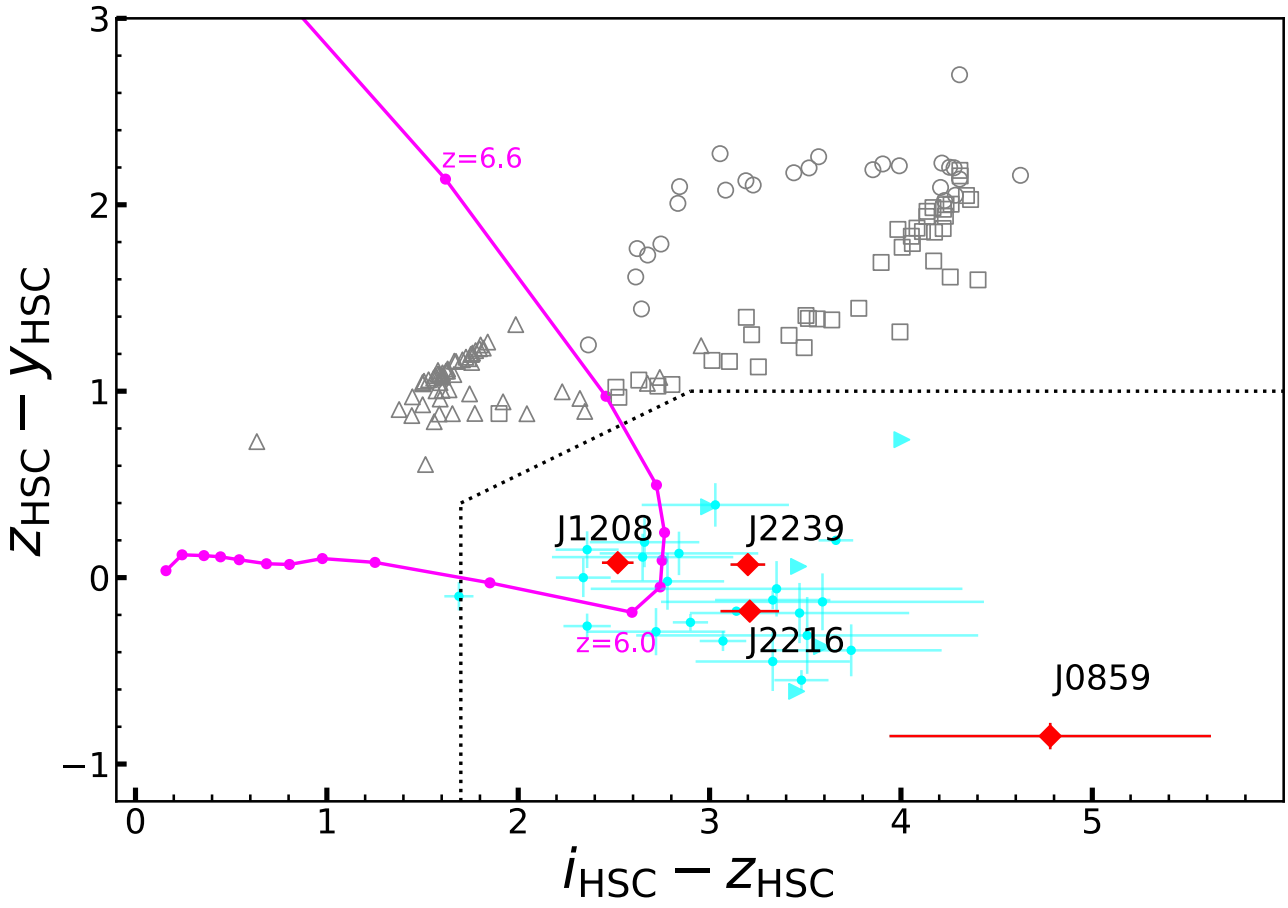

Figure 3.13: $i-z$ vs $z-y$ color diagram. The SHELLQs quasars discovered in Matsuoka et al. (2016, 2018) except two at $z > 6.5$ (including J1205-0000) are shown as cyan, while the four $z \sim 6$ quasars in this study are shown as red. 2σ limiting lower-limits are shown as triangle for those undetected in HSC-i. The solid lines, grey symbols are same as Figure 2.2.

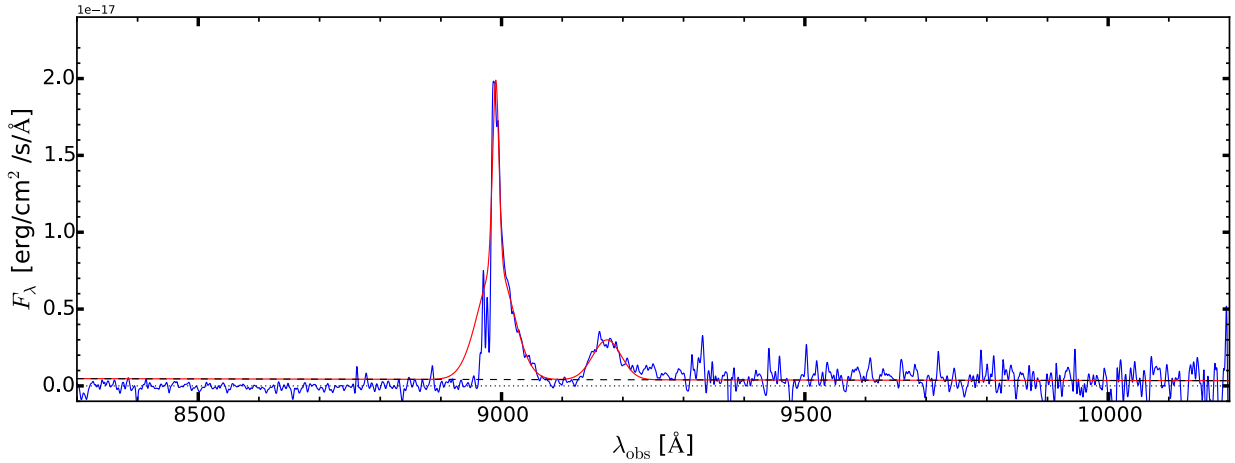

Figure 3.14: The VLT/X-SHOOTER spectrum of J0859+0022 in the VIS arm with the best-fit continuum plus Gaussian model.

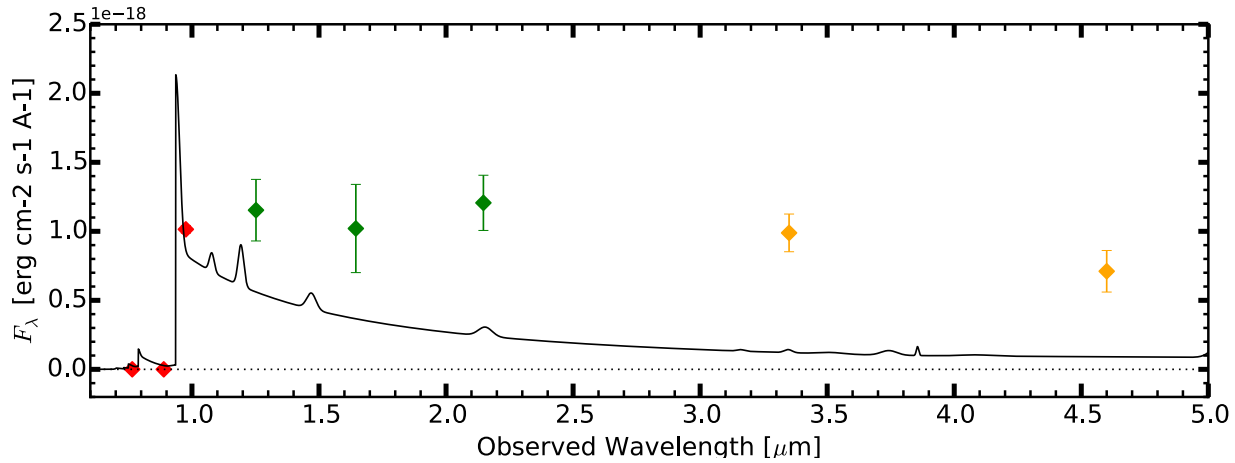

Figure 3.15: Broad-band SED of J1205-0000 from i to $W2$ (HSC: red, VIKING: green, WISE: orange). A typical SED model of a $z = 6.7$ quasar assuming $\alpha_\lambda = -0.44$ (Vanden Berk et al., 2001) is scaled to the HSC-y magnitude of J1205-0000 is shown in solid line. The observed broad-band SED is notably flat, which suggests its red continuum, i.e., large internal extinction.

same scaling relations can be used. However, we assume that the relation holds at high redshift, as is the same for other studies on $z > 6$ quasars (e.g., Bañados et al., 2017), and its validity is not the scope of this paper.

Subsequently obtained after the black hole mass measurement is the Eddington luminosity of the quasars, because the Eddington luminosity, $L_{\rm Edd}$ is a function of black hole mass:

$$L_{\rm Edd} = 1.3 \times 10^{38} \left(\frac{M_{\rm BH}}{M_\odot} \right) \ {\rm erg\ s^{-1}}. \tag{3.6}$$

We measure the Eddington luminosity from $M_{\rm BH}$(MgII) for J2239+0207 and J2216-0016, while we use $M_{\rm BH}$(C IV) for J1208-0200. We further compute the bolometric luminosity $L_{\rm bol}$ to derive the Eddington ratios defined as the ratio of the Eddington luminosity over the bolometric luminosity. Bolometric correction given in Shen et al. (2008) is applied to the observed monochromatic luminosity at rest-frame 3000Å:

$$L_{\rm bol} = 5.15\ \lambda L_\lambda (3000{\rm \AA})\ {\rm erg\ s^{-1}}. \tag{3.7}$$

In Table 3.4, the $M_{\rm BH}$ estimates obtained from MgII and CIV emission lines are listed. The uncertainties of the black hole mass are derived by propagating the measurements errors of the line widths and the absolute magnitudes. The systematic uncertainty due to the MgII-based calibration is ≈ 0.3 dex (Shen et al., 2008), although it is not included in the table. As a result, we find that the obtained MgII-based $M_{\rm BH}$ spans a wide range of $M_{\rm BH} \sim 10^{7-9} M_\odot$ and accordingly a wide range of the Eddington ratio of $L_{\rm bol}/L_{\rm Edd} \sim 0.2-8.6$. Figure 3.16 compares the SHELLQs quasars with the other $z > 6$ quasars whose MgII-based $M_{\rm BH}$ measurements are available (Jiang et al., 2007; Willott et al., 2010a; De Rosa et al., 2011; Wu et al., 2015; Mazzucchelli et al., 2017b; Bañados et al., 2017). Note that the quoted $M_{\rm BH}$ measurements for all $z > 6.5$ quasars are from the recently updated values in Mazzucchelli et al. (2017b). In Figure 3.16, $M_{\rm BH}$ is recalculated using the same calibration to the SHELLQs quasars and the cosmology adopted in this paper. The error bars of the SHELLQs quasars are the measurement uncertainties of the line width and power-law continuum. Such a variation in the black hole properties at $z > 6$ is not reported in the studies of $z > 6$ quasars, which mostly accretes at the maximum rate, i.e. $L_{\rm bol}/L_{\rm Edd} \sim 1$. The different trend seen in the SHELLQs quasars is likely because our targets are low-luminosity

quasars, which enables us to explore the sub-Eddington accreting super massive black hole with $M_{\rm BH} \gtrsim 10^9 M_\odot$. Note that Willott et al. (2010a) and Mazzucchelli et al. (2017b) show that a few CFHQS and PS1 quasars have the similarly low Eddington ratios.

On the other hand, J0859+0022 is the first $M_{\rm BH} \sim 10^7 M_\odot$ black hole at $z > 6$ as expected from the narrow MgII and weak continuum. As mentioned in Section 3.6.4, J0859+0022 is selected in this study because its absolute magnitude obtained in the discovery spectrum is much brighter than the near-infrared measurement. Its high Eddington ratio is comparable to some of the luminous $z > 6$ quasars such as PSO J247+24 ($L_{\rm bol} = 1.7 \times 10^{47}$ erg s^{-1}, $M_{\rm BH} = 5.2 \times 10^8 M_\odot$; Mazzucchelli et al. 2017b) and CFHQS J0210-0456 ($L_{\rm bol} = 2.5 \times 10^{46}$ erg s^{-1}, $M_{\rm BH} = 8.0 \times 10^7 M_\odot$; Willott et al. 2010a). The red quasar, J1205-0000 has both high black hole mass ($M_{\rm BH} = 9.3 \pm 1.1 \times 10^8 M_\odot$) and Eddington ratio ($L_{\rm bol}/L_{\rm Edd} = 3.6$). The high accretion rate is consistent with the picture that super massive black holes have a plenty of cold gas available for the black hole growth during intense dusty starburst triggered by the major mergers. At low redshift, Kim et al. (2015) show that 16 red quasars at $z \sim 0.7$ have the Eddington ratio of, on average, $L_{\rm bol}/L_{\rm Edd} = 0.69$, which is significantly higher than normal quasars at the same redshift range. J1205-0000 shows that it is also the case at higher redshift, perhaps with higher accretion rates at $z > 6$. We assume the intrinsic continuum slope of $\alpha_\lambda = -1.5$, while various studies derive the mean continuum slope of quasars with the range of $-1.7 \lesssim \alpha_\lambda \lesssim -1.2$ (e.g., Fan et al., 2000; Vanden Berk et al., 2001; Selsing et al., 2016). Within this range the color excess of J1205-0000 is $E(B-V) \sim 0.2-0.3$, which is converted to $\sim 10\%$ difference of the intrinsic luminosity correction based on the SED fitting to its broad band photometry, as applied in Section 3.6.5. This additional uncertainty does not affect much the $M_{\rm BH}$ of J1205-0000 within the measurement error. Nevertheless, more precise measurements of intrinsic continuum level is preferable around the Paschen or Balmer series lines which are another mass estimators and less affected by the dust extinction.

The CIV-based $M_{\rm BH}$ is obtained for all but J1205-0000. J2239+0207 has a broad absorption at the blue side of the apparent CIV peak and J1208-0200 and J2216-0016 are affected by absorption at the peak (Figure 3.12), which may affect the FWHM measurements. Albeit with those unusual line profiles, the two mass estimators give difference of a factor of two for J2239+0207 and J0859+0022. J2216-0016 has the biggest difference of $\Delta \log M_{\rm BH} = 0.67 M_\odot$, but it is still within the 1σ uncertainty taking into account the 0.3 dex systematic uncertainty due to the single-epoch

mass estimate (Shen et al., 2008; Willott et al., 2010a; De Rosa et al., 2014). In the following discussion, MgII-based $M_{\rm BH}$ is used except J1208-0200 (no MgII detection) considering the complicated line profiles of CIV and possible bias due to nuclear outflows.

3.8 Discussion

3.8.1 Seed Mass

The mass measurements of high-redshift quasars provide insights into the seed black holes at their birth. Figure 3.17 shows the estimated growth history of the five SHELLQs quasars in this study. The growth timescale given in Equation 1.2 is calculated with the radiation efficiency of $\eta = 0.1$ (i.e., 10% of the energy of the accreting mass is converted to radiation) commonly used in the literatures. Two scenarios are considered here: one is that the black hole constantly accretes at the Eddington ratio obtained in Section 3.7. The second one assumes that the black hole grows at the Eddington limit. The duty cycle of a unity is assumed; therefore the growth history considered here is the most efficient cases, while in reality the accretion onto the central black holes is regulated by the balance between the accreting matter and radiative negative feedback. Especially, the super-Eddington phase ($L_{\rm bol}/L_{\rm Edd} > 1$) is intermittent (e.g., Di Matteo et al., 2008). In Figure 3.17, the black hole growth traces back to $z = 30$ when the first star, galaxy, and black hole start to be formed in the universe. For comparison, the growth history of three representative luminous $z > 6$ quasars, J1120+0641 (Mortlock et al., 2011), J0100+2802 (Wu et al., 2015), and J1342+0928 (Bañados et al., 2017) is also shown. Among the five quasars in this study, J0859+0022 and J1208-02000 with the super-Eddington accretion rates can easily be explained with the Pop-III scenario in the either case of the assumed accretion rates. This is different from the seed mass arguments on J1120+0641 (Mortlock et al., 2011), for which even the constant Eddington accretion cannot reach to the Pop-III range, which requires other formation pathways with more massive seed black holes or more efficient hyper-Eddington phase (Inayoshi et al., 2016a). On the contrary, the initial growth of J2216-0016 and J2239+0207 cannot be explained with neither the Pop-III nor direct-collapse scenario with the current low accretion rates, while $M_{\rm BH} \sim 10^8 M_\odot$ black holes can easily be attained at $z \sim 6$ with the continuous Eddington-limit

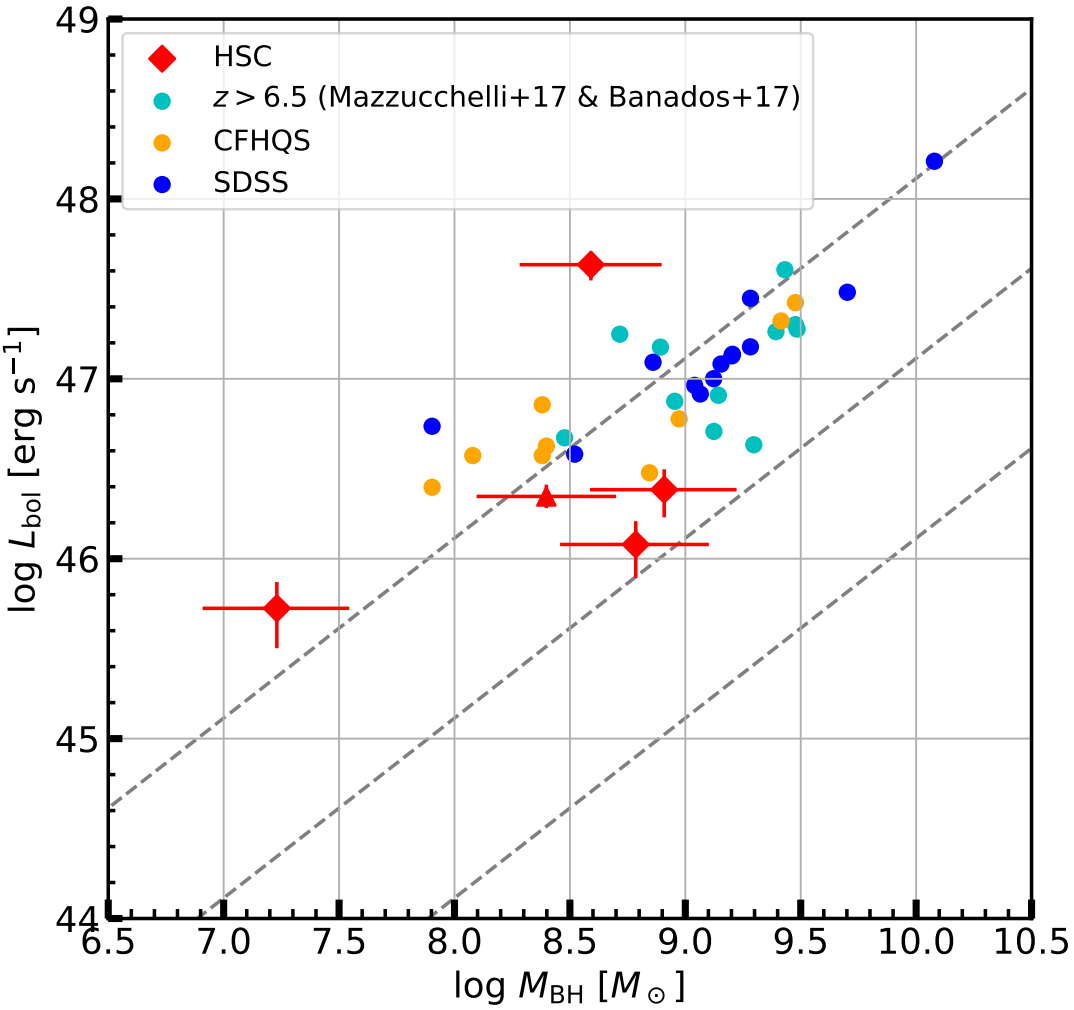

Figure 3.16: The distribution of black hole mass and bolometric luminosity for known $z > 6$ quasars whose MgII-based $M_{\rm BH}$ have been measured. The mass and luminosity are adjusted to the same scaling relation and cosmology in this study. The four SHELLQs quasars are shown as red diamonds while J1208-0200 whose $M_{\rm BH}$ is based on CIV, is shown as red triangle. Error bars show the 1σ uncertainties. In the errors of black hole mass, systematic errors of 0.3 dex in the virial mass measurements are included. SDSS quasars are from Jiang et al. (2007), De Rosa et al. (2011), and Wu et al. (2015). CFHQS quasars are from Willott et al. (2010a). $z > 6.5$ quasars are from the compilation of Mazzucchelli et al. (2017b, except J1205-0000) and from Bañados et al. (2017). The diagonal lines correspond to the Eddington ratio of $L_{\rm bol}/L_{\rm Edd} = 1, 0.1, 0.01$ from top to bottom.

accretion. Their nature is revisited in Section 3.8.3. Finally, J1208-0200 may require the massive seed of $M_{\rm seed} \sim 10^4 M_\odot$ considering its moderate Eddington ratio, while the constraint is not as stringent as the sub-Eddington accreting black holes.

3.8.2 Is J0859+0022 a type-II AGN?

Among the five $z > 6$ quasars in this study, J0859+0022 shows an intriguing SED. As aforementioned in Section 3.6.4, this quasar has a weak continuum and strong narrow emission lines, which can be explained by a type-II. The bolometric luminosity $L_{\rm bol} = 5.2 \times 10^{45}$ erg s^{-1} is at the classical boundary of Seyfert galaxies and quasars. Alexandroff et al. (2013) present their type-II quasar candidates at $2 < z < 4.3$ extracted from the BOSS survey. The absolute magnitudes of their 145 type-II candidates are $M_{1450} \sim -23$ and the CIV and Lyα emission lines have narrow profiles with FWHM < 2000 km s^{-1}, which is quite similar to J0859+0022. To compare with those lower-redshift type-II quasars, the Lyα and NV emission lines of J0859+0022 detected in the X-SHOOTER VIS arm are fitted with double and single Gaussian, respectively. For Lyα, only the red side of the emission line is used not to be affected by the IGM absorption. As a result, J0859+0022's Lyα is fitted with FWHM$_{\rm Ly\alpha,broad} = 2256 \pm 44$ km s^{-1} and FWHM$_{\rm Ly\alpha,narrow} = 407 \pm 10$ km s^{-1}, which is even narrower than the type-II composite spectra of Alexandroff et al. (2013). NV is fitted with FWHM$_{\rm NV} = 1794 \pm 22$ km s^{-1}.

Even with those observed properties in mind, J0859+0022 is assumed to be a low-luminosity type-I AGN in the following sections for two reasons. First, the blue continuum of J0859+0022 typical for a type-I quasar indicates the unobscured component, while the Alexandroff's Class A candidates have flat continuum likely contributed from host galaxies. Second, the apparent iron components further supports the type-I nature of J0859+0022. Specifically, the bumps at the both sides of MgII in the X-Shooter spectrum in Figure 3.11 should be noted. The broad component of Lyα could be another support of our assumption, but as mentioned above, the broad component is still narrower than the Lyα of composite type-II candidates in Alexandroff et al. (2013), and this should not be the primarily reason to classify J0859+0022 to be a type-I. Therefore, J0859+0022 is likely a low-luminosity type-I AGN and perhaps the high-redshift analogue of the local Narrow Line Seyfert 1 galaxies (Osterbrock & Pogge, 1985; Constraintin & Shields, 2003).

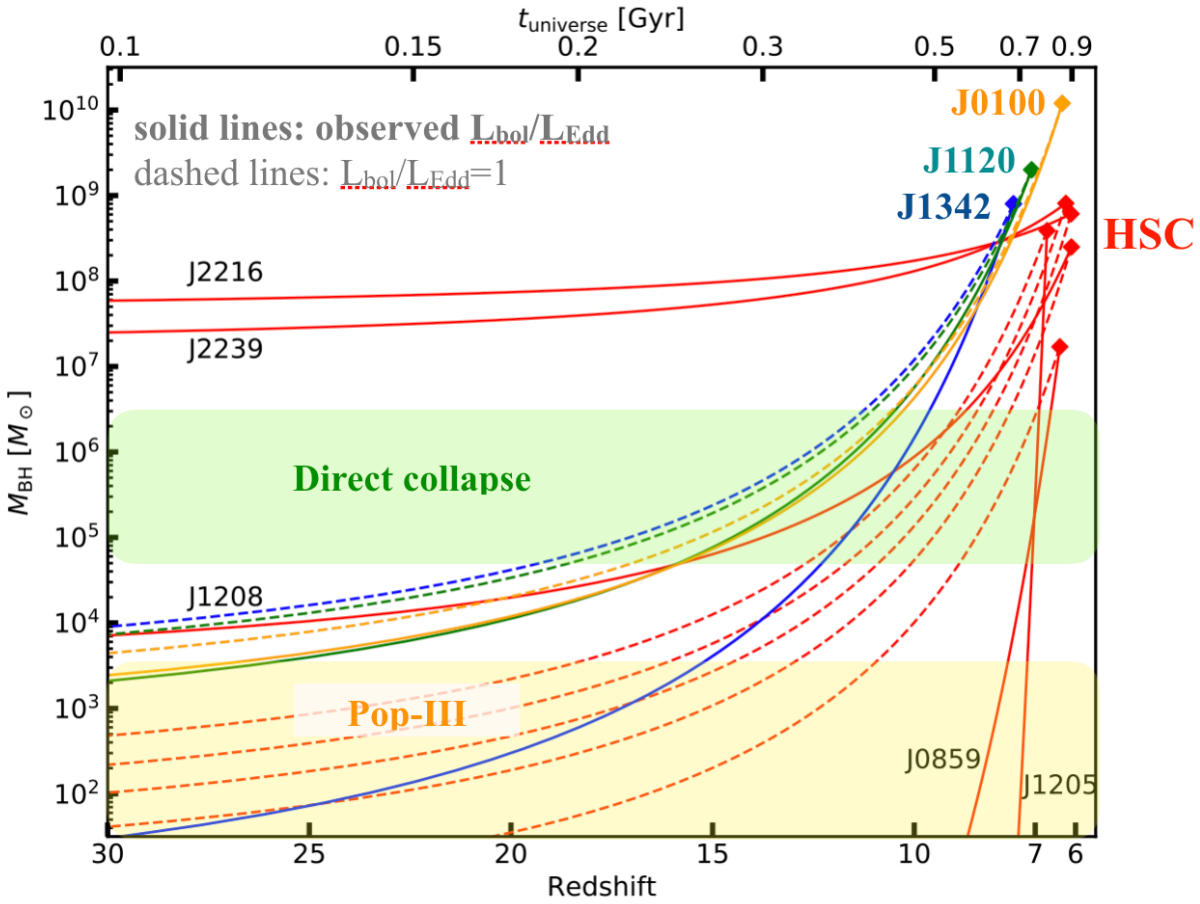

Figure 3.17: Estimated early growth history of the SHELLQs quasars (red) in the case of (i) the observed Eddington ratio in solid lines and (ii) the Eddington ratio in dashed lines. The duty cycle of a unity is assumed for giving the upper limit of the seed black hole mass. To aid visualization, the object names are indicated for the SHELLQs quasars in the first case. For comparison withe the low-luminosity quasars, three most peculiar quasars at $z > 6$ are also shown (J1120+0641 at $z = 7.1$ from Mortlock et al. 2011 in green, J0100+2802 at $z = 6.3$ from Wu et al. 2015 in orange, and J1342+0928 at $z = 7.5$ from Bañados et al. 2017 in blue). The redshift range shown is from $z = 30$ to $z \sim 6$, while the first star and black hole formation occur at $z \sim 10-30$.

3.8.3 Eddington ratio distribution

Willott et al. (2010a) compile 17 CFHQS and SDSS quasars to show that at $z \sim 6$ the Eddington ratio distribution inclines toward higher accretion rates than $z \sim 2$ quasars selected with the same luminosity cut. In the lognormal scale, the Eddington ratio distribution of $z \sim 6$ quasars has a peak of $< \log L_{\rm bol}/L_{\rm Edd} >= 0.03$ with the dispersion of 0.28 dex. Shen et al. (2008) show that the Eddington ratio distribution at $z \lesssim 4$ is capped between $L_{\rm bol}/L_{\rm Edd} \sim 0.01-1$ and gets narrower at higher luminosity range. The narrowing of the Eddington ratio distribution is at least partly due to the cut off of the black hole mass function at $M_{\rm BH} \sim 10^{10} M_{\odot}$ throughout the cosmic history (Inayoshi et al., 2016b). While the distribution of the quasar luminosity is one of the way to address the global redshift evolution of super massive black holes (Section 2.5.1), the more physical quantities, black hole mass and accretion rate, better trace exactly how super massive black holes grow in the cosmological scale acting in concert with the host galaxy growth, while constraining those distributions require deep spectroscopy and thus is observationally expensive. Indeed, a countable number of studies present the mass function and Eddington ratio distribution at $z \gtrsim 1$ (e.g., Shen et al., 2008; Willott et al., 2010a; Vestergaard & Osmer, 2011; Schulze et al., 2015).

Obtaining the Eddington ratio distribution at fixed black hole mass for the SHELLQs quasars is impossible at this stage because the black hole mass has not been completely measured for a flux limited sample. The selection function of the SHELLQs quasars and the luminosity function are going to be presented in Matsuoka et al. (in prep.). Instead, it is still possible to compare the distribution of the observed Eddington ratio at fixed luminosity. Recent efforts on $M_{\rm BH}$ measurements of $z > 6$ quasars have increased the number of quasars whose $M_{\rm BH}$ are available to 38 (De Rosa et al. 2014, Wu et al. 2015, Mazzucchelli et al. 2017b, Bañados et al. 2017, and this study) over a wide luminosity range. Figure 3.18 shows the histogram of the lognormal Eddington ratio for the same $z > 6$ quasars shown in Figure 3.16, divided into two luminosity bins at $L_{\rm bol} = 10^{47}$ erg s^{-1}. J0859+0022 and J1205-0000 are removed from this analysis because J0859+0022 is beyond the magnitude cut of the original sample selection for $M_{\rm BH}$ measurements (Section 3.3), and red quasars would have systematically high Eddington ratios. In total, 17 quasars are included in the “luminous" bin and the other 19 (three of them are the SHELLQs quasars) are included in the “less luminous" bin. The $M_{\rm BH}$ measurements are not

completed in the SDSS and other quasar surveys; however those quasars are discovered with flux-limited quasar selections and selected for $M_{\rm BH}$ measurements based on redshift and observed magnitude. Therefore, there should be no selection bias in the Eddington ratio at fixed luminosity. As a result, the average Eddington ratio is comparable between the two luminosity bins but has a larger scatter in the more luminous quasars: Quasars in the luminous bin have on average $< \log L_{\rm bol}/L_{\rm Edd} >= -0.10 \pm 0.20$, while quasars in the less luminous bin have $< \log L_{\rm bol}/L_{\rm Edd} >= -0.14 \pm 0.41$. Notably, the average of each bin is smaller than in Willott et al. (2010a, $< \log L_{\rm bol}/L_{\rm Edd} >= 0.37$). This is primary because the sub-Eddington accreting quasars have recently been identified at $z > 6$ (Mazzucchelli et al., 2017b, and this study) and also because more than half of the CFHQS quasars exceed the Eddington limit. The reason why CFHQS quasars preferentially have high Eddington ratios compared to the SHELLQs quasars is unclear, perhaps simply because of the small (< 10) sample sizes in both studies.

The dispersion of the Eddington ratio is somewhat smaller than expected when the systematic uncertainty of the virial $M_{\rm BH}$ measurements (0.3 dex) is taken into account. This issue is pointed out in Shen et al. (2008). They show that luminosity cuts affect the observed distributions of virial black hole mass and Eddington ratio in such a way that the observed peaks of $\log M_{\rm BH}$ and $\log L_{\rm bol}/L_{\rm Edd}$ shift toward massive and low-accretion direction from the true underlying distributions due to the Malmquist bias (Malmquist, 1922): When a bottom-heavy distribution such as the luminosity function and the black hole mass function is observed with a certain luminosity cut, more less-luminous or less-massive black holes scatter into luminous or massive bins than the other way around. In their analysis of the SDSS DR5 quasars, the apparent Eddington ratio distributions at $z \lesssim 4.5$ have dispersions of $\sim 0.2-0.4$ dex in their luminosity bins, which is comparable to our results. In Figure 3.18, their best-fit Gaussian distribution for $3 < z \lesssim 4.5$ quasars at $\log L_{\rm bol} > 47$ erg s^{-1} is shown in grey ($< \log L_{\rm bol}/L_{\rm Edd} >= -0.57 \pm 0.30$). This figure apparently shows that $z \sim 6$ quasars have high Eddington ratio than the Shen et al. (2008)'s result; however careful consideration of the selection completeness for each sample is required to fairly compare the two samples.

The narrow distribution of the luminous quasars in this study indicates that $M_{\rm BH} \sim 10^{10} M_\odot$ black holes are rare at $z > 6$ and there is a cut off in the black hole mass function at this range. Such extreme populations can only be made if Pop-III remnant black holes with $M_{\rm seed} \sim 10^{2-3} M_\odot$

continuously accrete at the Eddington limit or seed black holes are already massive. The deep survey of the HSC-SSP has a potential to find $M_{\rm BH} \sim 10^{10} M_\odot$ black holes with sub-Eddington accretion ratio. However, small-scale physics around the black hole accretion disks would also prevents a seed black hole from growing over a certain limit (Inayoshi et al., 2016b) in the short timescale. To put it another way, the sub-Eddington accreting black holes, some of which are identified in this study, would be the remnants of the first quasars whose bursty mass growth occur at the earliest stage and their current growth is in the post-active phase already in the reionization epoch, in the context of the anti-hierarchical or the so-called “downsizing" trend of the growth of the super massive black holes (Ueda et al., 2003, 2014).

Regarding the quasar contribution to reionization (Chapter 2), we conclude in Section 2.5.1 that quasar contribution to reionization is minor based on the Suprime-Cam survey of $z \sim 6$ quasars. On the other hand, the “dead" quasars seen in this study would contribute more to the UV photon budget at higher redshift when they are most active. Given that the redshift evolution of the QLF faint end is not clear at $z \gtrsim 4$ (Akiyama et al., 2017), it is possible that the QLF faint-end slope is much steeper at $z \gtrsim 7$ and the relative contribution of quasars to the UV photons is larger than $z \sim 6$. In this sense, the more accurate measurements of the QLF and the larger number of $z \gtrsim 6$ SMBHs with mass measurements for the low-luminosity quasars is required to further discuss the reionization scenario.

Finally, although not discussed in detail in this thesis, the host galaxy properties of J2216-0016 and J0859+0022 are different from those of luminous quasars (Izumi et al., 2018). The star-forming activities of the host galaxies are ordinary with the star-formation rates of $\sim 10 M_\odot$ yr^{-1}, contrary to $> 100 M_\odot$ yr^{-1} for the luminous quasar hosts (e.g., Venemans et al., 2016). Moreover, the ratio of the dynamical mass ($M_{\rm dyn} \sim 10^{11} M_\odot$) to black hole mass is consistent or slightly lower compared with the local $M_{\rm BH} - \sigma$ relation. Therefore, we may witness the first “turning-off" phase of the galaxy-SMBH co-evolution at high redshift, which has not been seen for the most luminous $z > 6$ quasars. Since the mass ratio of such extreme populations are over the local relation, those are likely be the progenitors of the outliers in the local universe (van den Bosch et al., 2012; Trakhtenbrot et al., 2017; Martine-Navarro et al., 2018).

Table 3.4: Black Hole Mass and Eddington ratio

	J2239+0207	J1208-0200	J2216-0016	J0859+0022	J1205-0000
$M_{\rm BH}$(MgII) [$10^8 M_\odot$]	$8.1 \pm 1.9^*$	⋯	$6.1 \pm 1.6^*$	$0.17 \pm 0.04^*$	$3.9 \pm 0.6^*$
$M_{\rm BH}$(CIV) [$10^8 M_\odot$]	13 ± 3^a	$2.5 \pm 0.2^{a,*}$	1.3 ± 0.3^a	0.38 ± 0.08	⋯
$L_{\rm bol}/L_{\rm Edd}$(MgII)	$0.23 \pm 0.07^*$	⋯	$0.15 \pm 0.05^*$	$2.4 \pm 1.0^*$	$8.6 \pm 1.6^*$
$L_{\rm bol}/L_{\rm Edd}$(CIV)	0.15 ± 0.05^a	$0.67 \pm 0.09^{a,*}$	0.72 ± 0.24^a	1.1 ± 0.5	⋯

The mass and Eddington ratio discussed in the following sections are marked with asterisk. While the error in the mass is measurement errors, there is additional systematic uncertainty of 0.3 dex in the single-epoch mass measurement. [a] The CIV emission line is affected by the broad absorption at the blue side of the peak or at the peak.

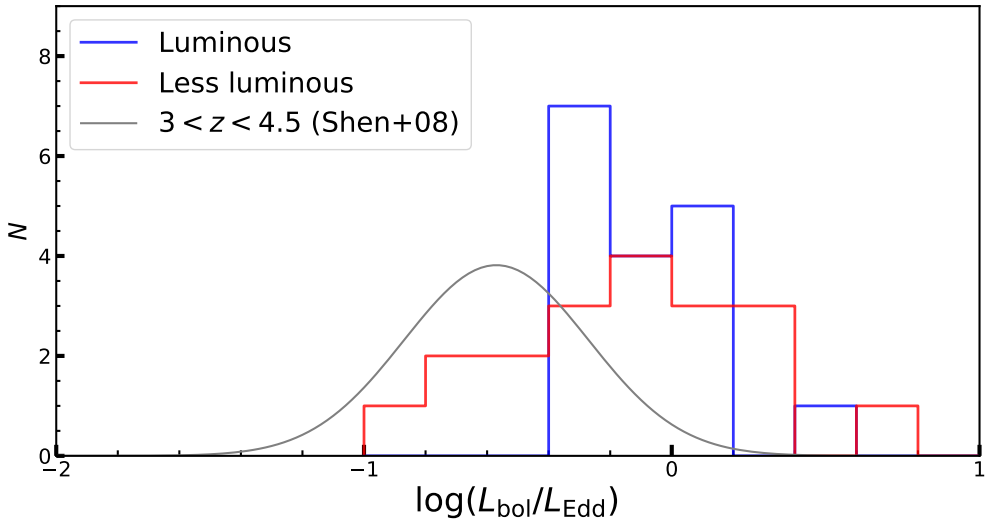

Figure 3.18: Histogram of the Eddington ratio in log scale for $z > 6$ quasars. 36 quasars from the literatures are divided into luminous ($L_{\rm bol} \geq 10^{47}$ erg s^{-1}, blue) and less-luminous ($L_{\rm bol} < 10^{47}$ erg s^{-1}, red) bins. Two SHELLQs quasars with peculiar SEDs, J0859+0022 and J1205-0000 are removed from the analysis. The observed Eddington ratio distribution for the SDSS DR5 quasars at $3 < z \lesssim 4.5$ from Shen et al. (2008) is shown in grey ($\log L_{\rm bol} > 47$ erg s^{-1}).

3.9 Summary

In this chapter, the black hole mass measurements of five low-luminosity quasars at $z > 6$ recently discovered by the HSC-SSP (Matsuoka et al., 2016, 2018) are presented. Among the current SHELLQs samples of 33 low-luminosity quasars, 5 quasars at $z_{\rm optical} = 6.1-6.8$ with the absolute magnitude of $M_{1450} \lesssim -23.8$ are selected for deep near-infrared spectroscopy with Gemini/GNIRS and optical-to-near-infrared spectroscopy with VLT/X-SHOOTER. Since the luminosity range of those quasars is fainter than previous studies of $M_{\rm BH}$ measurements at $z > 6$ mostly focusing on the extremely bright populations, or the most massive and active super massive black holes, this studies probe down the unexplored typical black hole populations in the reionization epoch.

The main findings from the observations can be summarized as follows:

1. From four quasars MgII emission lines are detected, while the profile is unclear for the other target (J1208-0200) because it has a smaller redshift than estimated from Lyα, and its MgII profile is highly affected by the strong sky emission. Other rest-frame UV broad emission lines such as CIV, CIII] are detected in some cases. Deep optical spectra including NV and Lyα are obtained in two X-SHOOTER targets. One of the X-SHOOTER targets, J0859+0022 has a blue continuum one magnitude weaker than expected in the optical discovery spectrum. Another X-SHOOTER target, J1205-0000 has a curved continuum with a remarkably flat broad-band SED up to $\lambda_{\rm obs} \sim 5\mu$m. This quasar is the first red quasar at $z > 6$ and its spectrum is characterized by a color excess of $E(B-V) = 0.27 \pm 0.03$ assuming the intrinsic power-law continuum of $\alpha_\lambda = -1.5$.

2. The near-infrared spectra are modeled with the combination of several components: power-law continuum, FeII pseudo-continuum, and emission lines modeled with single or double Gaussians. The continuum fitting is done by an iteration process, which allows us a reliable continuum subtraction at the emission line regions. The estimated power-law slope is in the range of typical type-I quasars except J1205-0000. The near-infrared redshifts are measured by the peak of the best-fit Gaussians. The obtained spectra are used to estimate the virial black hole mass based on MgII and CIV with the single-epoch method. The five SHELLQs quasars show a variety in the derived black hole mass with $M_{\rm BH} =$

$2\times10^7 - 9\times10^8 M_\odot$ and subsequently in the Eddington ratio of $L_{\rm bol}/L_{\rm Edd} = 0.2-3.6$, which has not been seen in more luminous $z > 6$ quasars. Specifically, J0859+0022 is turned out to be powered by a least massive black hole among $z > 6$ quasars known with $M_{\rm BH} = 1.7\pm0.4\times10^7 M_\odot$ due to its Seyfert-class luminosity and narrow MgII. Also, J1205-0000 also has the highest Eddington ratio of $L_{\rm bol}/L_{\rm Edd} = 3.6$ after the correction of internal reddening, which supports the scenario that the red quasars are in the transitional phase between starburst and type-I quasar. The MgII- and CIV-based $M_{\rm BH}$ are consistent within 1σ uncertainty taking into account measurement and systematic errors in the virial method.

3. Based on the obtained redshift and black hole properties, the growth history of the low-luminosity quasars is estimated assuming continuous accretion with the radiation efficiency of $\eta = 0.1$. In contrast to the seed mass arguments on the most luminous quasars at $z > 6$, the low-luminosity quasars can be explained by the Pop-III remnant black holes of $M_{\rm seed} = 10^{2-3} M_\odot$ if continuous Eddington-limit accretion is achievable. On the other hand, the current accretion rates suggest that two quasars powered by sub-Eddington accreting black holes are the remnants of the first quasars in the universe whose most active growth phase is already over at $z > 6$. They are likely on the way to settle down into the local $M_{\rm BH} - \sigma$ relation, while the luminous quasars would be the progenitors of the over-massive black hole galaxies. This scenario is partly supported by our host galaxy studies with ALMA.

4. One of the targets, J0859+0022 has weak continuum and relatively narrow emission line widths of $\mathrm{FWHM_{MgII}} = 857\pm60$ km s^{-1} and $\mathrm{FWHM_{CIV}} = 1371\pm16$ km s^{-1}. Moreover, J0859+0022 has a large equivalent width of $\mathrm{EW(Ly}\alpha + \mathrm{Nv)} = 269.5\pm0.3$Å. This quasar could be the first type-II quasar at $z > 6$; however, its blue continuum of $\alpha_\lambda = -1.60\pm0.04$ and the broad FeII components indicate its type-I nature. This intriguing quasar may be the high-redshift analogue of the local Narrow Line Seyfert I galaxies.

5. The observed Eddington ratio distribution of $z > 6$ quasars are presented dividing 37 quasars into two bins at $\log L_{\rm bol} = 47$ erg s^{-1}. The average Eddington ratio of each bin is smaller than reported in Willott et al. (2010a). We find that less-luminous quasars have larger scatter than luminous quasars, which implicates that there is a cut off in the black

hole mass function at $M_{\rm BH} \sim 10^{10} M_{\odot}$. The large scatter in the less-luminous bin suggests that there are two populations at $\log L_{\rm bol} = 46$ erg s^{-1}: One is the currently fast growing black holes with high Eddington ratios and the other is already matured $M_{\rm BH} \sim 10^{9} M_{\odot}$ black holes accreting at the similar rates as lower redshift quasars. They are the first “dead" quasars in the universe which are likely more luminous and contribute more to reionization at higher redshift.

Finally, complete $M_{\rm BH}$ measurements of a larger number of the SHELLQs quasars in some parts of the HSC-SSP coverage is required to discuss the mass and accretion rate distributions with the sample selection function is taken into account. The SHELLQs project has revealed some peculiar populations at $z > 6$ not identified in the luminous range such as narrow Lyα quasars and red quasars. The ongoing observations and future plans for the SHELLQs quasars are described in the next chapter.

Chapter 4

Conclusions and Outlook

4.1 Conclusions

In this work, we present the observational studies of $z \sim 6-7$ low-luminosity quasars based on optical wide-field surveys of the Subaru telescope. Those studies were fully made possible thanks to the Subaru's capability of deep imaging in a wide field-of-view. Specifically, this thesis work makes extensive use of the Hyper Suprime-Cam Subaru Strategic Program (HSC-SSP) survey covering more than 400 deg^2 even at this middle phase of the large program. Moreover, various ground-based 8m-class telescopes are used for quasar discovery and follow-up spectroscopy including Subaru, Gemini, and VLT.

The main results can be summarized as follows:

- **Low-luminosity quasar survey at $z \sim 6$ with Suprime-Cam:** We performed a survey for $z \sim 6$ quasars with Subaru/Suprime-Cam covering 6.5 deg^2 with deep imaging, whose 5σ limiting magnitudes in $z_{\rm R}$ band is $z_{{\rm R},3\sigma} = 24.15$. In the initial phase, 17 candidates are selected with the observed magnitudes down to $z_{\rm R} = 24.11$ based on a $i' - z_B$ and $z_B - z_R$ color selection, from which 2 quasars are spectroscopically identified at $z = 6.156$ and $z = 6.041$ with Subaru/FOCAS. As one of the new quasars has a relatively narrow Lyα as a type-I quasar with its half-line width of 427 km s^{-1}, this source could be the intermediate populations between type-I quasars and Lyα-emitting galaxies. Such ambiguous populations are also found in the HSC-SSP (Section 3.2.2), suggesting that they may be common

in the low-luminosity range at high redshift. Ten candidates remained to be identified in our first paper (Kashikawa et al., 2015). Additional follow-up spectroscopy with Subaru/FOCAS was carried out for another 4 candidates, but none of them are found to be genuine quasars. Complete identification of the 17 candidates were made possible with the deep photometry in the HSC-SSP, from which no additional quasars were found (Figure 2.2).

- **Quasar contribution to reionization:** From the two Suprime-Cam quasars, we were able to constrain the $z \sim 6$ quasar luminosity function (QLF) at the faint end ($M_{1450} \sim -23$, Figure 2.3). Parametric QLFs are obtained by combining the QLFs of this study with others at different magnitude ranges such as those from the SDSS, and fitting those with double power-laws. The best-fit QLFs suggest that the amount of ionizing photons from quasars is $\sim 1-12\%$ of the required photons for reionization within 2σ confidence levels of the QLF parameters (Figure 2.3). Various cases are assumed considering whether the ELAIS quasar is a quasar or not, and also whether a very faint AGN candidate in Parsa et al. (2017) is included (Table 2.2). Also, there are several uncertain factors in the UV photon arguments such as the minimum magnitudes of the QLFs and the clumpy factor of the IGM. However, those different models are consistent in the sense that quasars are minor contributors of the reionization even when those systematic uncertainties are taken into account. This result is contradictory to the recent arguments on the quasar-driven reionization models.

- **Near-infrared spectroscopy of $z \sim 6-7$ low-luminosity quasars:** We extend the search for $z > 6$ low-luminosity quasars with the much larger HSC-SSP. The project name is called as *Subaru High-z Exploration of Extremely Low-Luminosity Quasars* (SHELLQs). From its first-year dataset covering 430 deg^2, 33 quasars at $5.0 \leq z \leq 6.7$ have been found with the optical spectroscopy with Subaru/FOCAS and GTC/OSIRIS (Figure 3.2, Figure 3.3, Figure 3.4, Figure 3.5). Those quasars identified in the Subaru's survey account for $\sim 20\%$ of the $z > 6$ quasars currently known, and are $\sim 1-4$ magnitudes fainter than the SDSS-Main quasars ($-25 \lesssim M_{1450} \lesssim -22$, Figure 3.6).

  Deep spectra of five SHELLQs quasars were taken with Gemini/GNIRS and VLT/X-SHOOTER to study the spectral properties of the low-luminous quasars in the reionization epoch tak-

ing advantage of the wide coverage of the two spectrograph. Strong and broad emission lines of MgII, CIII], and CIV are detected over the underlying continuum, for which spectral fitting is applied to deblend their power-law continuum, FeII emission line forests, and emission lines. Although the target selection is based on redshift and absolute magnitude estimated from the optical discovery spectra, we find a few peculiar quasars with unexpected spectral properties, which would be unique in the low-luminosity range. In particular, the highest-redshift quasar in the current SHELLQs samples (J1205-0000) at $z_{\rm optical} = 6.7 - 6.9$ is the highest-redshift obscured quasar showing a curved continuum in the X-SHOOTER spectrum. Taking advantage of its rich photometric information up to the WISE 4.6μm band, the color excess is estimated to be $E(B-V) = 0.27 \pm 0.03$ assuming a typical rest-frame UV SED of a type-I quasar. For the other four quasars, the continuum slope is typical for type-I quasars. There is one quasar (J0859+0022) with narrow line widths as a type-I quasar with FWHM of $\sim$ 1000 km s^{-1}. This quasar may be a type-II quasar considering the line widths and its very weak continuum. However, we consider it to be a type-I because of its blue continuum and the presence of FeII components.

- **Black hole mass measurements:** Virial black hole masses are derived from the continuum luminosity and MgII and CIV broad emission lines to find some different trends of low-luminosity quasars from the most luminous ones. The derived black hole mass has a wide scatter of $M_{\rm BH} \sim 10^{7-9} M_{\odot}$ with the Eddington ratio of $L_{\rm bol}/L_{\rm Edd} \sim 0.1-1$, while most of the previously known $z > 6$ super massive black holes are accreting at the Eddington limit. The one red quasar has a very high Eddington ratio of $L_{\rm bol}/L_{\rm Edd} = 3.6$ based on the MgII-based black hole mass after correcting the internal reddening. The growth history of the five quasars are examined based on the obtained black hole mass and Eddington ratio, from which we find that they can be explained by light seed black holes of $M_{\rm seed} = 10^{2-3} M_{\odot}$ assuming the continuous Eddington-limit accretion. While the $z > 6$ super massive black holes are more active than at lower-redshift, we identify two quasars with sub-Eddington accretion rates, which have not seen until recently. Considering the short timescale and current relatively inefficient accretion speed, the power sources of those quasars are likely black holes which experience their rapid growth at earlier times. They more contribute to the UV photons at higher redshift. Combining $z > 6$ quasars from the literatures, we

point out for the first time that the Eddington ratio distribution has a narrow dispersion for luminous ($\log L_{\rm bol} > 47$ erg s^{-1}) $z > 6$ quasars compared to less-luminous quasars at the same redshift range. This trend suggests that there is a cut off in the $z \sim 6$ black hole mass function at $M_{\rm BH} \sim 10^{10} M_{\odot}$ and a part of the first quasars is in the post-active phase like those observed at lower redshift.

4.2 Future Prospects

Finally, our findings in this thesis pave the way for further investigations of the $z > 6$ quasars. Table X shows the list of the planned observation programs as well as our previous observations related to this thesis work.

- **The Nature of peculiar $z > 6$ quasars:** We find that there are quasars with peculiar spectral properties among the low-luminosity range. They are classified as “quasars" temporarily because their discovery optical spectra are noisy and it is hard to further examine their properties in details. First, some “quasars" have narrow Lyα with FWHM$_{\rm Ly\alpha} \sim 300$ km s^{-1}, while typical type-I quasars have FWHM$_{\rm Ly\alpha} > 1000$ km s^{-1}. They are both found in our Suprime-Cam and HSC surveys (Section 2.2 & 3.2.2). Since the fraction of this narrow Lyα quasars is not negligible to typical type-I quasars, their classification is vital for reliable estimates of the quasar luminosity function at the faint end. Their classification, which could be the composites of type-I quasars and galaxies, type-II quasars, or strong Lyα emitters such as Pop-III galaxies, should be addressed with deep near-infrared spectroscopy to see the emission line properties of various lines such as CIV, CIII], and HeII. It is possible that the type-II quasar contribution to reionization is non-negligible at the optically faint range because their intrinsic luminosity is much higher than observed in optical due to obscuration. A VLT/X-SHOOTER observation is going to be carried out for the most Lyα luminous object among the current 33 SHELLQs samples.

- **Searching for $z > 6$ quasars:** There are two directions for the highest-redshift quasar surveys. The first is to explore the much higher redshift range than the current limit. At the time of writing this thesis, the current record holder is ULAS J1342+0928 at $z = 7.5$. The

number of $z > 7.0$ quasars is still two partly because optical wide-field surveys can reach up to $z \sim 6.4$. Wide-field surveys with near-infrared telescopes such as the 6.5m TAO and WFIRST make it possible to explore up to when the first black holes begin to be formed at $z \sim 10-20$. The other way is to probe down the luminosity function. The SHELLQs project will address the faint-end of the quasar luminosity function (QLF) at $z \sim 6$ and $z \sim 7$ to investigate how rapidly the number density evolves in the first billion years of the universe. It should be noted that Prime Focus Spectrograph, the new generation fiber spectrograph of the Subaru telescope, will greatly help us to carry out follow-up observations of $z \sim 6-7$ quasar candidates over the entire HSC-SSP coverage.

- **Black home mass function:** While the early black hole growth of the less extreme populations at $z > 6$ has begun to be unveiled, the next step is to measure $M_{\rm BH}$ for a sufficient number of $z > 6$ low-luminosity quasars to give constraints to the black hole mass function (BHMF) and the Eddington ratio distribution function. Those distributions directly trace the black hole growth and can easily be compared with model predictions. The current BHMF constraints by Willott et al. (2010a) has more than an order of uncertainty at the low-mass end, which should be improved by the HSC-SSP. In particular, the $z \sim 6$ QLF of our Suprime-Cam study (Section 2.5.1) is consistent with the QLF of the CFHQS studies (Willott et al., 2010b) within the 1σ uncertainty level; however their observed distribution of the Eddington ratio at $L_{\rm bol} \sim 10^{46}$ erg s^{-1} seems to be inclined to super-Eddington compared with the HSC-SSP study in this thesis (Section 3.8.3). As simulations suggest that there is a rapid evolution in the Eddington ratio distribution at the low-Eddington ratio, it is ideal to investigate the redshift evolution of those distributions at $z \sim 4-7$ with the HSC-SSP. Four nights observations are going to be carried out in Subaru to increase the number of $M_{\rm BH}$ measured SHELLQs quasars to ~ 15. Moreover, it should be noted that $M_{\rm BH}$ measurements for the entire SHELLQs quasars are made possible by the James Webb Space Telescope (JWST), a new generation space telescope which will be launched in 2019.

Appendix A

Enhancement of Galaxy Overdensity around Quasar Pairs at $z < 3.6$ based on the Hyper Suprime-Cam Subaru Strategic Program Survey

ABSTRACT

We investigate the galaxy overdensity around proto-cluster scale quasar pairs at high ($z > 3$) and low ($z \sim 1$) redshift based on the unprecedentedly wide and deep optical survey of the Hyper Suprime-Cam Subaru Strategic Program (HSC-SSP). Using the first-year survey data covering effectively ~ 121 deg^2 with the 5σ depth of $i \sim 26.4$ and the SDSS DR12Q catalog, we find two luminous pairs at $z \sim 3.3$ and 3.6 which reside in $> 5\sigma$ overdense regions of g-dropout galaxies at $i < 25$. The projected separations of the two pairs are $R_\perp = 1.75$ and 1.04 proper Mpc, and their velocity offsets are $\Delta V = 692$ and 1448 km s^{-1}, respectively. This result is in clear contrast to the average $z \sim 4$ quasar environments as discussed in Uchiyama et al. (2017) and implies that the quasar activities of the pair members are triggered via major mergers in proto-clusters, unlike the vast majority of isolated quasars in general fields that may turn on via non-merger events such as bar and disk instabilities. At $z \sim 1$, we find 37 pairs with $R_\perp < 2$ pMpc and $\Delta V < 2300$ km s^{-1} in the current HSC-Wide coverage, including four from Hennawi et al. (2006). The distribution of the peak overdensity significance within two arcminutes around the pairs has a

long tail toward high density ($> 4\sigma$) regions. Thanks to the large sample size, we find a statistical evidence that this excess is unique to the pair environments when compared to single quasar and randomly selected galaxy environments at the same redshift range. Moreover, there are nine small-scale ($R_\perp < 1$ pMpc) pairs, two of which are found to reside in cluster fields. Our results demonstrate that < 2 pMpc-scale quasar pairs at both redshift range tend to occur in massive haloes, although perhaps not the most massive ones, and that they are useful to search for rare density peaks.

A.1 Introduction

The subject of how active galactic nuclei (AGN) connect to their surrounding galaxy formation and host dark matter haloes has been a matter of debate in modern extragalactic astronomy. When one assumes that supermassive black holes (SMBHs) grow primarily via gas accretion, the triggering mechanism of luminous quasars would be major mergers of gas-rich galaxies, which transform plenty of cold gas into the central SMBHs (e.g., Hopkins et al. (2008); Alexander & Hickox (2012)). The $M_{\rm BH} - \sigma_*$ relation (e.g., Magorrian et al. (1998); Kormendy & Ho (2013)) suggests a co-evolutionary growth history of SMBHs and host galaxies throughout the cosmic epoch in which massive galaxies host large SMBHs.

To investigate how the most mature clusters in the local universe are formed along with the hierarchal large-scale structure formation, AGN have been used for proto-cluster searches at high redshift. This is motivated by the assumption that galaxies in high density regions have earlier episodes of star formation and SMBH growth than those in normal and poor environments. Since gas-rich major mergers would more frequently happen in massive haloes than in less massive ones, luminous AGN can be used as landmarks of proto-clusters, while the blind searches of such rare density peaks requires a wide-field observation. There are various studies testing the validity of using AGN for proto-cluster searches. For example,Venemans et al. (2007) clearly show that radio galaxies are likely to be associated with proto-clusters at $z > 2$ based on their Lyα emitter (LAE) searches. Wylezalek et al. (2013) show that radio-loud AGN prefer massive environments using sources selected by the Infrared Array Camera (Fazio et al., 2004) of the *Spitzer Space Telescope*, suggesting that the high density environments induce high

spins of the SMBHs and radio jets enhancement. On the other hand, environment studies on the highest-redshift quasars show that luminous $z > 6$ quasars are not necessarily associated with rich environments (Mazzucchelli et al., 2017, and reference therein). Moreover, a deep and large spectroscopic sample of $2 < z < 3$ quasars from the Baryon Oscillation Spectroscopic Survey (BOSS, Dawson et al. (2013)) imply that the redshift evolution of the quasar auto-correlation signal gets flattened from lower redshift (Eftekharzardeh et al., 2015). Although their result is inconsistent with a $z > 3$ study by Shen et al. (2007) and the reason is unclear, it may imply that highly energetic feedback from quiescent AGN suppresses further cold-gas assembly onto the SMBHs in the most massive haloes ("radio-mode" feedback). Thereby, these arguments follow that the host halo of a luminous quasar at high redshift is not the most massive. This scenario is supported by several semi-analytical studies (e.g., Fanidakis et al. (2013); Orsi et al. (2015)).

As the HSC-SSP survey has started the enormously wide-field observation, Toshikawa et al. (2017) have found 179 promising proto-cluster candidates at $z \sim 3.8$ over 121 deg^2 currently available among the collaboration. This number overwhelms that of the previously known proto-clusters at the same redshift range, enabling them to investigate the clustering of proto-clusters for the first time. Their g-dropout catalog which efficiently selects Lyman break galaxies is used for a quasar environment study by Uchiyama et al. (2017), which is our companion paper. They exploit the catalog to examine how well quasars at $3.3 < z < 4.2$ trace the HSC proto-clusters based on their 151 BOSS quasar sample, finding that the luminous quasars in general do not reside in rich environments when compared to g-dropout galaxies. In particular, there are only six cases where the individual luminous quasars are hosted in the HSC proto-clusters within three arcminiutes (~ 1.3 proper Mpc) from the density peaks. Their result sheds a new light on the triggering mechanism of luminous quasars from an environmental point of view; the quasar activity at high redshift is more common in general environments than previously thought. One interpretation would be that the major merger is not a unique mechanism to trigger a luminous quasar and other channels, such as the secular process (bar and disk instabilities), which closes in its own system and has less to do with its environment, play a significant role. In fact, recent studies have shown that the morphology of luminous-quasar hosts at $z < 2$ are not highly distorted and not significantly different from that of inactive galaxies (e.g., Mechtley et al. (2016); Villforth et al. (2017)). Another way to explain their result is the strong

AGN feedback, which suppresses star formation in the vicinity of quasars. It is also possible that the majority of star-forming galaxies around $z \sim 4$ quasars are dusty and thus highly obscured, for which optical-based selection completeness is low.

When one assumes that major mergers dominate the role of triggering quasars in massive haloes, it is likely that environments around multiple quasars, i.e., a physical association of more than one quasar in close separation are more biased and they are much more efficient in pinpointing proto-clusters. While such populations are extremely rare, there are several studies on the pair and multiple quasars. Djorgovski et al. (1987) first report the discovery of a binary quasar at $z = 1.345$, a radio source PKS 1145-071, separated by 4.2 arcseconds. A small number of $z > 4$ quasar pairs with less than 1 pMpc projected separation has been reported (Schenider et al., 2000; Djorgovski et al., 2003; McGreer et al., 2016). Based on the SDSS, Hennawi et al. (2006) and Hennawi et al. (2010) construct large catalogs of spectroscopically confirmed quasar pairs at $z < 3$ and $3 < z < 4$, respectively. Quasar pairs with sub pMpc-scale separation like their samples are of particular interest for the study of the small-scale clustering of quasars. Several papers argue that quasar clustering is enhanced in such a small scale, which is suggestive of enhanced quasar activity in rich environments (e.g., Hennawi et al. (2006); Eftekharzadeh et al. (2017), but also see Kayo and Oguri (2012)). Regarding the environments, most of the previous studies focus on $z < 1$ pairs with ~ 10 sample sizes (e.g., Boris et al. (2007); Farina et al. (2011); Green et al. (2011); Sandrinelli et al. (2014)). While the observation depth and the target selection differ among these studies, they all suggest that the extremely rare quasar pairs are not always associated with significant overdensity of galaxies. At high-redshift, Fukugita et al. (2004) look for the overdensity enhancement around a $z = 4.25$ quasar pair, SDSS J1439-0034, but see no significant difference from a general field within a 5.8 arcminutes^2 area. On the other hand, it is remarkable that Hennawi et al. (2015) show an exceptionally strong enhancement of the LAE surface density around a $z = 2$ quasar quartet ("Jackpot nebulae"), with more than an order of excess on < 100 pkpc scale, demonstrating the extremeness of multiple quasar environments. Moreover, Cai et al. (2017) find an extremely massive overdensity of LAEs at $z = 2.32$ which is associated with multiple quasars.

This paper focuses on the galaxy overdensity around pairs of the BOSS quasars up to $z \sim 3.6$, thanks to the unprecedented coverage and depth of the HSC-SSP dataset. The outline of this

paper is as follows: In Section A.2, we describe our quasar pair sample at high redshift ($3.3 < z < 4.2$) and introduce how we select surrounding galaxies using the HSC-SSP photometric dataset. In Section A.3, we show that two quasar pairs at $z \sim 3.3$ and ~ 3.6 are both associated with the HSC proto-clusters, supporting that the rare occurrence of < 2 pMpc-scale pairs traces rich environments. Section A.4 describes our overdensity measurements around 37 quasar pairs at $z < 1.5$ including four pairs from literature, using the photometric redshift catalog of the HSC-SSP. We find statistical evidence that a significantly higher fraction of quasar pairs resides in dense environments than single quasars and randomly selected galaxies, which is described in Section A.5. We discuss the quasar pair environments in Section A.6, especially comparing with the study of single quasar environments at $z \sim 3.8$ (Uchiyama et al., 2017). Finally, the summary is given in Section A.7.

The magnitudes cited in this chapter are the CModel magnitude (in AB system), which is derived by fitting images with combination of the exponential and de Vaucouleurs profiles. The CModel magnitude is conceptionally the same as the PSF magnitude for point sources.

A.2 Data and Sample Selection

A.2.1 Effective Region in the HSC-Wide Dataset

In this paper, we use a photometric catalog of the HSC-SSP Wide survey for our surrounding galaxy selection. The photometric catalog using a dedicated pipeline (hscPipe; Bosch et al. (2017)) has been opened to the collaboration, the latest dataset of which is denoted as DR S16A with its Wide component covering ~ 170 deg^2 in five broad-band filters ($grizy$). This area consists of several large fields along the equator (W-GAMA09H, W-Wide12H, W-GAMA15H, W-VVDS, W-XMMLSS) and one field at Decl.= 43 deg (W-HECTMAP). The average 5σ-limiting magnitudes[1] are as follows: $g \sim 26.8$, $r \sim 26.4$, $i \sim 26.4$, $z \sim 25.5$, and $y \sim 24.7$. We share the g-dropout catalog of the HSC proto-cluster search project (Toshikawa et al., 2017). To take into account the partly inhomogeneous imaging in each HSC filter over the large survey regions, they carefully remove area with shallow depths in either g-, r-, or i-bands based on sky noise

[1] this limiting magnitude is defined as the point where the PSF magnitude has $S/N \sim 5\sigma$ at $0.5-0.7$ arcsec seeing condition. See Aihara et al. (2017a)

measurements at each 12×12 arcmin^2 sub-regions (*"patch"* in the HSC-SSP term), as well as the masked regions, for example, around saturated stars, at the edge of the images, and on bad pixels based on the photometry flags of the hscPipe (see Section 2 of Toshikawa et al. (2017) for more details). As a result, they construct a highly clean and uniform g-dropout galaxy sample over a total effective area of ~ 121 deg^2. Specifically, W-GAMA09H field is discarded in our analysis, because the number counts of the g-dropout galaxies has an offset compared to the other fields at bright magnitude range due to its shallow depth in r-band.

A.2.2 Quasar pair sample at $3 < z < 4$

In this section, we present our selection and sample of quasar pairs at $3 < z < 4$. We use the latest catalog of spectroscopically confirmed quasars from the SDSS-III BOSS survey (DR12Q, Pâris et al. (2017)), which contains about 300 thousands quasars in 9376 deg^2 down to $g = 22.0$ or $r = 21.85$. While the BOSS survey originally targets quasars at $2.15 \leq z \leq 3.5$, the redshift distribution of the DR12Q sample has a wide skirt up to $z \sim 6.4$. Moreover, the DR12Q catalog has a secondary redshift peak at $z \sim 0.8$, which is due to the SDSS-color similarity of quasars at this redshift range to that of $2 < z < 3$ quasars, enabling us to also investigate low-redshift quasar environments as described in Section A.4. We require secure redshift determination using a flag given in the DR12Q catalog (i.e., `ZWARNING=0`).

Since we assume such a situation in which more than one quasar emerges in the same massive halo, we define quasar pairs as two quasars with their separation closer than the size of massive proto-clusters. We extract quasar pairs from the DR12Q catalog following a framework given by a simulation done by Chiang et al. (2013). According to their definition of the most massive proto-clusters, which are the progenitors of $M_{\mathrm{halo,z=0}} > 10^{15} M_\odot$ clusters, and their characteristic size at the concerned redshift, we extract quasar pairs with their projected proper distance of $R_\perp < 4$ pMpc and velocity offset of $\Delta V < 3000$ km s^{-1}. This definition is more relaxed than previous studies such as Hennawi et al. (2010), since they assume that the pairs are gravitationally bound systems with $R_\perp < 1$ pMpc. The redshift range is limited to $3.3 < z < 4.2$ where the selection completeness of the HSC g-dropouts is over 0.4 (Ono et al., 2017). The Lyman break of galaxies at this range is shifted to r-band, and therefore $g - r$ and $r - i$ colors can be used to distinguish those galaxies from contaminants such as main-sequence stars and $z < 1$ galaxies. The

velocity offset between the quasar members in a pair ΔV is determined from the SDSS's visually inspected redshifts (Z_VI). Considering the uncertainty of the BOSS redshifts primarily relying on the Lyman break and Lyα emission ($\sim$ 1000 km s^{-1}), possible peculiar motion between the pair members ($\sim$ 500 km s^{-1}), and also their physical separation in the radial direction, we apply $\Delta V_{\rm max}$ = 3000 km s^{-1} as the maximum velocity offset of the $z \sim 3.8$ pairs. Finally, the BOSS quasar spectra are visually checked to confirm their secure classification and redshift determination.

As a result, two pairs of quasars are found at $z \sim 3.6$ and $z \sim 3.3$ from the DR12Q catalog. Table A.1 lists the two pairs with their angular separation $\Delta\theta$, projected separation $R_\perp$ and velocity offset ΔV, in which the average redshift of the two quasars in pairs is regarded as a pair redshift. QSOP1 is a pair of quasars at $z = 3.585$ and $z = 3.574$ with their angular separation $\Delta\theta = 241$ arcseconds ($R_\perp = 1.75$ pMpc) and velocity offset of $\Delta V = 692$ km s^{-1}. QSOP2 is a quasar pair at $z = 3.330$ and $z = 3.309$, which is close to the edge of our redshift cut, with their angular separation $\Delta\theta = 139$ arcseconds ($R_\perp = 1.04$ pMpc) and velocity offset of $\Delta V = 692$ km s^{-1}. Note that only Fukugita et al. (2004) has investigated the overdensity around $z > 3$ quasar pairs before this study. We search for their radio counterparts in the Faint Images of the Radio Sky at Twenty cm survey (FIRST 14Dec17 version; Becker et al. (1995)) within 30 arcsecond radius, but find that none of them are detected. There are $\sim$ 30 pairs in the whole HSC-Wide coverage (i.e., 1400 deg^2). The complete analysis of these pair environments will be done after the HSC-SSP survey is completed. Note that our pair selection is incomplete for small-scale pairs due to the fiber collision limit of the BOSS survey ($\Delta\theta = 62$ arcseconds). We check whether high-redshift physical pairs previously identified in the literature (i.e., Schenider et al. (2000); Hennawi et al. (2010)) are covered in DR S16A, but find no suitable pairs in our redshift range. There are several already-known pairs in the entire HSC-SSP survey regions, as we describe in Section A.6.1.

A.2.3 Imaging data and method

The g-dropout selection in this paper is the same as Toshikawa et al. (2017). We first apply a magnitude cut of $i < 25$ ($= i_{\rm lim,5\sigma} - 1.4$) to measure the overdensity in a magnitude range satisfying high completeness. Since this threshold corresponds to $\sim M^* + 2$ at $z \sim 4$ (Bouwens et al., 2007) where M^* denotes the characteristic magnitude, our density measurements are limited to

the bright population. In addition, we require significant detection in r- ($< r_{\mathrm{lim},3\sigma}$) and i-bands ($< i_{\mathrm{lim},5\sigma}$) to remove contaminants such as artificial and moving objects. It is noted that the broad-band selection of Lyman break galaxies has a large uncertainty on their redshifts, corresponding to ~ 200 pMpc in the line-of-sight direction, which is much larger than the projection direction. Then, the following color cuts are applied.

If $g < g_{\mathrm{lim},3\sigma}$,

$$1.0 < g - r \tag{A.1}$$

$$-1.0 < r - i < 1.0 \tag{A.2}$$

$$1.5(r-i) < (g-r) - 0.8 \tag{A.3}$$

, and if $g \geq g_{\mathrm{lim},3\sigma}$,

$$1.0 < g_{\mathrm{lim},3\sigma} - r \tag{A.4}$$

$$-1.0 < r - i < 1.0 \tag{A.5}$$

$$1.5(r-i) < (g_{\mathrm{lim},3\sigma} - r) - 0.8. \tag{A.6}$$

Note that the observed magnitudes are corrected for the Galactic extinction. Furthermore, we require that each source is de-blended with others (`deblend_nchild=0`) and passes various photometric quality flags of the HSC-SSP [2].

Our overdensity measurements of g-dropout galaxies in the quasar pair fields are as follows. First, we extract g-dropout galaxies within 2×2 deg^2 field centered on the pair in the projection plane. Then, we set a square grid on the field at 0.6 arcminute intervals to measure the number count of g-dropouts at each position within a 1.8-arcminutes aperture, corresponding to the size of a typical proto-cluster at $z \sim 4$ (0.75 pMpc). We calculate the average and standard deviation of the g-dropout counts over the effective region (see Section A.2.1) inside the 2×2 deg^2 fields. Blank grids where no galaxies exist inside the aperture are also masked out. The total area

[2] Specifically, we use the following flags: `centroid_sdss_flags,flags_pixel_edge,flags_pixel_interpolated_center,flags_pixel_saturated_center,flags_pixel_cr_center,flags_pixel_bad,flags_pixel_suspect_center,cmodel_flux_flags`

effectively used in 2×2 deg^2 is 2.44 deg^2 for QSOP1 and 2.19 deg^2 for QSOP2, which are large enough to calculate the field number counts. After deriving the significance map over the wide area, we zoom in on the pair vicinity of 12×12 arcmin^2 ($\sim 5 \times 5$ pMpc^2) to see its local overdensity significance. The arbitrary zoom-in scale is chosen to be larger than the pair separation and thus enough to see the overdensity structure in the quasar pair fields.

A.3 Result I: $z > 3$ Quasar Pair Environments

A.3.1 Discovery of proto-clusters at $z = 3.3$ & 3.6

This section shows the result of the overdensity measurements for the two quasar pair fields at $z > 3$. We find significant overdensity in both pair fields with the peak significance $\sigma_{\rm peak} = 5.22\sigma$ and 5.01σ, which is summarized in Table A.2. Figure A.1 shows the overdensity profile of the pair fields where the color contours indicate the g-dropout overdensity significance based on the g-dropout counts. The pair members are shown in stars and g-dropout galaxies are shown in circles. QSOP1 field shows a filament-like structure in the westward direction and QSOP2 field shows a core-like structure with several smaller density peaks in the vicinity. The four quasars themselves are not selected in our dropout selection due to their relatively blue $g-r$ colors ($0.3 \leq g-r \leq 0.9$), which could be explained by the intrinsic power-law shape of the quasar continuum declining toward longer wavelength. The cumulative number counts of the g-dropouts within five arcminutes from the pair centers are shown in Figure A.2 with open symbols, compared with those of the 2×2 deg^2 general fields used for the density measurements [3]. Overall, the number counts are roughly twice as high in all (non-zero) magnitude bins even within such a large projected area corresponding to ~ 2 pMpc radius. Specifically, there are two bright dropouts at $21.2 < i < 21.4$ in the QSOP1 field, which is six times higher density than the general fields. Although the redshift uncertainty in our dropout selection is large, our result strongly suggests that these pairs are associated with massive environments, namely proto-clusters.

Indeed, QSOP1 and QSOP2 fields are part of the HSC proto-clusters cataloged in Toshikawa et al. (2017). The two fields also have high sigma peaks over 4σ in their measurements (4.8σ and 4.0σ, respectively), which are likely to evolve in massive clusters in the local universe with the

[3] The pair vicinity is excluded in the calculation of the field number counts.

descendant halo mass $M_{\rm halo,z=0} > 10^{14} M_\odot$. It is notable that these two fields are not the richest among their HSC proto-clusters, which could suggest that even quasar pairs do not trace the most massive haloes. The reason the significance in our measurements is slightly higher than their measurements is the difference of the area used for the significance measurements. In Toshikawa et al. (2017), they measure the average and standard deviation of g-dropout counts over the whole S16A HSC-Wide area, deriving the average $N_{\rm ave,Wide} = 6.39 \pm 3.24$. Meanwhile, we measure the same quantities in an area approximately corresponding to the HSC field-of-view around the pairs. Therefore, their overdensity measurements reflect not only intrinsic galaxy density distribution but also different completeness over the large area due to different observation depth taken in various seeing conditions and different times of being covered while dithering. Indeed, the peak significance of the two pair fields is smaller in our measurements, and both fields, especially QSOP2 at the edge of the W-HECTMAP, have smaller $N_{\rm ave}$ than their measurements.

For the two proto-clusters, we find that local peaks are close to one of the pair members, but not to the other one (see Table A.1). For QSOP1, the significance just above the two quasars are not high and, in particular, HSCJ221452+011119 (the upper one in Figure A.1) is at the outskirt of the overdensity profile. This is also the case for QSOP2, as HSCJ161451+423737 (the upper one) is at the gap of density peaks. Nevertheless, there are only six out of 151 quasars in Uchiyama et al. (2017) measurements with which $> 4\sigma$ overdensity regions are associated within three arcminutes from the HSC proto-clusters, and intriguingly, three of them are the quasar pairs: the two QSOP1 quasars and one QSOP2 quasar (HSCJ161447+423525). Therefore, our result may indicate that pairs of quasars are likely related to rich environments, but they do not emerge at the central peak of galaxy density.

To further investigate the overdensity structure, the overdensity profiles of the same two fields are measured again including fainter g-dropouts down to the approximate 5σ limiting magnitude. Figure A.3 shows the local significance maps of g-dropouts down to $i < 26$ ($\sim i_{{\rm lim},5\sigma}$), for which only the i-band magnitude cut is loosened by one magnitude in the original dropout selection criteria. The circles and stars are the same as Figure A.1 and the black dots show the g-dropouts with $25 \leq i < 26$. In the two significance maps, the overdensity structures become more extended and centered around the pairs in Figure A.3. While the completeness falls down

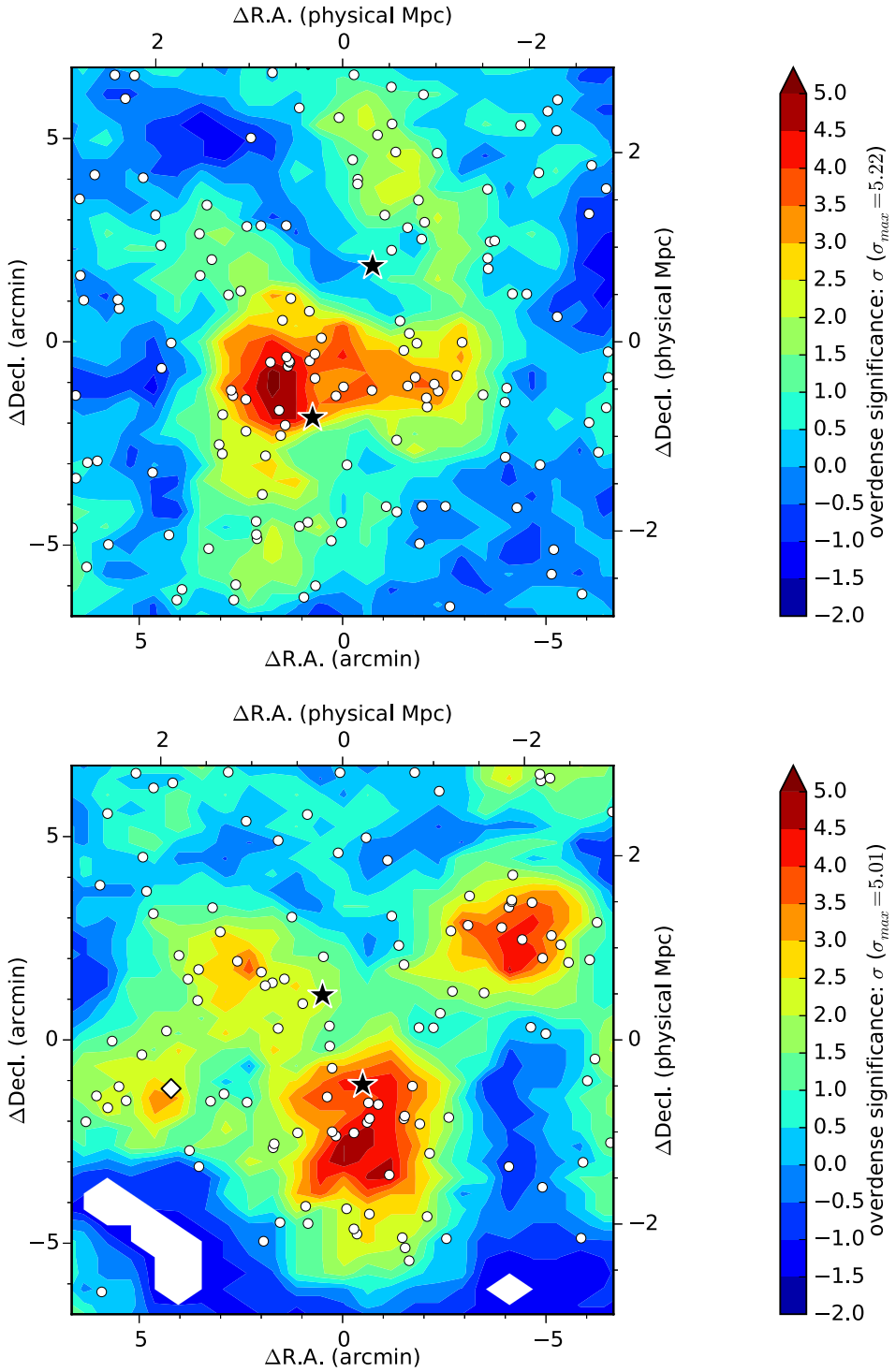

Figure A.1: Overdensity profile of g-dropout galaxies (12×12 arcminutes^2) around QSOP1 (top) and QSOP2 (bottom). The quasar pairs are shown in black stars. The surrounding g-dropouts are shown in white circles. The g-dropout overdensity significance is shown in color contours. The region where no galaxies are found is masked. A white diamond in the QSOP2 field shows the quasar candidate, HSCJ161506+423519 ($i = 22.30$). The physical scale from the pair center is also indicated.

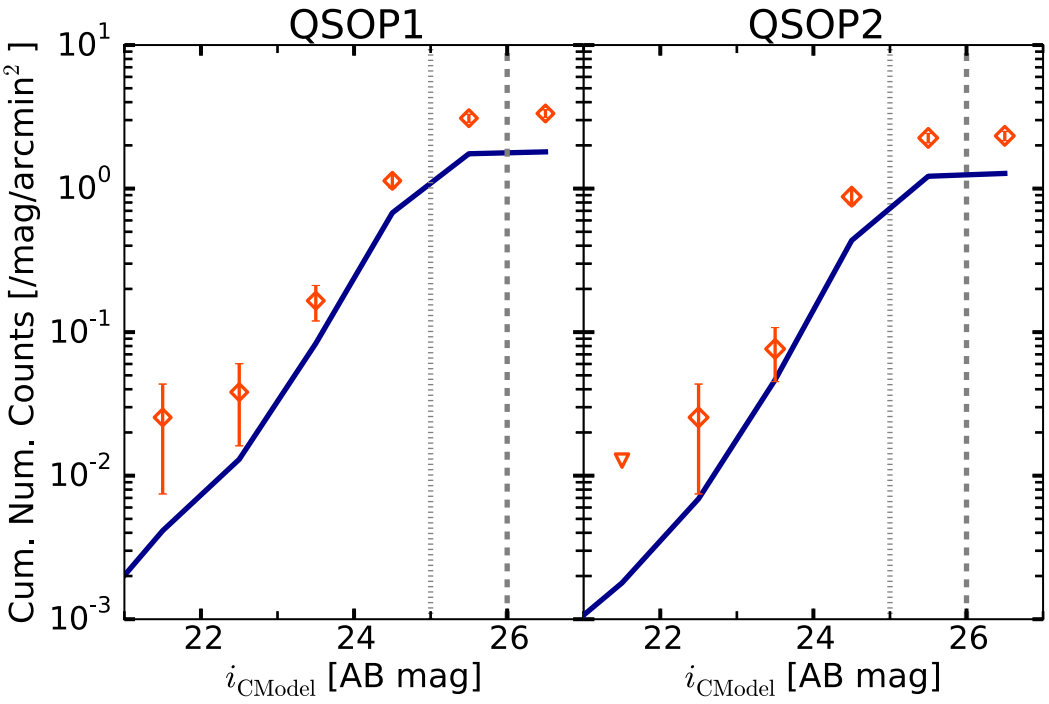

Figure A.2: Cumulative i-band number counts of the g-dropouts within five arcminutes from the pair centers (left: QSOP1, right: QSOP2). In each panel, the open symbols show those of the pair field with Poisson error bars. Magnitude bins with zero source count are shown in upside-down triangles. The solid line shows the number counts of the field where the pair vicinity is excluded. The $i = 25$ and $i = 26$ magnitude thresholds are shown in vertical dotted and dashed lines, respectively.

from $i > 25$ as is also indicated in Figure A.2, the profiles would trace real structures assuming that the completeness is independent of local positions. Therefore, we conclude that these proto-clusters have filament-like extended structure and likely host the luminous quasars pairs inside. We discuss the interpretation of our results in Section A.6.1 comparing with single quasar environments.

A.3.2 A faint quasar candidate in the pair fields

We inspect the possibility that the two proto-clusters we find host other quasars fainter than the BOSS depth limit. Here, we assume a pure point source morphology and search for faint quasar candidates among the g-dropouts in the two pair fields. For this purpose, a shape parameter included in the HSC-SSP dataset is used, which gives a rough shape measurement based on the second moment of the object image. We take the i-band shape parameter, since the i-band observation in the HSC-SSP is executed in good seeing conditions (typically 0.56 arcsecond). Using the ratio of the g-dropout moment (`ishape_sdss`, I_{ij}) over the PSF moment (`ishape_sdss_psf`, ψ_{ij}), Akiyama et al. (2017) show that, through their $z \sim 4$ quasar selection, $i < 23$ point sources are extracted with $> 80\%$ completeness using their criteria: $I_{xx}/\psi_{xx} < 1.1 \wedge I_{yy}/\psi_{yy} < 1.1$. We apply the same criteria for our g-dropouts down to $i < 23$ in the QSOP1 and QSOP2 fields. Among five g-dropouts with $i < 23$ in the QSOP1 and two in QSOP2, we find that the brightest dropout in the QSOP2 field, HSCJ161506+423519 ($i = 22.30$) is a point source with its shape parameters $I_{xx}/\psi_{xx} = 1.00$ and $I_{yy}/\psi_{yy} = 1.01$, as is also shown in Table A.3. This quasar candidate is shown in a diamond in Figure A.1 and A.3. This source is ~ 2 pMpc away from the two QSOP2 quasars, and at the center of a small density peak. Therefore, it is likely that three QSOP2 quasars cluster in 2 pMpc scale, embedded in a large proto-cluster at $z \sim 3.3$, while the faint quasar candidate could be a foreground or background quasar independent of the pair fields. We search for the radio counterpart of this quasar candidate with the FIRST survey, but do not find any source within 30 arcsecond from the optical position.

Table A.1: Quasar pair sample at $3 < z < 4$

ID[a]	R.A.[b] (J2000)	Decl.[c] (J2000)	redshift[d]	i[e] [mag]	$\Delta\theta$[f] [arcsec]	$R_\perp$[g] [pMpc]	ΔV[h] [km s^{-1}]
QSOP1	22:14:52:49	+01:11:19.9	3.585	21.167 ± 0.002	240.6	1.75	692
	22:14:58.38	+01:07:36.1	3.574	20.380 ± 0.001			
QSOP2	16:14:47.39	+42:35:25.2	3.330	20.373 ± 0.001	139.0	1.04	1448
	16:14:51.35	+42:37:37.2	3.309	20.092 ± 0.001			

[a] Pair ID. [b,c] HSC coordinates. [d] SDSS DR12Q visual redshift (`Z_VI`). [e] Extinction-corrected HSC-i magnitude. [f] Angular separation in arcseconds. [g] Projected separation in physical scale. [h] Velocity offset of the pairs in km s^{-1}.

Table A.2: Overdensity significance around two $z > 3$ quasar pairs based on $i < 25$ g-dropouts

ID	$\sigma^a_{\rm peak}$	$\sigma^b_{\rm Q1}$	$\sigma^c_{\rm Q2}$	$(N_{\rm ave} \pm \sigma_{\rm STD})^d$
QSOP1	5.22	-0.02	3.30	5.80 ±2.91
QSOP2	5.01	4.21	2.23	4.40 ±2.52

[a] Overdensity significance.
[b,c] Significance above each quasar. The former and latter quasars in Table A.1 are denoted as Q1 and Q2, respectively.
[d] Average number and standard deviation ($= \sigma_{\rm STD}$) of g-dropouts within a 1.8′-radius aperture.

Table A.3: The quasar candidate at $z \sim 3.3$ associated with the QSOP2: HSCJ161506+423519

R.A. (J2000)	Decl. (J2000)	g [mag]	r [mag]	i [mag]	z [mag]	y [mag]	I^*_{xx} [arcsec^2]	I^*_{yy} [arcsec^2]	$(I_{xx}/\psi_{xx})^\dagger$	$(I_{yy}/\psi_{yy})^\dagger$
16:15:06.24	+42:35:19.4	24.414 ± 0.033	22.732 ± 0.008	22.272 ± 0.005	22.123 ± 0.012	22.076 ± 0.025	0.0442	0.0426	1.00	1.01

The HSC magnitudes are extinction-corrected. [*] The practical adaptive momentum of the object. [†] ratio of the object momentum over that of the PSF model: I/ψ. Note that point sources can be extracted with > 80% completeness down to $i = 23$ with $(I_{xx}/\psi_{xx}) < 1.1 \wedge (I_{yy}/\psi_{yy}) < 1.1$ (see Section 2.2 of Akiyama et al. (2017)).

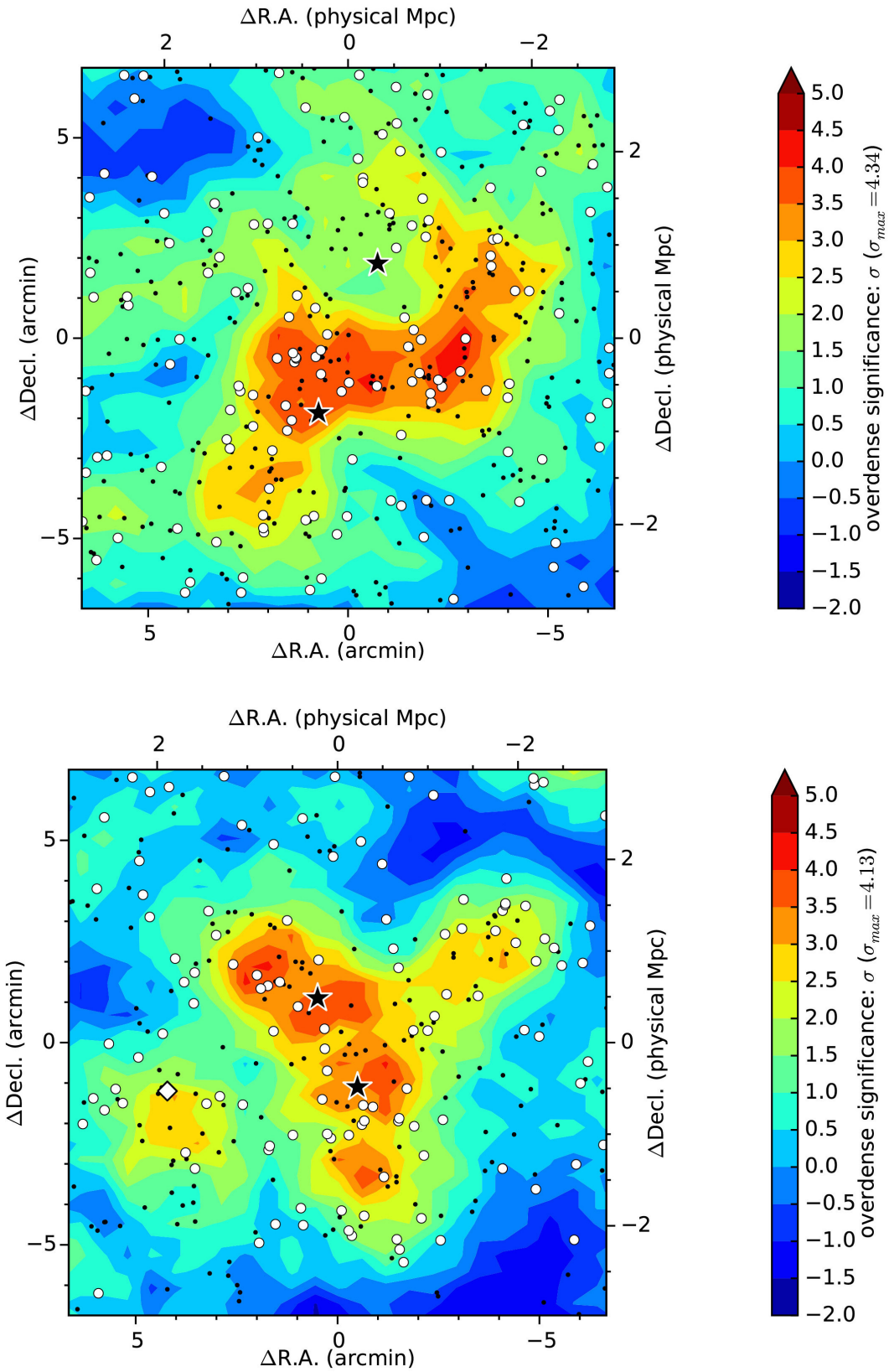

Figure A.3: The same significance maps for QSOP1 and QSOP2, but with fainter g-dropouts down to $i = 26.0$. The black dots show the faint ($25 \leq i < 26$) dropouts. The overdensity significance are measured with all $i < 26.0$ dropouts.

A.4 Quasar Pairs at $z \sim 1$

In the previous sections, we report that two quasar pairs at high redshift do trace proto-clusters. On the other hand, previous studies show that quasar pairs at low redshift ($z < 1$) do not always reside in dense environments. A recent study by Song et al. (2016) shows that $z \sim 1$ single quasar environments have a slight tendency toward high density regions, while the enhancement of the quasar density is weaker than expected from a proportional relation of the galaxy density. From this section, we extend the redshift range down to $z \sim 1$ to compare with the high-redshift pairs and also with single quasars at the same redshift.

A.4.1 $z \sim 1$ quasar pair selection

BOSS pairs

We extract our sample of low-redshift quasar pairs from the SDSS DR12Q catalog as follows. First, the selection area is limited to the ~ 121 deg^2 of the S16A effective area. Second, we limit the redshift range to $z < 1.5$, over which the photometric redshift estimate with the five-band photometry of the HSC has a large scatter and a high contamination rate (Tanaka et al., 2017). After applying the BOSS redshift flag (`ZWARNING=0`), we apply our definition of $z \sim 1$ quasar pairs: two quasars within projected separation $R_\perp < 2$ ($= 1.4\ h^{-1}$) pMpc and velocity offset $\Delta V < 2300$ km s^{-1}. The maximum projected separation corresponds to the size of a $z \sim 1$ proto-cluster, the descendant halo mass of which is $M_{\mathrm{halo},z=0} \sim 10^{14} M_\odot$ (Chiang et al., 2013). It is chosen to select pairs with comparable separation to the two $z > 3$ pairs in this paper. The maximum velocity difference takes into account redshift uncertainty, peculiar velocity, and physical separation of < 2 pMpc. At this stage, we select 38 pairs. We further require that the following positions and areas are within the S16A effective area to exclude insufficient fields for the overdensity measurements: i) at the position of the quasars, ii) at the pair center, iii) over 70% of the 2×2 deg^2 area centered on the pair, and iv) over 80% of the pair vicinity (8×8 arcmin^2). Finally, 33 pairs at $0.33 < z < 1.49$ ($z \sim 1.02$ on average) are extracted in the S16A area. Their redshift distribution is shown in Figure A.4. We find that J020332.82-050944.5 at $z = 1.353$ is double-counted, having two companions nearby. Since the projection separation of the two companions are over the cluster scale (i.e., > 2 pMpc), we treat the two pairs individually in the following analysis. It is

noted that whether these three quasars are considered as two pairs or a triplet does not affect our final result in Section A.5. In the search of $0.5 < z < 3$ small-scale quasar pairs with the SDSS (Hennawi et al., 2006), two quasars with $R_\perp < 1\ h^{-1}$ pMpc and $\Delta V < 2000$ km s^{-1} separation are assumed to be physically associated binaries. On the other hand, this study loosens the pair selection criteria as we recognize a cluster-scale association of two quasars as a pair. While we have four small-scale ($R_\perp < 1$ pMpc) pairs from the BOSS catalog, it should be noted that our selection is not complete, since a complete search of such sub pMpc-scale pairs requires a dedicated spectroscopic campaign. The detailed information of the pairs such as their coordinates, redshift, and pair separation are given in Table A.4. Note that all $z \sim 1$ pairs are in the W-XMMLSS region. We find that most of them are flagged as the BOSS ancillary program targets (`ANCIALLY_TARGET2`).

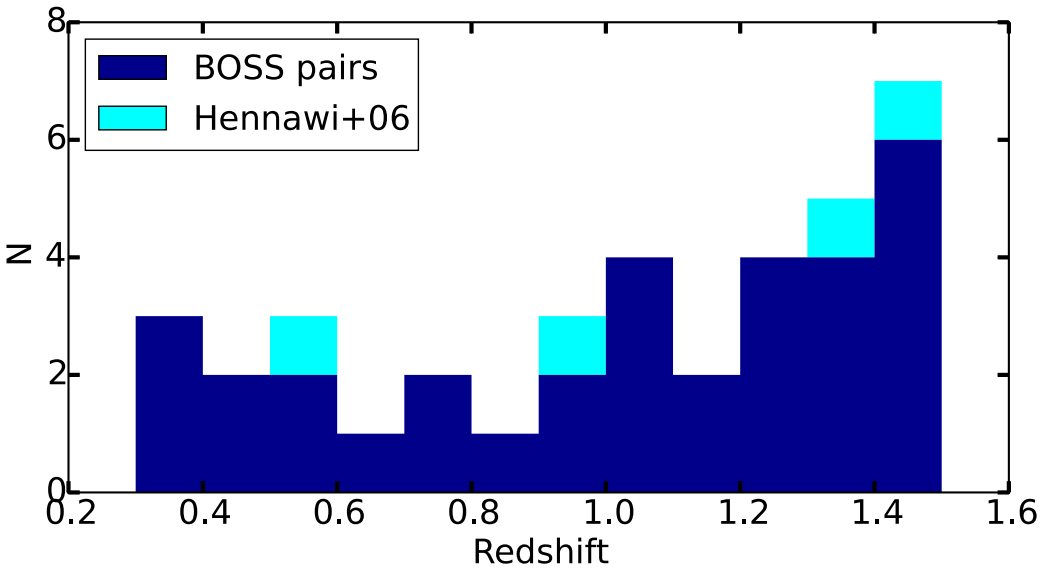

Figure A.4: Redshift distribution of the $z < 1.5$ pairs. 33 BOSS quasar pairs ($R_\perp < 2$ pMpc and $\Delta V < 2300$ km s^{-1}) is shown in dark blue. The four pairs from Hennawi et al. (2006) are shown in cyan (Sec. A.4.1). The pair coordinates, redshift, separation are summarized in Table A.5.

Table A.4: Quasar pairs at $z \sim 1$ extracted from the BOSS DR12Q with their overdensity significance within 2 arcminutes

ID[a]	redshift[b]	i^c [mag]	$\Delta\theta$ [arcsec]	$R_\perp$ [pMpc]	ΔV [km s^{-1}]	$\sigma^d_{\mathrm{peak},2'}$
SDSSJ020257.39-051225.4	0.512	21.13 ± 0.09	251.3	1.55	504	2.08
SDSSJ020313.15-051057.6	0.514	21.30 ± 0.10				
SDSSJ020320.47-050933.8	1.3526	21.18 ± 0.09	184.7	1.55	40	1.79
SDSSJ020332.82-050944.5*	1.3529	21.10 ± 0.09				
SDSSJ020332.82-050944.5*	1.3529	21.10 ± 0.09	182.7	1.54	1057	5.18
SDSSJ020341.74-050739.5	1.345	19.69 ± 0.05				
SDSSJ020334.58-051721.3†	1.399	21.30 ± 0.11	99.9	0.84	130	1.62
SDSSJ020336.45-051545.4†	1.400	20.42 ± 0.02				
SDSSJ020411.47-051032.7	0.326	19.86 ± 0.04	314.3	1.49	1261	1.39
SDSSJ020423.94-050619.6	0.332	19.74 ± 0.03				
SDSSJ020442.23-051041.3	1.329	20.90 ± 0.07	117.5	0.99	374	0.92
SDSSJ020448.12-050923.4	1.326	22.77 ± 0.32				
SDSSJ020645.57-044511.8	1.410	19.53 ± 0.07	226.6	1.91	2262	4.57
SDSSJ020700.09-044406.8	1.428	20.72 ± 0.08				
SDSSJ020659.51-042343.3	0.732	21.21 ± 0.08	173.0	1.26	587	2.94
SDSSJ020709.83-042501.5	0.729	21.32 ± 0.08				
SDSSJ021105.40-051424.0†	1.078	21.37 ± 0.08	37.0	0.30	680	4.56
SDSSJ021107.88-051425.6†	1.083	20.04 ± 0.04				
SDSSJ021335.21-055002.7	1.2219	18.86 ± 0.02	173.4	1.44	18	2.41
SDSSJ021339.82-055241.9	1.2220	20.56 ± 0.05				
SDSSJ021425.44-035631.7	1.423	20.63 ± 0.05	137.5	1.16	356	1.12
SDSSJ021434.30-035555.3	1.426	20.88 ± 0.05				
SDSSJ021436.80-045150.4	1.107	20.60 ± 0.21	156.6	1.28	1091	1.34
SDSSJ021444.98-045012.6	1.115	21.50 ± 0.10				

ID[a]	redshift[b]	i^c [mag]	$\Delta\theta$ [arcsec]	$R_\perp$ [pMpc]	ΔV [km s^{-1}]	$\sigma^d_{\mathrm{peak},2'}$
SDSSJ021448.84-040601.7	0.4447	20.22 ± 0.04	293.4	1.68	74	1.83
SDSSJ021508.19-040513.6	0.4451	20.07 ± 0.03				
SDSSJ021606.59-040508.4	1.1447	20.19 ± 0.13	147.3	1.21	26	-0.11
SDSSJ021614.95-040626.3	1.1449	21.40 ± 0.08				
SDSSJ021610.64-045229.8	0.9570	21.35 ± 0.07	240.7	1.91	28	3.43
SDSSJ021626.53-045308.3	0.9568	21.17 ± 0.07				
SDSSJ021650.21-040142.6	1.031	20.96 ± 0.06	218.3	1.76	154	2.85
SDSSJ021659.43-035853.4	1.030	21.77 ± 0.11				
SDSSJ021710.20-034101.2	1.425	20.85 ± 0.07	178.1	1.50	296	1.37
SDSSJ021718.77-033857.6	1.427	21.59 ± 0.13				
SDSSJ021756.83-035316.6	0.7511	20.53 ± 0.04	231.2	1.70	92	4.20
SDSSJ021806.76-035019.5	0.7505	21.72 ± 0.13				
SDSSJ021757.23-050216.3	1.088	20.47 ± 0.04	237.0	1.93	1081	6.46
SDSSJ021809.48-045945.8	1.095	21.60 ± 0.10				
SDSSJ021809.55-050200.3	1.277	21.22 ± 0.07	128.3	1.07	1290	3.96
SDSSJ021817.20-050258.7	1.287	20.26 ± 0.04				
SDSSJ022024.49-040017.2	0.812	21.58 ± 0.11	228.2	1.72	1723	0.75
SDSSJ022032.41-040332.2	0.822	20.77 ± 0.06				
SDSSJ022125.05-055638.0[†]	0.585	20.59 ± 0.04	150.4	0.99	893	2.98
SDSSJ022128.77-055857.7[†]	0.580	19.81 ± 0.02				
SDSSJ022226.84-041313.4	1.486	21.73 ± 0.11	189.7	1.60	1193	1.73
SDSSJ022237.88-041140.3	1.496	21.52 ± 0.09				
SDSSJ022248.98-044824.6	1.419	20.81 ± 0.06	200.7	1.69	263	1.97
SDSSJ022253.17-044513.9	1.421	21.17 ± 0.09				
SDSSJ022534.82-042401.6	0.920	21.06 ± 0.08	152.8	1.20	222	5.90
SDSSJ022537.16-042132.9	0.921	19.32 ± 0.03				
SDSSJ022542.41-051452.4	1.258	21.35 ± 0.11	194.8	1.63	281	1.82
SDSSJ022554.86-051354.6	1.256	20.08 ± 0.04				

ID[a]	redshift[b]	i^c [mag]	$\Delta\theta$ [arcsec]	$R_\perp$ [pMpc]	ΔV [km s^{-1}]	$\sigma^d_{\mathrm{peak},2'}$
SDSSJ022550.97-040247.4	1.448	21.14 ± 0.08	150.1	1.27	799	2.25
SDSSJ022552.15-040516.5	1.441	21.30 ± 0.08				
SDSSJ022855.35-051130.6	0.366	18.97 ± 0.05	200.5	1.02	96	0.78
SDSSJ022855.95-051450.8	0.365	19.96 ± 0.06				
SDSSJ022916.82-044600.7	0.612	20.35 ± 0.04	193.9	1.31	455	1.60
SDSSJ022928.73-044444.0	0.610	20.53 ± 0.05				
SDSSJ023035.82-052603.2†	0.364	19.68 ± 0.03	153.2	0.78	318	1.84
SDSSJ023038.66-052336.0†	0.363	19.96 ± 0.03				
SDSSJ023231.43-053655.9	1.098	20.92 ± 0.07	165.5	1.35	408	3.18
SDSSJ023238.46-053903.9	1.101	21.01 ± 0.07				
SDSSJ023323.39-042803.0	1.238	21.41 ± 0.08	118.1	0.98	362	2.42
SDSSJ023331.24-042815.2	1.241	20.76 ± 0.06				
SDSSJ023328.44-054604.4†	0.494	20.31 ± 0.03	41.1	0.25	170	2.46
SDSSJ023331.05-054550.9†	0.493	18.45 ± 0.02				

Notes: [a] DR12Q ID. [b] DR12Q redshift (`Z_VI`). [c] SDSS-*i* PSF magnitude. [d] Peak significance within two arcminutes around the pairs.

* The quasar having two companions. † Small-scale pairs with $R_\perp < 1$ pMpc.

Pairs in the literature

To complement the sub pMpc-scale quasar pairs lacking in the BOSS pair selection, spectroscopically confirmed small-scale pairs identified in the literature are added to our sample. Such pairs are usually identified as byproducts of lensed quasar searches. We look for spectroscopically confirmed binary quasars within the DR S16A coverage referring to the following literature: Djorgovski (1991); Myers et al. (2008); Hennawi et al. (2006); Kayo and Oguri (2012); Inada et al. (2012); More et al. (2016); Eftekharzadeh et al. (2017). Following the same selection procedure applied to the BOSS quasars, we are able to measure the galaxy overdensity around four small-scale quasars originally identified in Hennawi et al. (2006). Therefore, the total number of quasar pairs including pairs from literature is 37, nine of which are $R_\perp < 1$ pMpc pairs. The redshifts of the additional pairs are shown in cyan in Figure A.4, and their properties are listed in Table A.5. The projected separation of the four pairs is almost comparable to the BOSS pairs, but SDSSJ1152-0030 ($z \sim 0.55$) has the smallest projected separation $R_\perp = 0.13$ pMpc ($\Delta\theta = 29.3$ arcseconds) among our sample.

A.4.2 $z \sim 1$ single quasars

To compare with the $z \sim 1$ pairs, we also measure the overdensity around single quasars at $0.9 < z < 1.1$ in the W-XMMLSS region. To extract only isolated quasars, we require that there is no neighborhood quasar at $R_\perp < 4$ pMpc and $\Delta V < 3000$ km s^{-1}, in addition to the BOSS redshift flag. We set this boundary larger than the maximum pair separation to remove companion quasars associated with quasar pairs. We also check to see whether their fields are suitable for overdensity measurements using the same criteria applied to the quasar pair fields. As a result, 127 isolated quasars at $z \sim 1$ are extracted, the sample size of which is large enough to statistically compare with the pair environments.

A.4.3 $z \sim 1$ galaxy selection

We measure the galaxy overdensity of the 37 pair and 127 single quasar fields at $z \sim 1$, using a photometric redshift catalog available in the DR S16A (`Mizuki`, Tanaka 2015) derived from the HSC-SSP survey. The accuracy of the photometric redshift ($z_{\rm phot}$) with respect to the spec-

troscopic redshift ($z_{\rm spec}$) is often characterized by two conventional quantities. The scatter is denoted as

$$\sigma_{\rm conv} \equiv 1.48 \times MAD\left(\frac{z_{\rm phot} - z_{\rm spec}}{1+z_{\rm spec}}\right) \tag{A.7}$$

, where MAD stands for median absolute deviation. The outlier rate is denoted as

$$f_{\rm outlier,conv} \equiv \frac{N(\frac{|z_{\rm phot}-z_{\rm spec}|}{1+z_{\rm spec}} > 0.15)}{N_{\rm total}} \tag{A.8}$$

, where the denominator stands for the total number of test samples and the numerator stands for the number of outliers. In the S16A dataset, the scatter and the outlier rate at $z \sim 1$ is $\sigma_{\rm conv} \sim 0.05$ and $f_{\rm outlier} \sim 0.1$ under a moderate seeing condition (0.7 arcsecond).

We extract surrounding galaxies within 2×2 deg^2 centered on the pairs and single quasars using the following criteria:

$$i < 24 \tag{A.9}$$

$$r < r_{\rm lim,5\sigma} \tag{A.10}$$

$$\frac{|\, z_{\rm med} - z_{\rm QSOP} \,|}{1+z_{\rm QSOP}} < 0.05 \tag{A.11}$$

, where we use the median redshift $z_{\rm med}$ defined as $\int_0^{z_{med}} P(z)dz = 0.5$ as a photometric redshift. $z_{\rm QSOP}$ is the average redshift of the two quasars in pair. The magnitude cut in i-band ($\sim i_{\rm lim,5\sigma}-2$) is to select galaxies with reliable classification and without significant contamination such as higher-redshift ($z > 3$) galaxies. It is noted that we select galaxies brighter than $\sim M^* + 2$ at $z \sim 1$ based on the M^* calculation in Boris et al. (2007). The scatter and outlier plots as functions of i-band magnitudes are given in Tanaka et al. (2017). We pick up galaxies at redshift within five percent of the pair redshift using the third criterion (Eq. A.11). This limit is selected to match the scatter of the photometric redshift (i.e., $\sigma_{\rm conv}$). Furthermore, quality flag cuts for the photometric redshift are applied[4] in addition to the same photometry flags in Section A.2.3. For the selected galaxies, we measure the local ovedensity significance in the pair fields following the same procedure for the high redshift pairs. We first calculate the galaxy density map at each grid

[4] Specifically, we use `photoz_prob_star`< 0.1 for removing Galactic stars, `reduced_chisq`< 10 for removing sources with unusual optical SEDs, and `photoz_conf_median`> 0.2 for removing sources with flat $P(z)$ distribution.

in 2×2 deg^2 around the pairs using the 1.8 arcminutes aperture, and then measure the local peak of the overdensity significance within two arcminutes from the pair center. At $z \sim 1$, its diameter corresponds to ~ 2 pMpc, comparable to the maximum pair separation. We use the peak significance to quantify the pair environments and compare it with that of other environments such as galaxies and isolated quasars.

A.4.4 Random fields around $z \sim 1$ galaxies

To compare with the pair and single quasar fields, we compute the peak significance distribution around randomly selected $z \sim 1$ galaxies. For this purpose, the random fields should be independent of the quasar presence. We make use of the 2×2 deg^2 fields around the 127 single quasars at $0.9 < z < 1.1$, and galaxies selected by the photometric redshift selection in Section A.4.3 (i.e., $i < 24$). We assume no significant redshift evolution of the surface galaxy density within $0.3 < z < 1.4$. In each of the 127 fields, we randomly pick ten galaxies removing the masked regions, the central 30×30 arcminutes^2 around quasars, and < 15 arcminutes at the edges. We then measure the significance peak within the two arcminutes radius to quantify the overdensity of the selected regions. We require that there is no overlap between each aperture centered at the randomly selected galaxies to ensure the independence of the selected regions. A certain amount of the 2×2 deg^2 fields overlaps, but this does not affect the randomness of the galaxy selection unless the selected galaxies are in vicinity of others. After examining the randomly selected positions of the galaxies to check for any overlaps of the two-arcminutes aperture with others, we finally derive the overdensity significance distribution around $z \sim 1$ galaxies from 849 random fields, which is sufficient to compare the significance distribution with the quasar fields.

A.5 Result II: $z \sim 1$ Quasar Pair Environments

A.5.1 Significance distribution

In this section, we show the result of the overdensity measurements in $z \sim 1$ quasar pair fields. Since we have an unprecedentedly large number of quasar pair samples, we are able to exam-

ine the rare pair environments with statistical approaches for the first time. Figure A.5 shows the normalized distribution of the peak significance around the pairs. Globally, the peak significance is distributed around a moderate density with the median significance of $< \sigma_{\mathrm{peak},2'} >= 1.97$. This result suggests that the quasar pairs at low redshift reside in moderate environments as a whole, in contrast to the high redshift pairs. This is consistent with the findings of the previous studies (e.g., Boris et al. 2007; Sandrinelli et al. 2014) in which they find no strong evidence that the local galaxy density is highly enhanced around $z \lesssim 1$ pairs. However, it is notable that the distribution has a long tail toward high significance up to 6.46σ. To be specific, there are seven pairs (19%) with $\sigma_{\mathrm{peak},2'} > 4$, including SDSSJ1152-0030, the pair with the smallest projected separation ($\sigma_{\mathrm{peak},2'} = 5.07$), and J020332-050944 & J020341-0500739, which has a companion ($\sigma_{\mathrm{peak},2'} = 5.18\sigma$). These $> 4\sigma$ pair fields were visually checked to confirm that the overdense regions are not fakes due to, for example, false detections of artificial noises around bright stars. Their local significance maps are shown in Figure A.6, where it is clear that the significance is highly enhanced between or on the pair members. The maps of the other pairs hosted in normal- or under-density regions are shown in Figure A.8 (Appendix A.5.2). We also show the peak significance in the $R_{\parallel} - R_{\perp}$ plane in Figure A.7, where $R_{\parallel}$ is the line-of-sight separation directly converted from the velocity difference ΔV. The significance is divided into three bins: $4 < \sigma_{\mathrm{peak},2'}$, $2 < \sigma_{\mathrm{peak},2'} \leq 4$, and $\sigma_{\mathrm{peak},2'} \leq 2$ with filled symbols showing the BOSS pairs and open symbols showing the Hennawi et al. (2006) pairs. The number of pairs in each bin and the number of sub pMpc-scale pairs are summarized in Table A.6.

In Figure A.5, we also compare the significance distribution with those of single quasars and randomly selected galaxies. As the median significances are 1.47 and 1.75σ, respectively, the overall significant distributions are only different by $< 1\sigma$ level from the pairs. However, a major difference is at the high density outskirt, where the significance distributions of single quasars and galaxies decline smoothly with the fraction of $> 4\sigma$ significance regions 2.4% and 2.0%, respectively. Taking advantage of the large sample size, we perform two-sample tests of goodness-of-fit to compare the three distributions. In all tests, the null hypothesis is that two non-parametric distributions are from the same underlying distribution. The significance threshold is set at 0.05. Three combinations of the pairs ("P"), single quasars ("S"), and random fields ("R") distributions are tested as we summarize in Table A.7. First, the Kolmogorov-

Table A.5: Quasar pairs at $z < 1.5$ from Hennawi et al. (2006)

ID	redshift	i [mag]	$\Delta\theta$ [arcsec]	$R_\perp$ [pMpc]	ΔV [km s^{-1}]	$\sigma_{\mathrm{peak},2'}$
SDSSJ1152-0030A	0.550	18.80 ± 0.02	29.3	0.19	740	5.07
2QZJ1152-0030B	0.554	19.99 ± 0.03				
2QZJ1209+0029A	1.319	20.26 ± 0.04	165.8	1.39	340	0.94
2QZJ1209+0029B	1.322	20.76 ± 0.05				
2QZJ1411-0129A	0.990	19.85 ± 0.04	152.5	1.22	1820	1.14
2QZJ1411-0129B	0.978	19.75 ± 0.03				
2QZJ1444+0025A	1.460	20.34 ± 0.04	113.3	0.96	1950	0.43
2QZJ1444+0025B	1.444	20.35 ± 0.04				

Notes: ID, redshift, separation are derived from their measurements converted with the cosmology we adopt. The i-band magnitudes are the extinction-corrected PSF magnitudes derived from the SDSS DR12. In the last column, we report the peak significance within two arcminutes around the pair center.

Table A.6: Summary of $z \sim 1$ pair environments

	$N_{4\leq\sigma_{\mathrm{peak},2'}}$	$N_{2\leq\sigma_{\mathrm{peak},2'}<4}$	$N_{\sigma_{\mathrm{peak},2'}<2}$	N_{total}
$R_\perp < 1$	2	3	4	9
$R_\perp \geq 1$	5	8	15	28

Notes: The overdensity significance of the 37 $z \sim 1$ pair fields are divided by the projected separation of the pair ($R_\perp < 1$ and $R_\perp \geq 1$ [pMpc]).

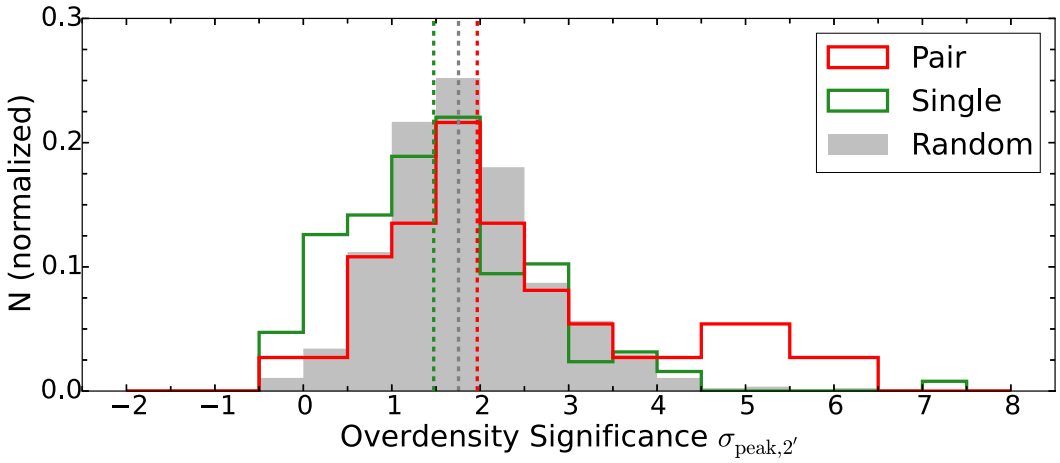

Figure A.5: Normalized distribution of the overdensity significance around $z < 1.5$ quasar pairs (red), $z \sim 1$ single quasars (green), and random galaxy fields (grey). The overdensity significance $\sigma_{\mathrm{peak},2'}$ is defined as the peak significance within a two-arcminutes radius from quasars or galaxies. The pair center is used for the case of quasar pairs. The negative significance means that all the areas inside the two-arcminutes radius have smaller galaxy densities than the average. The median value for each distribution (1.97, 1.47, and 1.75σ for pair, single, and random, respectively) is indicated with a vertical line.

Smirnoff (KS) test (Smirnov , 1939) shows that we cannot reject the possibility that any of the three samples come from the same distribution, implicating that there seem to be no significant levels of overdensity enhancement in pair and single quasar fields in a global view. On the other hand, the Anderson-Darling (AD) test (Stephens , 1974), which is more sensitive to the tail of the distribution, statistically supports that the pair environments are more likely to be overdense. Moreover, comparing the two quasar groups ("P-S" in Table A.7), we find that quasar pairs favor cluster environments. Intriguingly, it is also evident that the single quasar fields are likely underdense, compared with the galaxy fields. Since the two pairs at $z = 3.3$ and 3.6 have physical separations comparable to the $z \sim 1$ pairs, our result suggests that < 2 pMpc-scale quasar pairs are good tracers of massive clusters both at $z > 3$ and $z \sim 1$, yet the probability of finding clusters seems smaller at low redshift.

A.5.2 Low density environments around $z \sim 1$ quasar pairs

In Section A.5, we show that seven out of 37 $z \sim 1$ quasar pairs are embedded in $> 4\sigma$ overdenisty regions as shown in Figure A.6. Here, we show the other 29 pair fields showing lower ($\sigma_{\mathrm{peak},2'} < 4$)

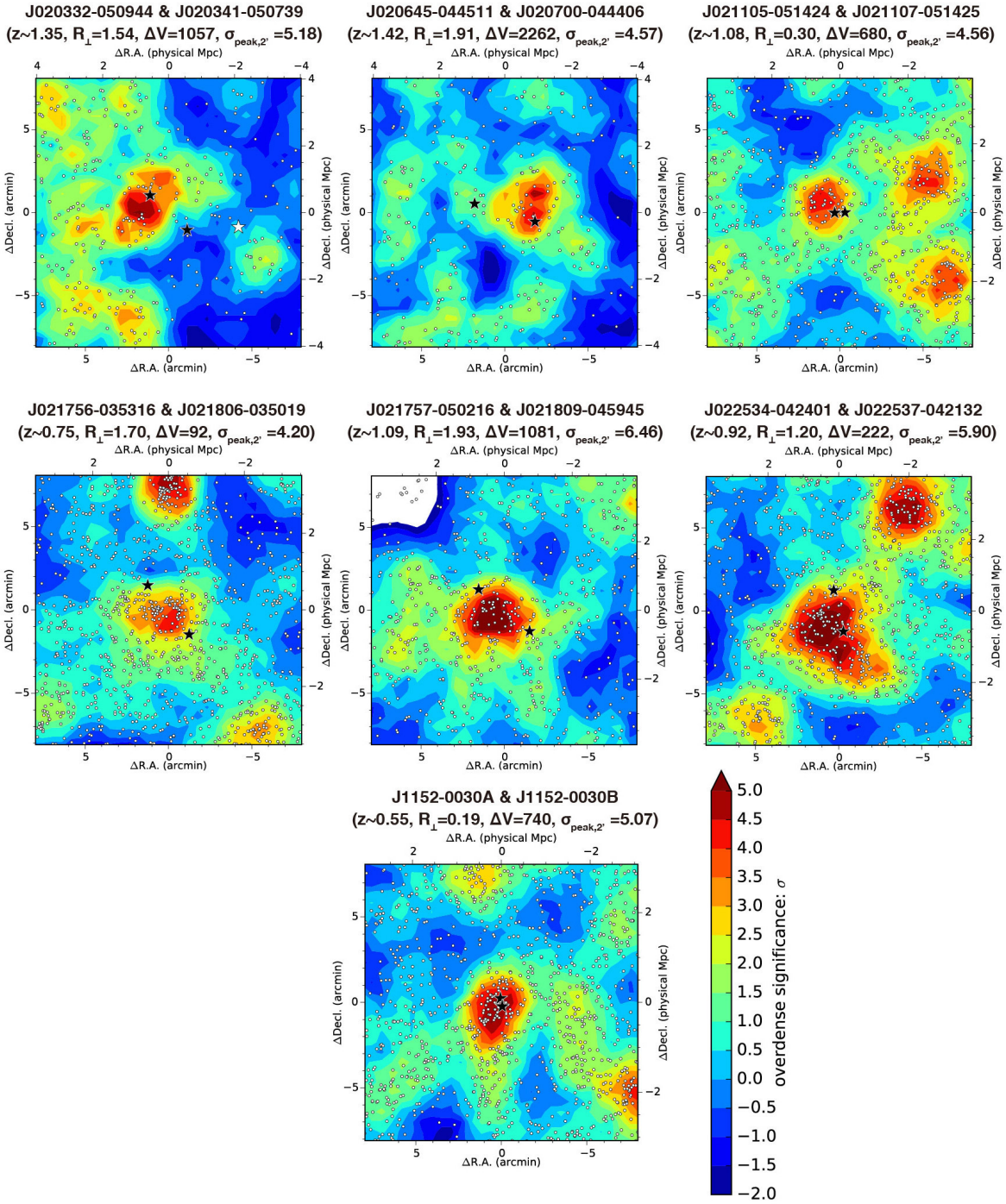

Figure A.6: Local significance maps for seven $z \sim 1$ pairs with $> 4\sigma$ overdensity within two arcminutes. The symbols and contours are the same as Figure A.1. The first six panels show the BOSS binary fields and the bottom panel shows the one from Hennawi et al. (2006). The white star in J020332-050944 & J020341-050739 field shows the companion quasar (SDSSJ020320.47-050933.8) at $z = 1.353$.

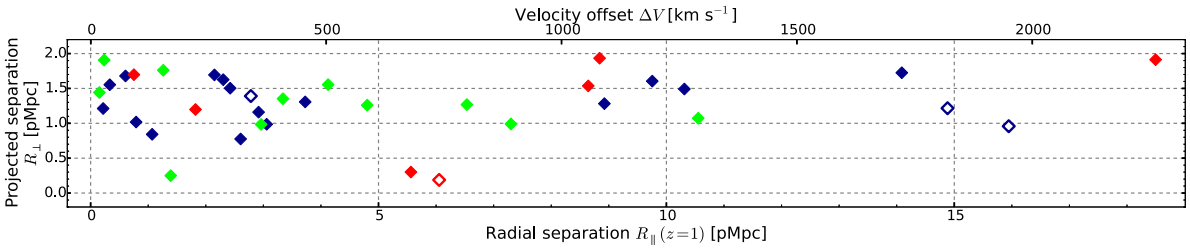

Figure A.7: The distribution showing the radial separation $R_\parallel$ [pMpc] and projected separation $R_\perp$ [pMpc] of the 37 pairs at $z \sim 1$. The radial separation $R_\parallel$ is converted from the velocity offset ΔV [km s^{-1}] assuming $z = 1$, which is also shown for reference. The color shows the peak significance within two arcminutes $\sigma_{\mathrm{peak},2'}$ in red ($4 \leq \sigma_{\mathrm{peak},2'}$), green ($2 \leq \sigma_{\mathrm{peak},2'} < 4$) and blue ($\sigma_{\mathrm{peak},2'} < 2$). The filled symbols show the BOSS quasar pairs. The open symbols show the pairs from Hennawi et al. (2006).

Table A.7: Two-sample KS and AD Test

	KS		AD	
	D	p	A^2	p
P-R	0.30	0.28	5.1	0.0033
S-R	0.20	0.77	9.8	0.0001
P-S	0.30	0.28	6.3	0.0014
$P_{z1.0}$ - $P_{z1.5}$	0.20	0.77	-1.0	1.0

Notes: "P" represents the quasar pairs, while "S" and "R" represent the single quasars at $0.9 < z < 1.1$ and the random sample as described in Section A.4.4. For example, the "P-S" stands for the comparison of the pair and single quasars. The "$P_{z1.0}$-$P_{z1.5}$" is the comparison of the pairs divided into two groups: $z < 1.0$ and $1.0 \leq z < 1.5$. The test statistics are shown in D and A^2 with corresponding p-values.

overdensity significance for reference in Figure A.8, in which their redshift, pair separation ($R_\perp$ and ΔV), and peak significance $\sigma_{\mathrm{peak},2'}$ are given. Note that J020320-050933 & J020332-050944, the companion pair of J020332-050944 & J020341-050739 at $z \sim 1.35$ is shown in the top-left panel of Figure A.6.

A.5.3 Significance dependence on redshift

Here, we examine the redshift dependence, albeit narrow range, of the peak significance of the pair environments. The pair sample is divided into i) $z < 1.0$ group and ii) $1.0 \leq z < 1.5$ group. There are 15 pair fields at $z < 1$ with median significance 2.08σ and 22 pair fields at $1 \leq z < 1.5$ with median significance 1.90σ. Figure A.9 compares the normalized significance distributions of the two pair groups. After applying the two-sample tests, we find that there is no significant redshift dependence of the peak significance (Table A.7). Note that this result supports our initial assumption that the pair environments do not significantly change at $0.3 < z < 1.5$.

A.6 Discussion

A.6.1 Enhancement of overdensity around $z > 3$ quasar pairs

In this study, we derive an implication that the rare occurrence of < 2 pMpc-scale quasar pairs is related to galaxy overdensity regions at $z > 3$ and also, with a statistical evidence at $z \sim 1$. At the high redshift, if the effective projection size of a $z \sim 4$ proto-cluster is defined as 1.8 arcminute (0.75 pMpc, Chiang et al. (2013)) radius, the total surface area of the 179 HSC proto-clusters is 0.51 deg^2, only 0.4% of the entire S16A field. Therefore, when one assumes a uniform surface density of quasar pairs, the chance that two randomly selected positions in 121 deg^2 are both in proto-cluster fields is only 2×10^{-5}, while we find two proto-clusters out of the two pairs.

At this stage, we again look at the work of Uchiyama et al. (2017). Using the same HSC g-dropout selection and parent quasar catalog, they suggest that the majority of 151 quasars at $z \sim 3.8$ likely reside in moderate-density environments. As also mentioned in Section A.3 in this paper, there are only six BOSS quasars located within three arcminutes (~ 1.25 pMpc) from the density peaks of the HSC proto-clusters, and intriguingly, three of them are the QSOP1 and

J020257-051225 & J020313-051057
(z~0.51, $R_\perp$=1.55, ΔV=504, $\sigma_{peak,2'}$ =2.08)

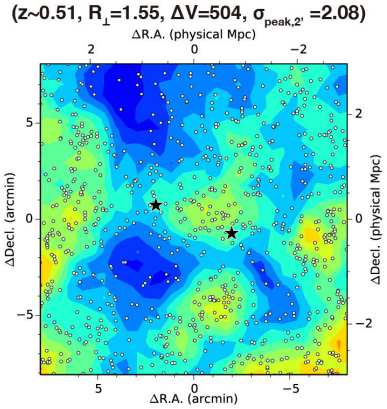

J020334-051721 & J020336-051545
(z~1.40, $R_\perp$=0.84, ΔV=130, $\sigma_{peak,2'}$ =1.62)

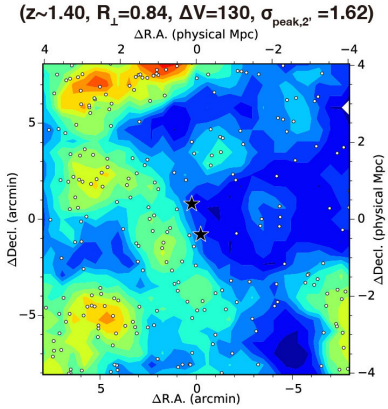

J020411-051032 & J020423-050619
(z~0.33, $R_\perp$=1.49, ΔV=1261, $\sigma_{peak,2'}$ =1.39)

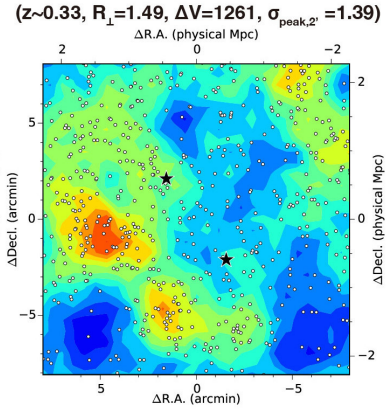

J020442-051041 & J020448-050923
(z~1.33, $R_\perp$=0.99, ΔV=374, $\sigma_{peak,2'}$ =0.92)

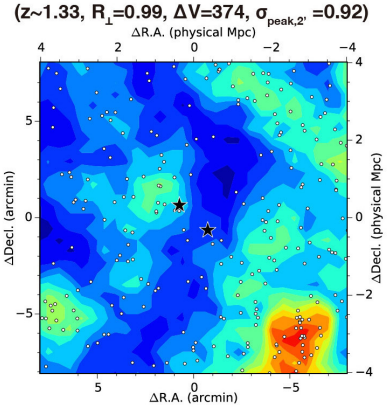

J020659-042343 & J020709-042501
(z~0.73, $R_\perp$=1.26, ΔV=587, $\sigma_{peak,2'}$ =2.94)

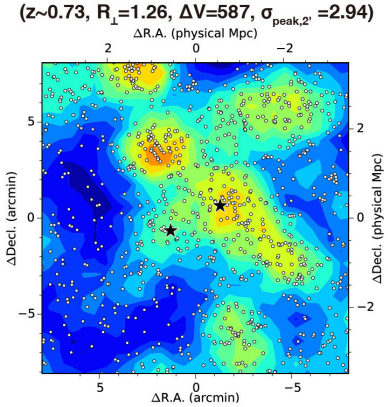

J021335-055002 & J021339-055241
(z~1.22, $R_\perp$=1.44, ΔV=18, $\sigma_{peak,2'}$ =2.41)

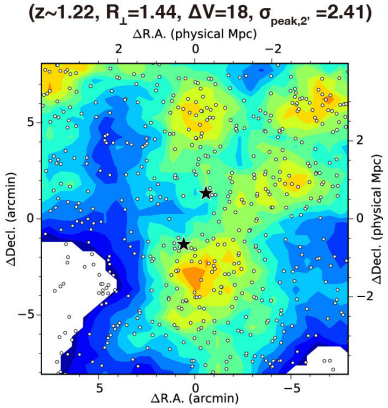

J021425-035631 & J021434-035555
(z~1.42, $R_\perp$=1.16, ΔV=356, $\sigma_{peak,2'}$ =1.12)

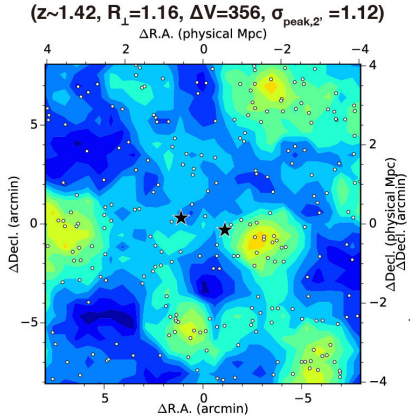

J021436-045150 & J021444-045012
(z~1.11, $R_\perp$=1.28, ΔV=1091, $\sigma_{peak,2'}$ =1.34)

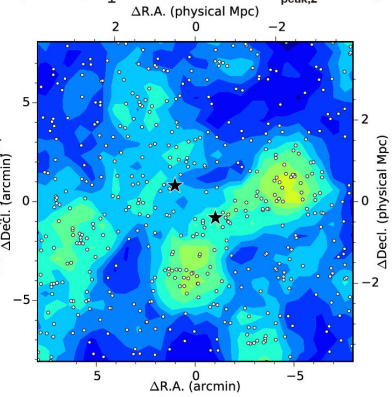

J021448-040626 & J021508-040513
(z~0.44, $R_\perp$=1.68, ΔV=74, $\sigma_{peak,2'}$ =1.83)

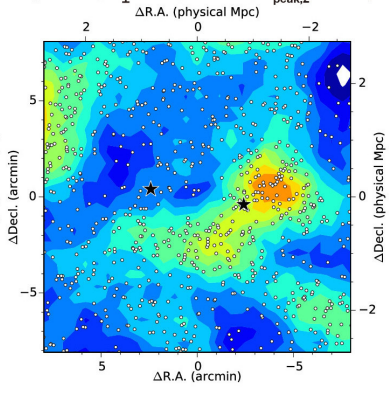

J021606-040513 & J021614-040626
(z~1.14, $R_\perp$=1.21, ΔV=26, $\sigma_{peak,2'}$ =-0.11)

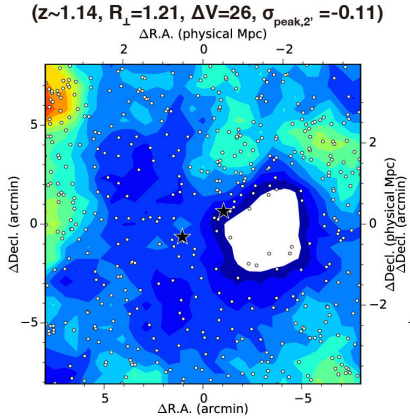

J021610-045229 & J021626-045308
(z~0.96, $R_\perp$=1.91, ΔV=28, $\sigma_{peak,2'}$ =3.43)

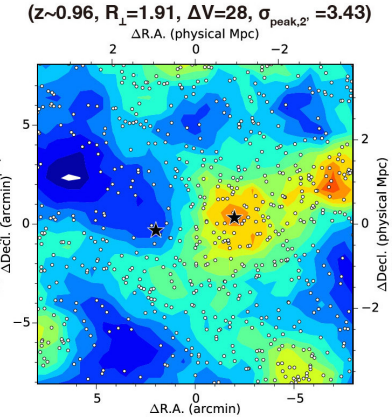

J021650-040142 & J021659-035853
(z~1.03, $R_\perp$=1.76, ΔV=154, $\sigma_{peak,2'}$ =2.85)

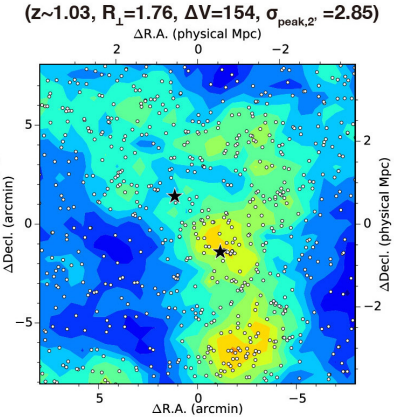

J021710-034101 & J021718-033857
(z~1.43, $R_\perp$=1.50, ΔV=296, $\sigma_{peak,2'}$ =1.37)

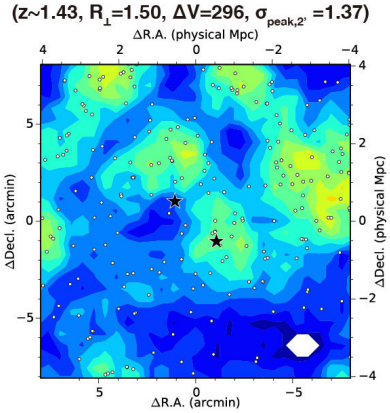

J021809-050200 & J021817-050258
(z~1.28, $R_\perp$=1.07, ΔV=1290, $\sigma_{peak,2'}$ =3.96)

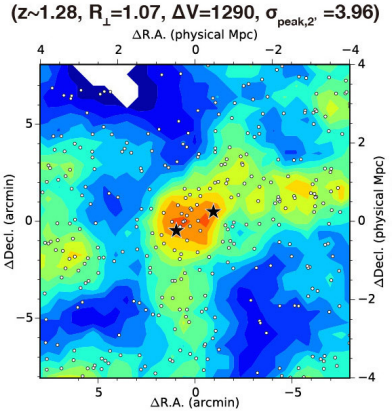

J022024-040017 & J022032-040332
(z~0.82, $R_\perp$=1.72, ΔV=1723, $\sigma_{peak,2'}$ =0.75)

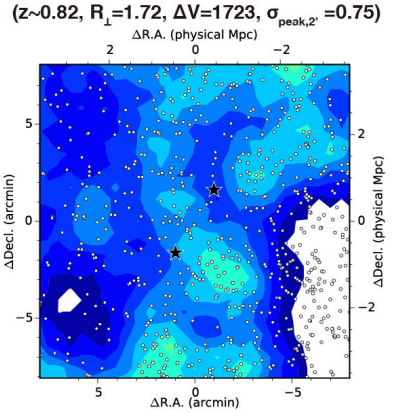

J022125-055638 & J022128-055857
(z~0.58, $R_\perp$=0.99, ΔV=893, $\sigma_{peak,2'}$ =2.98)

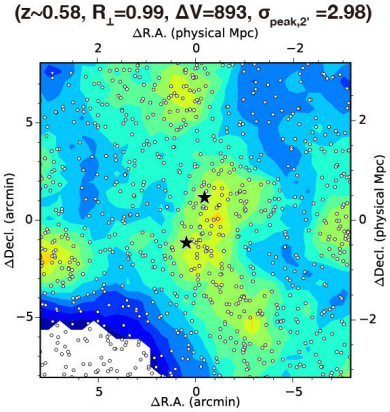

J022226-041313 & J022237-041140
(z~1.49, $R_\perp$=1.60, ΔV=1193, $\sigma_{peak,2'}$ =1.73)

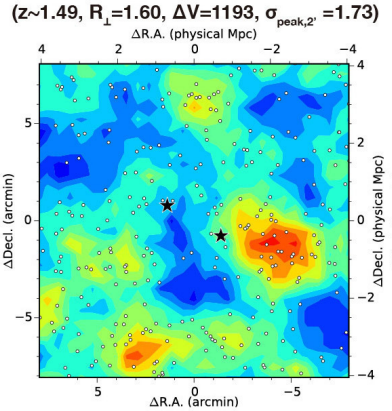

J022248-044824 & J022253-044513
(z~1.42, $R_\perp$=1.69, ΔV=263, $\sigma_{peak,2'}$ =1.97)

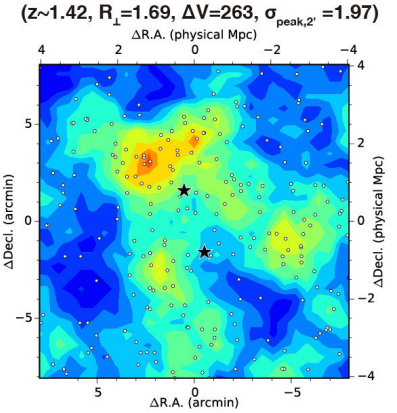

J022542-051452 & J022554-051354
(z~1.26, $R_\perp$=1.63, ΔV=281, $\sigma_{peak,2'}$ =1.82)

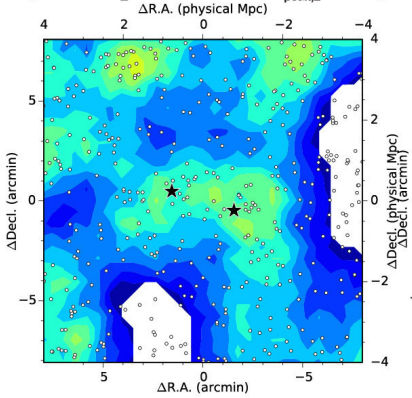

J022550-040247 & J022552-040516
(z~1.44, $R_\perp$=1.27, ΔV=799, $\sigma_{peak,2'}$ =2.25)

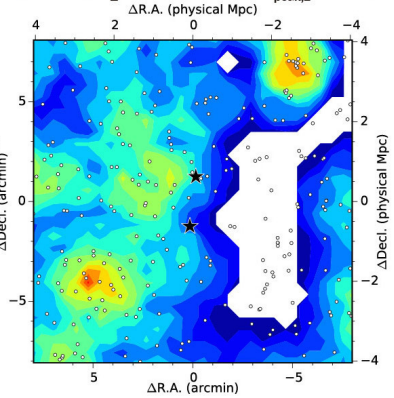

J022855-051130 & J022855-051450
(z~0.37, $R_\perp$=1.02, ΔV=96, $\sigma_{peak,2'}$ =0.78)

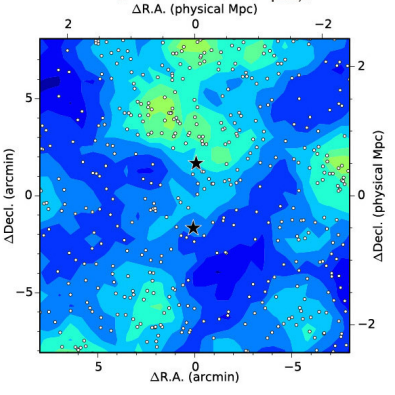

J022916-044600 & J022928-044444
(z~0.61, $R_\perp$=1.31, ΔV=455, $\sigma_{peak,2'}$ =1.60)

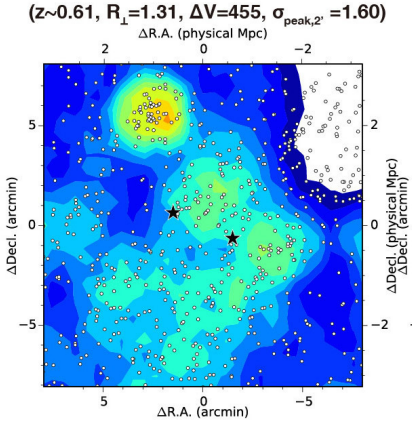

J023035-052603 & J023038-052336
(z~0.36, $R_\perp$=0.78, ΔV=318, $\sigma_{peak,2'}$ =1.84)

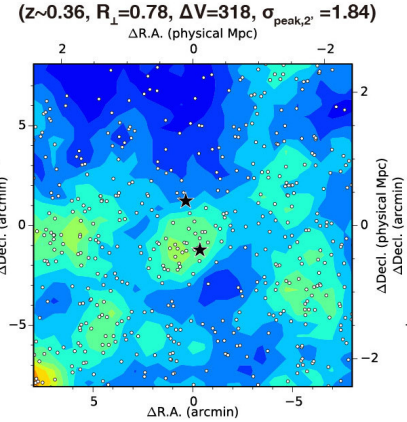

J023231-053655 & J023238-053903
(z~1.10, $R_\perp$=1.35, ΔV=408, $\sigma_{peak,2'}$ =3.18)

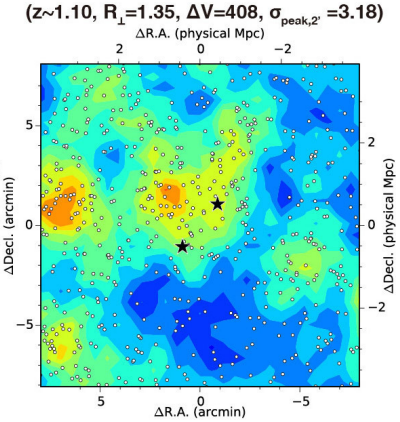

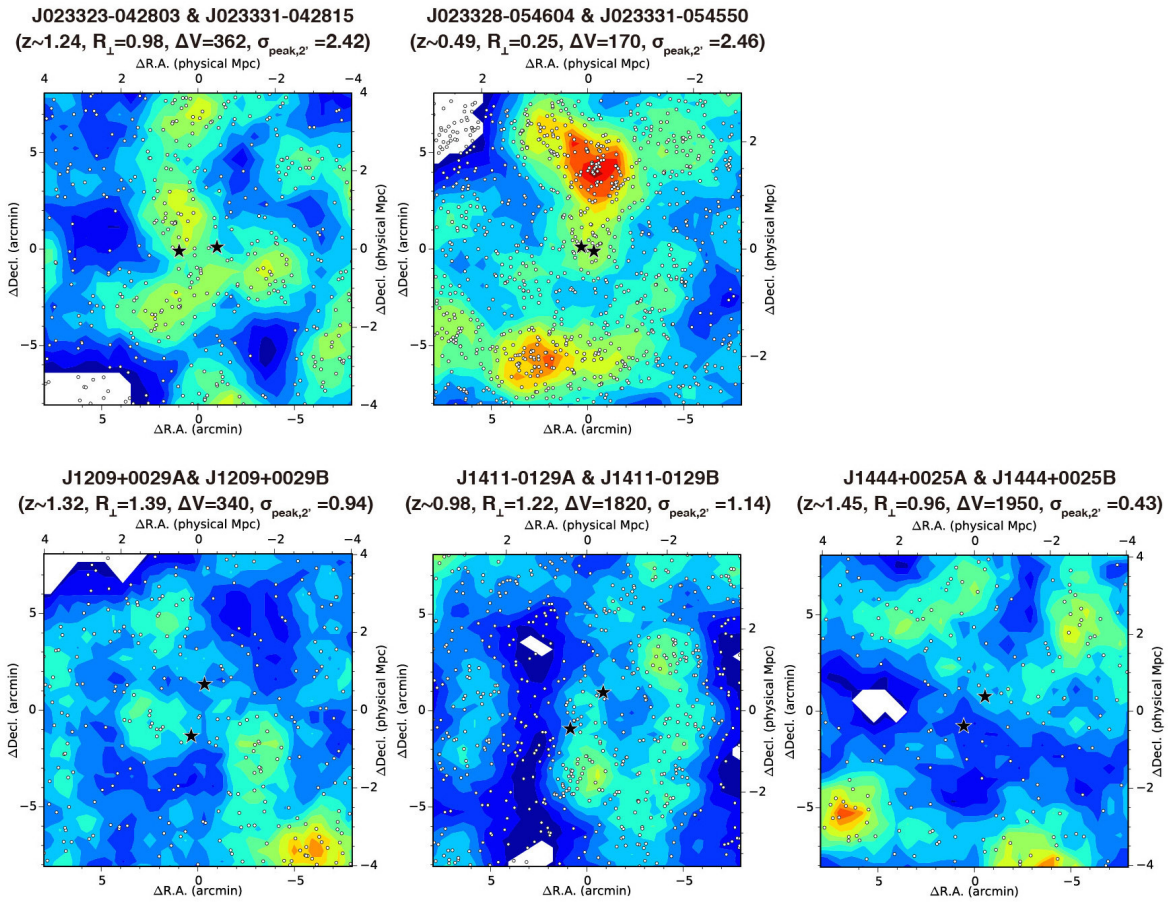

Figure A.8: Local significance maps of the 30 pair fields showing $\sigma_{\mathrm{peak},2'} < 4\sigma$. The symbols and contours are the same as Figure A.6. The first 27 panels show the BOSS pairs (see Table A.4), and the last three are the Hennawi et al. (2006) pairs (see Table A.5). Note that one field J020320-050933 & J020332-050944-050944 is shown in the panel in Figure A.6 (the first panel at the left-top).

QSOP2 pair members (Figure A.1). While several studies argue high-redshift quasar environments with small-field observations, for example using the *Hubble Space Telescope*, the area used for the overdensity measurements in our HSC-SSP studies is sufficient to identify proto-clusters and to see their whole structures thanks to the enormously wide coverage. Thus, it is assured that, unlike the average environments of isolated quasars at $z \sim 3.8$, the two quasar pair fields showing large excess ($> 5\sigma$) of overdensity significance are exceptionally rare and rich as quasar environments at this epoch. In terms of the triggering mechanism, our result suggests that, even though the vast majority of luminous quasars may be triggered via the secular process which is independent of the galaxy density, quasars turning on by the heavy interaction of massive galaxies do exist in massive haloes, and such quasar activity is perhaps so synchronous especially at high redshift that we observe more than one quasar in proto-clusters. This result supports our initial anticipation that pairs of luminous quasars are better tracers of proto-clusters than single quasars. Meanwhile, given that Fukugita et al. (2004) find no overdensity around a quasar pair at $z = 4.25$, while their imaging area is small (5.8 arcminutes^2), a bigger pair sample at $z > 3$ is needed to derive more conclusive evidence. Spectroscopic or narrow-band imaging follow-up observation of the two pair fields is required to address i) the identification of member galaxies, ii) the presence of faint quasars as the one found in the QSOP2 field, and iii) star-formation activity of the member galaxies.

It is notable that the two pair fields are not the richest among the HSC proto-clusters. Toshikawa et al. (2017) find up to 9σ overdensity regions, while the pair fields have 4.8 and 4.0σ in their measurements. The interpretation of this fact is not straightforward. The AGN feedback suppression of the quasar activity in the most massive haloes (Fanidakis et al., 2013; Orsi et al., 2015) could explain the absence of luminous quasars in the high density regions, though it cannot explain why the QSOP1 and QSOP2 pair members can emerge in proto-clusters. A certain number of quasars in proto-clusters could be missed in the incomplete selection of the BOSS catalog especially at $z > 3.5$, but it is unlikely that the members of the two quasar pairs pass the BOSS color selection but the majority of other quasars in other > 100 proto-clusters do not. As an alternative explanation, AGN in the most massive haloes just might not turn on in the more massive proto-clusters, if one takes into account the short AGN duty cycle of typically 10^7 years. In this context, another possibility would be that the quasar activity is triggered in the massive

haloes but they are not in the type-I quasar phase; thus they are not optically bright. Since we are just starting the proto-cluster search in the first ~ 100 deg^2, it would be of great interest to study the relation between the most overdense regions and luminous quasars with a larger sample size as the HSC-SSP survey coverage is enlarged. Furthermore, far-infrared or sub-mm studies of the HSC proto-clusters are necessary to probe obscured galaxies residing in proto-clusters.

We note that two sub pMpc-scale quasar pairs in Hennawi et al. (2010), namely SDSSJ1054+0215 at $z \sim 3.98$ and SDSSJ1118+0202 at $z \sim 3.94$ are at our redshift range and within the entire HSC-Wide survey area, while these fields have not been covered yet. Also, CFHTLSJ0221-0342, another small-scale pair at $z = 5$ reported in McGreer et al. (2016) is within the W-XMMLSS field covered with the HSC-Deep layer, but the current depth is almost the same as the Wide. We will investigate these small-scale pair environments at $z > 3$ after their fields are covered or the imaging gets deeper, to compare with larger separation pairs like the two in this paper as well as the other pairs which will be covered in the future HSC-SSP data release, and also with the $z \sim 1$ counterparts.

Finally, the environment around fainter $z > 3$ quasars is another important topic. While low-luminosity quasars are more easily triggered in normal environments as would also be the case for quasar pairs, such measurements will provide a clue to understand how the host haloes and surrounding galaxy overdensity affect the triggering mechanism of low-luminosity quasars. In the HSC-SSP, Akiyama et al. (2017) compile a > 1000 sample of $z \sim 4$ quasars down to $i = 24$ to derive the accurate shape of the quasar luminosity function at the faint end. He et al. (2017) discuss the clustering of their quasars to show that their host halo masses are moderate, with the order of $M_{\rm halo} \sim 10^{12} M_\odot$. To asses their measurements from an environment point of view, it is highly necessary to investigate the galaxy overdensity of their low-luminosity quasars.

A.6.2 Redshift dependence of quasar pair environments

Different environments between single quasars and pairs are also found at $z \sim 1$, as we show in Section A.5 that a significant fraction of quasar pair fields is at high density regions, which is statistically different from those of single quasars and randomly selected galaxies. However, a big difference from the $z > 3$ pair environments is that the significance distribution is globally the same among the three environments, meaning that quasars are generally common in any

environments at $z \sim 1$. Since the brightness of most $z \sim 1$ quasars is in the range of $19 < i < 21$ and this is the same for the pairs in $> 4\sigma$ regions, the brightness dependence of the pair environments does not have a major effect on the result.

The trend that not all $z \sim 1$ quasar pairs reside in massive environments as well as single quasars is consistent with previous studies. For example, Farina et al. (2011) show that, although the pair selection is severer than this study (i.e., $R_\perp < 500$ kpc and $\Delta V < 500$ km s^{-1}), in only one out of six pair fields at $z < 0.8$ shows significant overdensity using galaxies as bright as the ones in this study. Boris et al. (2007) adopt a loose pair selection at $z \sim 1$ ($\Delta\theta < 300$ arcseconds) comparable to this study. They conduct a deep optical imaging observation with Gemini/GMOS down to 1.5σ limit $i' = 26.4$ in four pair fields, showing that three pairs are associated with cluster environments but the other one is in an isolated field. Sandrinelli et al. (2014) stack the radial profile of galaxies in 14 pair fields at $z < 0.85$ ($R_\perp < 600$ kpc) and suggest that there is no clear enhancement of overdensity compared with single quasars. We note that the definition of overdensity and its significance are different among this and previous studies; therefore the probability of finding overdense regions around quasar pairs cannot be compared with this study. These results can be discussed under the downsizing evolution of the quasar activity. At high redshifts, quasar activity is most efficient in the most massive SMBHs residing in dense environments, for which plenty of cold gas is available for the mass growth to make gigantic SMBHs ($M_{\rm BH} > 10^9 M_\odot$) such as those found at $z > 6$ (e.g., Mortlock et al. (2011); Wu et al. (2015)). At lower redshifts, the galaxy interaction gets common in normal environments following the fast growth of SMBHs in proto-clusters. The luminosity where the quasar activity is most active shifts to a less luminous range as quasars are powered by already-matured black holes or less-massive black holes in their late growth. The observational evidence of such anti-hierarchical evolution is given by, for instance, Ueda et al. (2014) in their X-ray AGN luminosity function over $0 < z < 5$. In this respect, our result confirms the down-sizing trend of the SMBH growth by showing from an environmental point of view that the majority of low-redshift quasars, even for quasar pairs, turn on in moderate environments, in contrast to the $z > 3$ quasar pairs.

Furthermore, our measurement of > 30 $z \sim 1$ pair environments shows statistical evidence that, not all but $\sim 20\%$ of the quasar pairs does reside in cluster fields and this is distinguishable from the isolated quasar eivironments and random fields. This feature is found thanks to our

large sample size, while previous studies are limited to ∼ 10 pair fields. The high density tail in the significance distribution of the pairs suggests that the quasar activity is still ongoing in massive haloes and actually so active at $z \sim 1$ that more than one quasar are triggered at the same time. There should be isolated quasars in other massive environments, but they would be not visible since they are hidden by larger number of quasars in moderate environments. The implication of this trend is that there are still remnants and further accretion of cold-gas in cluster environments even after the major epoch of star-forming and SMBH feeding, and the frequent galaxy interaction can ignite more than one quasar simultaneously.

There are nine quasar pairs with less than 1 pMpc projected separation including two from Hennawi et al. (2006). From the nine sub pMpc-scale pairs, we find that two pairs, J021105-051424 & J021107-051425 at $z \sim 1.08$ ($R_\perp = 0.30$ pMpc, $\Delta V = 680$ km s^{-1}) and J1152-0030A & B at $z \sim 0.55$ ($R_\perp = 0.19$ pMpc, $\Delta V = 740$ km s^{-1}) are embedded in high density environments ($\sigma_{\mathrm{peak},2'} = 4.56\sigma$ and 5.07σ, respectively). On the other hand, the significance of the other seven pairs is moderate or small ($\sigma_{\mathrm{peak},2'} = 0.4 - 3.0$) like the larger-separation pairs. Therefore, while several studies on such small-scale clustering of quasars suggest that the clustering signal of projected correlation function is enhanced from the extrapolation from Mpc scale due to intense interaction of galaxies in massive haloes (Eftekharzadeh et al., 2017; Hennawi et al., 2006), our result implies that such small-scale quasar pairs are hosted not only in cluster fields but also in general fields at $z \sim 1$.

A.7 Summary

In this paper, we investigate the galaxy overdensity of quasar pair environments at high ($z > 3$) and low ($z \sim 1$) redshift, using the optical imaging catalog of the HSC-SSP survey (DR S16A) covering effectively 121 deg^2 with the i-band 5σ-depth of ∼ 26.4. The quasar pairs are primarily extracted from the SDSS DR12Q catalog with additional samples from the literature at $z \sim 1$. We use the photometric catalog of the HSC-SSP to select surrounding galaxies based on our g-dropout selection at $z > 3$ and photometric redshift selection at $z \sim 1$. The galaxy overdensity measurement around quasar pairs is based on the local significance of galaxies within a 1.8 arcminutes aperture at each square grid over a 2×2 deg^2 field separated by 0.6 arcminute. Our

main results are summarized as follows:

1. We find that two quasar pairs at $z = 3.3$ and 3.6 are associated with $\sigma_{\rm peak} > 5\sigma$ overdense regions. Their projection separations are $R_\perp = 1.75$ and 1.04 pMpc, and their velocity offsets are $\Delta V = 692$ and 1448 km s^{-1}, respectively. The number counts within five arcminutes around the two pairs are more than twice as high as field environments in all magnitude bins down to $i = 26$. Specifically, QSOP1 field has two brightest dropouts ($21.2 \leq i \leq 21.4$), which is six times higher density than the general fields. Since no apparent trend has been found to indicate that quasars at $z \sim 3.8$ are related to massive environments, pairs of luminous quasars are likely more efficient tracers of proto-clusters than isolated quasars, although a bigger pair sample is needed to discuss the probability of tracing the high density regions and its redshift dependence. Our result implies that the two quasar pairs are likely triggered via galaxy major merger, while the vast majority of isolated quasars are triggered via other processes such as bar and disk instabilities.

2. The overdensity significance of the $z > 3$ pair environments is not the highest among 179 HSC proto-clusters, which may imply that luminous quasars cannot emerge in the most massive haloes. However, this is not clear since we may miss quasars in the largest proto-clusters due to the incomplete selection of $z > 3.5$ quasars, and quasars may actually exist in the richest environments but they are not optically bright due to obscuration or their turn-off phase in the duty cycle.

3. We extend our study down to $z \sim 1$ using the HSC-SSP photometric redshifts. We select 33 pairs from the BOSS DR12Q and also four previously known small-scale pairs from Hennawi et al. (2006). While the distribution of peak significance within two arcminutes from the pair center is globally not different from those of isolated quasars and randomly selected galaxies at the same redshift range, a significant difference is found at the high density tail thanks to our large sample size. We find that 19% of the $z \sim 1$ pairs are within massive ($> 4\sigma$) environments and statistically confirm that this is unique in pair environments. Our result suggests that more than one quasar can ignite simultaneously in massive haloes even after the major epoch of the AGN activity, and quasar pairs are still good tracers of rich environments at $z \sim 1$, while the chance is lower than at $z > 3$. We detect no

redshift dependence of the significance between $z < 1$ pairs and $1 \leq z < 1.5$ pairs.

4. Among nine small-scale pairs with $R_\perp < 1$ pMpc, two of them reside in $> 4\sigma$ fields including the pair with the smallest projected separation, SDSSJ1152-0030A & B ($z \sim 0.55$, $R_\perp = 0.19$ pMpc). The other fields are moderate- or under-density regions, suggesting that sub pMpc-scale pairs could be embedded in general fields at low-redshift like isolated quasars.

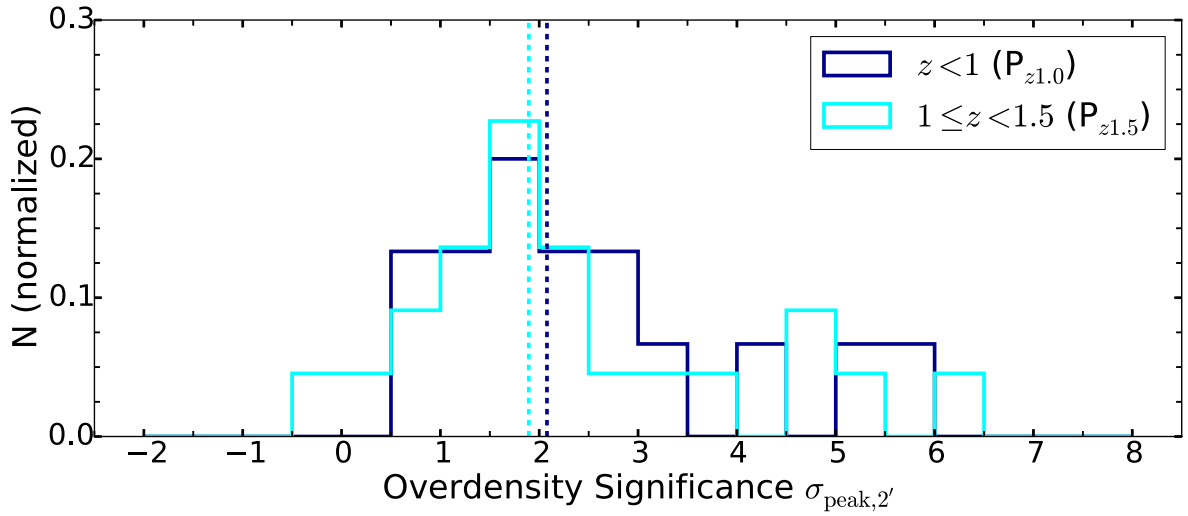

Figure A.9: Normalized significance distribution of the $z \sim 1$ pairs divided into $z < 1.0$ pairs ("$\mathrm{P}_{z1.0}$", blue) and $1.0 \leq z < 1.5$ pairs ("$\mathrm{P}_{z1.5}$", cyan). There are 15 pairs in $\mathrm{P}_{z1.0}$ group and 22 pairs in $\mathrm{P}_{z1.5}$ group. The grey histogram shows the random sample which is the same as in Figure A.5.

Bibliography

Aihara, H., Armstrong, R., Bickerton, S., et al. 2017, ArXiv e-prints, arXiv:1702.08449

Aihara, H., Arimoto, N., Armstrong, R., et al. 2017, ArXiv e-prints, arXiv:1704.05858

Akiyama, M., He, W., Ikeda, H. et al. 2017, ArXiv e-prints, arXiv:1704.05996

Alexander, D. M. and Hickox, R. C. 2012, New A Rev., 56, 93

Alexandroff, R., Strauss, M. A., Greene, J. E. et al. 2013, MNRAS, 435, 3306

Allard, F., Homeier, D. and Freytag, B. 2013, Mem. Soc. Astron. Italiana, 84, 1053

Bañados, E., Venemans, B. P., Morganson, E. et al. 2014, AJ, 148, 14

Bañados, E., Venemans, B. P., Decarli, R. et al. 2016, ApJS, 227, 11

Bañados, E., Venemans, B. P., Mazzucchelli, C. et al. 2017, ArXiv e-prints, arXiv:1712.01860

Becker, R. H., White, R. L., and Helfand, D. J. 1995, ApJ, 450, 559

Becker, G. D., Bolton, J. S., Madau, P. et al. 2015, MNRAS, 447, 3402

Bolton, J. S., & Haehnelt, M. G. 2007, MNRAS, 382, 325

Boris, N. V., Sodré, Jr., L., Cypriano, E. S. et al. 2007, ApJ, 666, 747

Bosch, J., Armstrong, R., Bickerton, S. et al. 2017, ArXiv e-prints, arXiv:1705.06766

Bouwens, R. J., Illingworth, G. D., Franx, M et al. 2007, ApJ, 670, 928

Bouwens, R., Illingworth, G., D., Oesch, P. A. et al. 2015, ApJ, 803, 34

Bouwens, R. J., Oesch, P. A., Illingworth, G. D. et al. 2017, ApJ, 843, 129

Cai, Z. Fan, X., Bian, F. et al. 2017, ApJ, 839, 131

Calzetti, D., Armus, L., Bohlin, R. C. et al. 2000, ApJ, 533, 682

Carnall, A. C., Shanks, T., Chehade, B. et al. 2015, MNRAS, 451, L16

Chardin, J., Puchwein, E., & Haehnelt, M. G. 2017, MNRAS, 465, 3429

Chiang, Y.-K., Overzier, R. and Gebhardt, K. 2013, ApJ, 779, 127

Coatman, L., Hewett, P. C., Banerji, M. et al. 2017, MNRAS, 465, 2120

Constraintin, A. & Shields, J. C. 2003, PASP, 115, 592

Dawson, K. S., Schlegel, D. J., Ahn, C. P. et al. 2013, AJ, 145, 10

De Rosa, G., Decarli, R., Walter, F. et al. 2011, ApJ, 739, 56

De Rosa, G., Venemans, B. P., Decarli, R. et al. 2014, ApJ, 790, 145

Dey, A., Soifer, B. T., Desai, V. et al. 2008, ApJ, 677, 943

Djorgovski, S., Perley, R., Meylan, G. et al. 1987, ApJ, 321, L17

Diamond-Stanic, A. M., Fan, X., Brandt, W. N. et al. 2009, ApJ, 699, 782

Di Matteo, T., Colberg, J., Springel, V. et al. 2008, ApJ, 676, 33

Djorgovski, S., 1991, ASP Conf. Ser., 21, 349

Djorgovski, S. G., Stern, D., Mahabal, A. A. et al. 2003, ApJ, 596, 67

Eftekharzadeh, S., Myers, A. D., White, M. et al. 2015, MNRAS, 453, 2779

Eftekharzadeh, S., Myers, A. D., Hennawi, J. F. et al., MNRAS, 468, 77

Fan, X., White, R. L., Davis, M. et al. 2000, AJ, 120, 1167

Fan, X., Strauss, M. A., Richards, G. T. et al. 2001, AJ, 121, 31

Fan, X., Strauss, M. A., Schneider, D. P. 2001, AJ, 121, 54

Fan, X., Narayanan, V. K., Lupton, R. H. et al. 2001, AJ, 122, 2833

Fan, X., Strauss, M. A., Schneider, D. P. et al. 2003, AJ, 125, 1649

Fan, X., Strauss, M. A., Richards, G. T. et al. 2004, AJ, 128, 515

Fan, X., Strauss, M. A., Richards, G. T. et al. 2006, AJ, 131, 1203

Fan, X., Strauss, M. A., Becker, R. H. et al. 2006, AJ, 132, 117

Fan, X., Carilli, C. L. and Keating, B. 2006, ARAA, 44, 415

Fanidakis, N., Macciò, A. V., Baugh, C. M. et al. 2013, MNRAS, 436, 315

Farina, E. P., Falomo, R. and Treves, A. 2011, MNRAS, 415, 3163

Farina, E. P., Montuori, C., Decarli, R. et al. 2013, MNRAS, 431, 1019

Fazio, G. G., Hora, J. L., Allen, L. E. et al. 2004, ApJs, 154, 10

Finkelstein, S. L., Ryan, Jr., R. E., Papovich, C. et al. 2015, ApJ, 810, 71

Fukugita, M., Nakamura, O., Schneider, D. P et al. 2004, ApJ, 603, L65

Giallongo, E., Grazian, A., Fiore, F. et al. 2015, A&A, 578, A83

Glikman, E., Helfand, D. J., White, R. L. et al. 2007, ApJ, 667, 673

Glikman, E., Helfand, D. J., White, R. L. et al. 2007, ApJ, 667, 673

Green, P. J., Myers, A. D., Barkhouse, W. A et al. 2011, ApJ, 743, 81

Gunn, J. E. and Peterson, B. A. 1965, ApJ, 142, 1633

Hatch, N. A., Wylezalek, D., Kurk, J. D. et al. 2014, MNRAS, 445, 280

He, W., Akiyama, M., Enoki, M. et al. 2017, ArXiv e-prints, arXiv:1704.08461

Hennawi, J. F., Strauss, M. A., Oguri, M. et al. 2006, AJ, 131, 1

Hennawi, J. F., Myers, A. D., Shen, Y. et al. 2010, ApJ, 719, 1672

Hennawi, J. F., Prochaska, J. X., Cantalupo, S. et al. 2015, Science, 348, 779

Hirano, S., Hosokawa, T., Yoshida, N. et al. 2017, Science, 357, 1375

Hopkins, P. F. and Hernquist, L. and Cox, T. J. et al. 2008, ApJ, 175, 356

Inada, N., Oguri, M., Shin, M.-S. et al. 2012, ApJ, 143, 119

Inayoshi, K., Haiman, Z., and Ostriker, J. P. 2016, MNRAS, 45, 3738

Inayoshi, K. & Haiman, Z. 2016, ApJ, 828, 110

Ishigaki, M., Kawamata, R., Ouchi, M. et al. 2017, ArXiv e-prints, arXiv:1702.04867

Izumi, T., Onoue, M., Shirakata, H. et al. 2018, ArXiv e-prints, arXiv:1802.05742

Jiang, L., Fan, F., Vestergaard, M. et al. 2007, AJ, 134, 1150

Jiang, L., Fan, X., Annis, J. et al. 2008, AJ, 135, 1057

Jiang, L., Fan, X., Bian, F. et al. 2009, AJ, 138, 305

Jiang, L., Fan, X., Hines, D. C. et al. 2015, AJ, 149, 188

Jiang, L., McGreer, I. D., Fan, X. et al. 2016, ApJ, 833, 222

Kashikawa, N., Aoki, K., Asai, R. et al. 2002, PASJ, 54, 819

Kashikawa, N., Ishizaki, Y., Willott, C. J. et al. 2015, ApJ, 798, 28

Kaspi, S., Maoz, D., Netzer, H. et al. 2005, ApJ, 629, 61

Kawanomoto, S. et al. to be submitted to PASJ

Kayo, I., and Oguri, M. 2012, MNRAS, 424, 1363

Kikuta, S., Imanishi, M., Matsuoka, Y. et al. 2017, ApJ, 841, 128

Kim, S., Stiavelli, M., Trenti, M. et al. 2009, ApJ, 695, 809

Kim, D., Im, M., Glikman, E. et al. 2015, ApJ, 812, 66

Kim, Y., Im, M., Jeon, Y. et al. 2015, ApJ, 813, L35

Kormendy, J. and Ho, L. C. 2013, ARAA, 51, 511

Kurk, J. D., Walter, F., Fan, X. et al. 2007, ApJ, 669, 32

Latif, M. A., & Ferrara, A 2016, PASA, 33, e051

Livermore, R. C., Finkelstein, S. L., & Lotz, J. M. 2017, ApJ, 835, 113

Lusso, E., Worseck, G., Hennawi, J. F., et al. 2015, MNRAS, 449, 4204

Madau, P., Haardt, F., & Rees, M. J. 1999, ApJ, 514, 648

Madau, P., & Haardt, F. 2015, ApJl, 813, L8

Magorrian, J., Tremaine, S., Richstone, D. et al. 1998, AJ, 115, 2285

Malmquist, K. G 1922, Lund Medd. Ser. I, 100, 1

Martine-Navarro, I., Brodie, J. P., Romanowski, A. J. et al. 2018, Nature in press, arXiv e-prints arXiv:1801.00807

Matsuoka, Y., Onoue, M., Kashikawa, N. et al. 2016, ApJ, 828, 26

—. 2018, PASJ, 70S, 35

Mazzucchelli, C., Bañados, E., Decarli, R. et al. 2017, ApJ, 834, 83

Mazzucchelli, C., Baña dos, E., Venemans, B. P. et al. 2017, ApJ, 849, 91

McGreer, I. D., Eftekharzadeh, S., Myers, A. D. et al. 2016, AJ, 151, 61

Mechtley, M. and Jahnke, K. and Windhorst, R. A. et al. 2016, ApJ, 830, 156

Miyazaki, S., Komiyama, Y., Sekiguchi, M. et al. 2002, PASJ, 54, 833

Miyazaki, S., Komiyama, Y., Nakaya, H. et al. 2012, Proc. SPIE, 8446, 84460Z

More, A., Oguri, M., Kayo, I. et al. 2016, MNRAS, 456, 1595

Morganson, E., De Rosa, G., Decarli, R. et al. 2012, AJ, 143, 142

Mortlock, D. J., Patel, M., Warren, S. J. et al. 2009, A&A, 505, 97

Mortlock, D. J., Warren, S. J., Venemans, B. P. et al. 2011, Nature, 474, 616

Mortlock, D. J., Patel, M., Warren, S. J. et al. 2012, MNRAS, 419, 390

Myers, A. D. and Richards, G. T. and Brunner, R. J. et al. 2008, ApJ, 678, 635

Nagao, T., Marconi, A., and Maiolino, R. 2006, A&A, 447, 157

Omukai K. 2001, ApJ, 546, 635

Ono, Y., Ouchi, M., Harikane, Y. et al. 2017, ArXiv e-prints, arXiv:1704.06004

Onoue, M., Kashikawa, N., Willott, C. et al. 2017, ApJ, 847, L15

Orsi, Á. A., Fanidakis, N., Lacey, C. G. et al. 2015, MNRAS, 456, 3827

Osterbrock, D. E. & Pogge, R. W. 1985, ApJ, 297, 166

Pâris, I., Petitjean, P., Ross, N. P. et al. 2017, A&A, 597, A79

Parsa, S., Dunlop, J. S., & McLure, R. J. 2017, ArXiv e-prints, arXiv:1704.07750

Peterson, B. M., Ferrarese, L., Gilbert, K. M. 2004, ApJ, 613, 682

Reed S. L., McMahon R. G., Banerji M. et al. 2015, MNRAS, 454, 3952

Reed, S. L., McMahon, R. G., Martini, P. et al. 2017, MNRAS, 468, 4702

Ricci, F., Marchesi, S., Shankar, F. et al. 2017, MNRAS, 465, 1915

Richardson, J., Zheng, Z., Chatterjee, S. et al., 2012, ApJ, 755, 30

Ross, N. P., Hamann, F., Zakamska, N. L. et al., 2014, MNRAS, 453, 3932

Salpeter, E. E. 1964, ApJ, 140, 796

Sandrinelli, A., Falomo, R., Treves, A. et al. 2014, MNRAS, 444, 1835

Schneider, D. P. and Fan, X. and Strauss, M. A. et al. 2000, AJ, 120, 2183

Schneider, D. P. and Hall, P. B. and Richards, G. T. et al. 2007, AJ, 134, 102

Schlafly, E. F. & Finkbeiner, D. P. 2011, ApJ, 737, 103

Schmidt, M. 1963, Nature, 197, 1040

Schmidt, M. 2015, ARAA, 53, 1

Schulze, A., Bongiorno, A., Gavignaud, I. et al. 2015, MNRAS, 447, 2085

Selsing, J., Fynbo, J. P. U., Christensen, L. 2016, A&A, 585, A87

Shen, Y., Strauss, M. A., Oguri, M. et al. 2007, ApJ, 133, 2222

Shen, Y., Greene, J. E., Strauss, M. A. et al. 2008, ApJ, 680, 169

Shen, Y., Brandt, W. N., Richards, G. T. et al. 2016, ApJ, 831, 7

Shibuya, T., Ouchi, M., Harikane, Y. et al. 2017, ArXiv e-prints, arXiv:1705.00733

Shull, J. M., Harness, A., Trenti, M. 2012, ApJ, 747, 100

Sikora, M., Stawarz, Ł., and Lasota, J.-P. 2007, ApJ, 658, 815

Smirnov, N. V. 1939, *Bulletin Moscow University*, 2, 3-16.

Song, H., Park, C., Lietzen, H. et al. 2016, ApJ, 827, 104

Steidel, C. C., & Hamilton, D. 1992, AJ, 104, 941

Stephens, M., A. 1974, *JASA*, 69, 730-737

Tanaka, M. 2015, ApJ, 801, 20

Tanaka, M., Coupon, J., Hsieh, B.-C. et al. 2017, ArXiv e-prints, arXiv:1704.05988

Toba, Y., Nagao, T., Strauss, M. A. et al. 2015, PASJ, 67, 86

Toshikawa, J., et al. to be submitted to PASJ

Trakhtenbrot, B., Lira, P., Netzer, H. 2017, ApJ, 836, 8

Uchiyama, H., Kashikawa, N., Toshikawa, J. et al. 2017, ArXiv e-prints, arXiv:1704.06050

Ueda, Y. and Akiyama, M., Ohta, K. et al. 2003, ApJ, 598, 886

Ueda, Y. and Akiyama, M., Hasinger, G. et al. 2014, ApJ, 786, 104

van den Bosch, R. C. E., Gebhardt, K., Gultekin, K. et al. 2012, Nature, 491, 729

Vanden Berk, D. E., Richards, G. T., Bauer, A. et al. 2001, AJ, 122, 549

Venemans, B. P., Röttgering, H. J. A., Miley, G. K. et al. 2007, A&A, 461, 823

Venemans, B. P., Findlay, J. R., Sutherland, W. J. et al. 2013, ApJ, 779, 24

Venemans, B. P., Bañados, E., Decarli, R. et al. 2015, ApJL, 801, L11

Venemans, B. P., Walter, F., Zschaechner, L. et al. 2016, ApJ, 816, 37

Vestergaard, M. and Wilkes, B. J. 2001, ApJS, 134, 1

Vestergaard, M. and Peterson, B. M. 2006, ApJ, 641, 689

Vestergaard, M. and Osmer, P. S. 2009, ApJ, 609, 800

Vestergaard, M. and Osmer, P. S. 2011, ApJ, 699, 800

Villforth, C. and Hamilton, T. and Pawlik, M. M. et al. 2017, MNRAS, 466, 812

Vito, F., Gilli, R., Vignali, C. et al. 2016, MNRAS, 463, 348

Volonteri, M. 2010, A&AR, 18, 279

Wang, R., Wu, X.-B., Neri, R. et al. 2016, ApJ, 830, 53

Wang, F., Fan, X., Yang, J. et al. 2017, ApJ, 839, 27

Welsh, B. Y., Wheatley, J. M. and Neli, J. D. 2011, A&A, 527, A15

Willott, C., Delorme, P., Omont, A. et al. 2007, AJ, 134, 2435

Willott, C., Delorme, P., Reyle, C. et al. 2009, AJ, 137, 3541

Willott, C., Albert, L. and Arzoumanian, D. 2010, AJ, 140, 546

Willott, C. J., Delorme, P., Reylé, C. et al. 2010, AJ, 139, 906

Wu, X.-B., Wang, F., Fan, X. et al. 2015, Nature, 518, 512

Wylezalek, D., Galametz, A., Stern, D. . et al. 2013, ApJ, 769, 79

Yang, Q. and Wu, X.-B. and Fan, X. 2017, AJ, 154, 269

York, D. G., Adelman, J., Anderson, Jr., J. E et al. 2000, AJ, 2000, 120, 1579